3-2023

Influence of Dilute Silicon Carbide Nanoparticle Additions to the Microstructure and Mechanical Properties of Laser Powder Bed Fusion Molybdenum

Nathan E. Ellsworth

INFLUENCE OF DILUTE SILICON CARBIDE NANOPARTICLE ADDITIONS TO THE MICROSTRUCTURE AND MECHANICAL PROPERTIES OF LASER POWDER BED FUSION MOLYBDENUM

DISSERTATION

Nathan E. Ellsworth, Maj, USAF

AFIT-ENP-DS-23-M-084

DEPARTMENT OF THE AIR FORCE
AIR UNIVERSITY

AIR FORCE INSTITUTE OF TECHNOLOGY

Wright-Patterson Air Force Base, Ohio

AFIT-ENP-DS-23-M-084

INFLUENCE OF DILUTE SILICON CARBIDE NANOPARTICLE ADDITIONS TO THE MICROSTRUCTURE AND MECHANICAL PROPERTIES OF LASER POWDER BED FUSION MOLYBDENUM

DISSERTATION

Presented to the Faculty

Graduate School of Engineering and Management

Air Force Institute of Technology

Air University

Air Education and Training Command

in Partial Fulfillment of the Requirements for the

Degree of Doctor of Philosophy in Materials Science

Nathan E. Ellsworth, B.S., M.S.

Maj, USAF

23 March 2023

AFIT-ENP-DS-23-M-084

INFLUENCE OF DILUTE SILICON CARBIDE NANOPARTICLE ADDITIONS TO THE MICROSTRUCTURE AND MECHANICAL PROPERTIES OF LASER POWDER BED FUSION MOLYBDENUM

DISSERTATION

Nathan E. Ellsworth, B.S., M.S.
Maj, USAF

Committee Membership:

Dr. Larry W. Burggraf
Chairman

Maj Ryan A. Kemnitz, PhD
Member

Dr. Joshua R. Machacek
Member

Dr. Adib J. Samin
Member

AFIT-ENP-DS-23-M-084

Abstract

Consolidation of molybdenum through laser powder bed fusion and other additive manufacturing (AM) techniques is complicated by a high melting temperature, high thermal conductivity, and a high ductile-to-brittle transition temperature. Nano-sized silicon carbide particles (0.1 wt%) were homogeneously mixed with molybdenum powder. The printing characteristics, chemical composition, microstructure, and mechanical properties were compared to pure molybdenum at four different scan speeds. As a function of improved melting and consolidation, the addition of nano-sized silicon carbide improved the optically determined density, flexural strength, and reduced the oxygen content over the four scan speeds analyzed. The oxygen concentration in the Mo-0.1SiC specimens increased with scan speed. Two mechanisms of oxygen reduction were posited as responsible for the improvements: oxidation of free carbon and the creation of secondary-phase nanoparticles. Positron annihilation lifetime spectroscopy and Doppler-broadening of annihilation radiation were used to monitor the sub-micron microstructure and compared with the microstructure revealed through electron back scatter diffraction analysis. The grain size and misorientation results do not correlate with positron lifetimes indicating the positrons are sampling regions within the grains. Positron annihilation spectroscopy identified the presence of dislocations and micro-voids not revealed through electron microscopy techniques and correlated with the findings of secondary-phase nanoparticles in the Mo-0.1SiC specimens. This dissertation illustrates the promising influence of nanoparticle additions to refractory metals in laser powder bed fusion. Additionally, the comparison of results indicate the usefulness of positron techniques to characterize nano-structure in AM metals due to significant increase in atomic-level information.

Acknowledgements

From the beginning of this doctoral experience, it was obvious that I would require the assistance of a great many people in order to graduate.

I would like to first thank my advisor, Dr. Burggraf, who from the outset of registering me for a first quarter advanced Nuclear Physics course, applied what seemed to be an intentional blind eye towards my shortcomings and ensured that I would attempt to accomplish things that I did not expect to be possible.

I would also like to thank my committee members, Dr. Samin, Dr. Kemnitz, and Dr. Machacek for their tireless efforts required to ensure my understanding of what are probably not overly complex concepts. In particular, a large thanks goes to Dr. Machacek for dealing with the time difference in Australia to be available on his first cup of coffee in the morning.

Finally, the completion of my work would not have been possible with the outstanding support from Cayla Eckley and Brianna Sexton in the Additive Manufacturing Laboratory. Their surface preparation and mechanical testing expertise were absolutely essential.

Nathan E. Ellsworth

Table of Contents

Page

List of Figures

List of Tables

INFLUENCE OF DILUTE SILICON CARBIDE NANOPARTICLE ADDITIONS TO THE MICROSTRUCTURE AND MECHANICAL PROPERTIES OF LASER POWDER BED FUSION MOLYBDENUM

I. Introduction

There were two goals that guided the course of the materials research presented in this dissertation: investigate the influence of nanoparticle silicon carbide (SiC) additions to laser powder bed fusion (LPBF) molybdenum on microstructural, chemical, and mechanical properties and explore the ability of positron annihilation spectroscopy (PAS) techniques to identify differences in the nanostructure and microstructure produced by varying parameters in the LPBF process. These goals are addressed as problem statements with associated hypotheses in Chapter 1. Chapter 2 presents background on molybdenum, silicon carbide, and the laser additive manufacturing (AM) of refractory metals, specifically, work conducted on molybdenum and with added carbides. Chapter 3 covers the basics of positron theory, their interaction with condensed matter, and an introduction to positron measurement techniques. Previous positron measurements on molybdenum are referenced when discussing the results of the experimental work outlined in this dissertation. Chapter 4 presents the results from the traditional materials characterization techniques while Chapter 5 discusses the results of the positron measurements. Chapter 6 presents the conclusions and proposed future work.

1.1 Overview

Refractory metals have only just begun to be investigated for use in AM processes over the last ten years, starting with the development of tungsten collimators for magnetic resonance instruments in the medical field [1]. The near net-shape preparation of components through additive techniques is ideal for refractory metals due to their inherently high ductile-to-brittle transition temperature (DBTT) which impedes room temperature post-processing [2]. Unfortunately, while the potential for AM refractory metal preparation is enticing, processing improvements must be made before industrial adoption is ensured currently, parts do not meet the rigorous standards required for their use [3]. This research describes the potential of nanoparticle silicon carbide additions to improve AM molybdenum.

The microstructure of LPBF metals are different from those of traditionally wrought origin. Grain sizes are refined due to the rapid cooling of the melt pool and the thermal gradients involved promote epitaxial grain growth along the longitudinal (build, XZ) direction resulting in a columnar orientation that isn't reflected in the transverse (print, XY) direction. The mechanical properties thus exhibit strong anisotropic behavior that is undesirable in most applications for which refractory metals are used. As with metals that are more easily prepared through AM techniques, such as Inconel, it has been shown that post-processing heat treatments can correct the anisotropic grain structure in LPBF tungsten [4, 5]. It is well known that dilute additions of secondary particles have the ability to greatly influence the microscopic and macroscopic properties of refractory metals. In this research, the addition of silicon carbide to LPBF molybdenum has been explored as a means of favorably altering the grain morphology and improving consolidation. This research included chemical analysis, microstructural characterization, and mechanical testing of LPBF molybdenum and molybdenum with 0.1wt% of nano-sized silicon carbide (Mo-0.1SiC). Additionally,

PAS techniques were used to distinguish between LPBF microstructures and provide nondestructive testing (NDT) analysis of the quality of LPBF builds. Silicon carbide was identified as a nanoparticle additive to LPBF molybdenum that bolsters the print-ability and alters the microstructure to improve the mechanical properties. Positron annihilation lifetime spectroscopy (PALS) proved successful in identifying differences in the sub-grain, nano-structures of LPBF molybdenum and Mo-0.1SiC that were not readily observed by standard microscopy techniques. The associated results of Doppler-broadening of annihilation radiation (DBAR) measurements were inconclusive.

1.2 Motivation of Research

The production of high performance components through AM has grown rapidly over the last two decades into a technology that is known for producing highly complex three-dimensional objects through layer-by-layer sequential welding of powder feedstock [6]. There are numerous AM categories including material extrusion, vat photopolymerization, powder bed fusion, binder jetting, material jetting, and direct energy deposition procedures. Each of these categories include various methods that comprise the totality of current AM efforts [7].

Powder bed fusion techniques include LPBF, selective laser sintering, selective laser melting, electron beam melting, direct metal laser sintering, direct metal laser melting, and multi-jet fusion, with the differences between them being mostly related to manner in which the thermal energy is applied. These techniques are known for producing some of the strongest AM structures in polymers, metals, and metal alloys [8].

The importance of AM as an emerging industrial practice cannot be overstated. Rapid prototyping using AM can reduce weeks of scheduling by removing the need for

traditional setup, mold designs, and tooling. Traditional processes, such as casting and milling, cannot produce the intricate designs that are ubiquitous to AM techniques. Complex lattice structures result in a three-dimensional component that has a higher strength-to-weight ratio using less material than traditional manufacturing.

While originally limited to production of plastic components, many other materials including, but not limited to, ceramics [9], glass [10], wood [11], biological materials [12], and metals [13, 14, 15, 16, 17, 18] are becoming more common. Metal AM components are finding extensive uses in the military [19], aerospace [20], biomedical [21], and energy [22] industries, among others [23].

Characterized by incredible design flexibility and low overhead costs, LPBF enables the processing of complex components using high performance metals and alloys that are simply not possible with traditional subtractive manufacturing techniques. From aluminum, titanium, nickel, and chromium to tungsten-based superalloys, LPBF technology has begun to emerge as a potential option for the design and manufacturing of high performance materials and parts. AM techniques lend themselves to weldable metals and alloys, and as such, nickel-based alloys, like the Inconel series, have been used to produce rocket injectors, turbine blades, borescope bosses, and hydraulic valves with relative success using LPBF [24].

While nickel and titanium based super-alloys offer impressive high temperature strength, nothing compares to the performance of refractory metals. Tungsten, molybdenum, tantalum, niobium, and rhenium make up the class of refractory metals if defined by melting temperatures above 2000°C [25]. The use of refractory metals is, for the most part, widespread, if a bit specialized. The general properties of all refractory metals are high density, hardness, melting points, and high strength at elevated temperatures as well as low coefficients of thermal expansion and high thermal and electrical conductivity [3]. The usefulness of refractory materials at high temper-

atures are limited due to the products of their oxidation which generally provide no protection to further oxidation.

LPBF offers a unique avenue to exploit the desirable properties of refractory metals by reducing unnecessary weight through component design. AM can produce structural materials by adding the strength where it is needed and removing weight where it is not [26]. As the raw precursors for high performance materials are expensive, AM processes offer a cost effective approach to small-batch and specialized production. Traditional techniques are likely to be more cost effective for large-batch production currently [27], but metal LPBF offers a relatively cheap and accessible tool to conduct advanced material research.

Of the five refractory metals, tungsten and molybdenum are far cheaper per kilogram than tantalum, niobium, and rhenium. Tungsten offers the best performance at high temperature of any of the refractories, but it's high melting point requires more energy input to produce proper melting and fusion in AM builds. Molybdenum shares similar strength properties to tungsten at intermediate temperatures with a lower melting point and hardness which makes it a more accessible LPBF material.

Most molybdenum is prepared for use as an alloying agent in different types of steel, with the London Metal Exchange estimating roughly 75% of world production going to this purpose. Other uses of molybdenum are found in lubricants, catalysis reactions, and as an ingredient in high performance alloys and ceramics [28].

Molybdenum-based materials offer promise as high-performance, high-temperature, structural materials, however, the fabrication through additive techniques is challenging due to the high melting temperatures and brittleness. While there has been less research on AM of molybdenum when compared to tungsten, many of the issues are the same [29]. AM alloys containing significant amounts of tungsten suffer from defects and cracking due to their inherent brittleness and high melting temperatures.

Thermal stresses arise when the melt pool cools. These stresses can be accommodated when above the DBTT, but rapid cooling and oxygen embrittlement of the grain boundaries can increase this transition temperature [29]. Generally, the formation of pores and micro cracks are not predictable events and can occur at any time during the LPBF process. Detailed information on the issues concerning the AM of refractory metals is provided in Chapter 2.

The issues plaguing the LPBF of molybdenum are similar to those found in tungsten, such as delamination effects [30], porosity, low relative density, and cracking [31]. Attempts over the past few years to improve the print-ability of pure molybdenum have centered on the addition of small amounts of carbon. This addition had the effect reducing the impact of oxygen segregation to the grain boundaries, improving crack resistance during printing, and the overall strength of the material [32, 33, 34].

Li et al. [35] successfully suppressed the growth of crack formations in LPBF tungsten by introducing a small weight percentage of zirconium carbide (ZrC). Secondary-phase nanoparticles of zirconium oxide (ZrO_2) refined the microstructure and the available carbon captured oxygen impurities.

Chen et al. saw improved crack resistance and mechanical properties in LPBF tungsten with the addition of tantalum carbide (TaC) [36]. The effects of TaC were similar to what Li et al. documented with ZrC, however carbides were formed as secondary nanoparticles instead of oxides.

With the microstructure of AM materials playing such a critical role in their mechanical performance it is imperative that methods be available to qualify components and ensure the vast possibilities of AM-caused defects are not present. There are numerous quality control (QC) methods that have been established for LPBF. Material characterization techniques such as x-ray crystal diffraction (XRD), Raman spectroscopy, energy-dispersive x-ray spectroscopy (EDS), scanning electron microscopy

(SEM), and optical microscopy (OM), have been used to characterize the particle size distribution, shape, and aspect ratio of metal powders prior to printing. Density can be measured through gas pycnometry and chemical analysis can determine composition [37]. Melt pool temperature and shape can be monitored through integrating cameras attached directly to the scan head [38]. Transmitters and analyzers have been used within the build chambers to monitor for the presence of oxygen [39]. Acoustic-based testing methods, such as ultrasonic testing and acoustic emission spectroscopy, have been conducted to evaluate porosity, cracking, balling, and overheating. Generally these methods are more suited for qualitative assessments, but could potentially be calibrated for specific types of pores [40, 41]. Optical imaging and optical emission spectroscopy (OES) can be used to visually inspect the surface of the build to inspect for porosity or irregularities in the powder bed or powder layer after spreading and before exposure of the next laser pass. OES is commonly used in other manufacturing techniques as well [42, 43]. Tomographic techniques have been used to produce a three-dimensional representation of defect structure by compiling multiple two-dimensional images throughout the build process. Optical and x-ray tomography provide information on porosity, lack-of-fusion, and balling [44, 45, 46]. Thermal imaging has been adopted recently to measure the thermal gradients and thermal radiation signatures given off by the laser, melt-pool, and surrounding metal substrate [38]. Generally, thermal measurements are surface techniques; however, infrared imaging has been used to measure inter-layer cooling rates [47]. Pyrometry, a technique that uses non-contacting photodiodes to measure temperature, has been used to investigate the laser spot temperature and the gradients in the surrounding melt-pool and substrate [48]. Commercially, thermal and optical techniques are used and are offered through a large number of AM instrument providers. These in-situ capabilities focus on the the temperature and geometry of the melt pool, laser spot,

and the build platform [49]. While all of these techniques are still receiving considerable attention in the literature, they lack the sensitivity to nanoscale defects. PAS techniques offer the potential for in situ monitoring that is sensitive to nano-scale features.

PALS measurements are sensitive to the electronic structure of materials and can probe the interior of a three-dimensional structure for vacancy-type, open-volume defects at the sub-micron scale. Non-destructive in nature, PALS offers the capapbility to identify defect size, type, and distribution. Depending on the energy of positrons upon implantation, PAS can be a near-surface or bulk technique. The qualities of this type of material characterization technique can provide additional context to current approaches.

1.3 Problem Statements

There were two goals of this research. The first was to understand how the addition of a dilute amount of silicon carbide to pure molybdenum powder influences the microstructure and mechanical properties of LPBF molybdenum and the second was to determine the ability of PAS techniques to distinguish between the microstructures developed during the LPBF process. Silicon carbide was chosen to act as an oxygen scavenger during the build process. It was hypothesized that the nano-sized silicon carbide particles would refine the grain boundaries, limit crack growth, and increase strength. Additionally the nano-sized particles would increase the energy coupling of the laser and powder leading to better fusion and overall print-ability.

The major problems surrounding the printing of refractory metals are widely known in the AM community. High melting points, brittleness upon cooling, oxygen segregation at the grain boundaries, and extreme temperature gradients all negatively impact AM of refractory metals. Therefore, this research both looked into the ability

of an addition of a small amount of nano-sized silicon carbide to pure molybdenum powder to positively influence the microstructure and mechanical properties, and the changes in positron annihilation characteristics associated with those microstructures.

Problem Statement 1: Molybdenum parts consolidated through LPBF AM suffer from cracking and porosity due, in part, to oxygen segregation to the grain boundaries.

Like most body centered cubic (BCC) heavy metals, the DBTT of pure polycrystalline molybdenum is not a sharp transition, but instead a temperature range around room temperature that is dependent on strain rate [50, 51]. The addition of impurities, such as oxygen, to the grain boundaries can increase this DBTT from room temperature up to 400°C [52].

Hypothesis 1.A: The addition of silicon carbide will reduce the segregation of oxygen impurities during the LPBF process and improve consolidation.

Objective 1.A: Characterize elemental composition of the as-built molybdenum and Mo-0.1SiC specimens using inert gas fusion analysis. Compare to the initial feedstock powders. Observe fracture surfaces and grain morphology with electron microscopy.

Hypothesis 1.B: Improved consolidation will reduce cracking, porosity, and improve mechanical properties.

Objective 1.B: Conduct hardness and three-point bend strength measurements. Perform tests on specimens with and without nanoparticle silicon carbide additions at various scan speeds. Compare results to identify the influence of nanoparticle silicon carbide additions and scan speed.

Hypothesis 1.C: The addition of nanoparticles to molybdenum powder will increase the ability of the powder bed to absorb the energy from the laser and improve melting.

Objective 1.C: Conduct reflectance measurements on the pure and mixed powders. Measure the macroscopic porosity and observe the fracture surfaces using optical and electron microscopy, respectively, to compare the impact of silicon carbide additions on the laser-energy coupling and consolidation of molybdenum powder.

Hypothesis 1.D: Additions of carbides to AM tungsten have created the presence of secondary phase nanoparticles. Silicon carbide will produce secondary phase silicon-oxygen nanoparticle inclusions in the AM molybdenum matrix that can sequester oxygen from the grain boundaries.

Objective 1.D: Characterize the microstructure of Mo-0.1SiC using transmission electron microscopy (TEM). Determine the presence of secondary phase nanoparticles and use EDS to determine elemental content.

Problem Statement 2: Defects that promote crack propagation in molybdenum can be on the atomic scale and the resolution of traditional microscopy techniques make it difficult to resolve these types of bulk microstructural defects.

Hypothesis 2: The presence of silicon carbide in the molybdenum powder will produce microstructural differences that may not be readily apparent under standard microscopic techniques; however, PAS methods will have potential for NDT interrogation of nano-scale microstructural features in LPBF metals.

Objective 2: Determine the positron lifetimes associated with the pure molybdenum and Mo-0.1SiC specimens printed at various scan speeds. Correlate to known microstructural changes from other techniques.

Problem Statement 3: The anisotropic nature of crystal growth found within AM molybdenum and other metals creates undesired microstructures leading to mechanical performance that is unacceptable for most applications.

Hypothesis 3: PAS techniques will be sensitive to the significant microstructural differences found in the longitudinal and transverse directions of AM parts and can be used as a nondestructive measurement technique to distinguish between AM microstructures.

Objective 3: Identify the position lifetimes and Doppler broadening associated with pure molybdenum when approached in the transverse and longitudinal orientations.

1.4 Summary of Methodology

In order to assess the hypotheses proposed in the previous section, the microstructures of the molybdenum and Mo-0.1SiC system were examined with conventional materials characterization techniques and PAS. Molybdenum and Mo-0.1SiC powders were printed using LPBF in a nitrogen atmosphere at four different scan speeds: 100, 200, 400, 800 mm/s. The powders and built specimens were characterized for pure molybdenum and molybdenum with 0.1 wt% nano-sized silicon carbide added. The microstructures of the as-printed specimens were analyzed by optical microscopy (OM), scanning electron microscopy (SEM), and transmission electron microscopy (TEM). Chemical compositions of the feedstock powders and as-printed specimens was determined through inert gas fusion analysis per American Society for Testing and Materials (ASTM) Standard E 1019-18 [53]. The reflectance of the pure and mixed powders was measured via ASTM Standard E 903-20 [54]. Hardness and flexural strength measurements were conducted on the as-printed specimens. PALS and DBAR were used to assess differences in the microstructures of the as-printed samples and compare to traditional pure molybdenum. The data collected from the PAS measurements was correlated to the data collected from the other characterization techniques and used to evaluate the effectiveness of selected build parameters and the

use of PAS as a QC method.

1.4.1 Metallography

Metallography includes techniques that investigate the microstructure and chemical composition of metals and metal alloys [55]. OM, SEM, and TEM were used extensively to characterize the powders and the as-printed specimens. Through OM, changes to crack formation and porosity due to varied scan parameters were quickly evaluated. After the grinding, polishing, and etching of a sample, the grain structure, defects, and porosity became observable. SEM was used to investigate as-built and fracture surfaces. When coupled with EBSD and EDS, the quantification of chemical compositions and identification of specific element-rich phases made it a powerful tool for use in materials characterization. Unfortunately, when accounting for very low atomic number impurities such as carbon, oxygen, nitrogen and hydrogen EDS becomes less reliable. Instead, inert gas analysis (IGA) was used to provide elemental composition of the powders and AM components for these impurities. TEM was used to characterize nanoparticle inclusions with high resolution. All of these methods will be combined to provide an extensive, full assessment of microstructural development as a result of the LPBF process.

1.4.2 Mechanical Testing

The as-printed pure molybdenum and Mo-0.1SiC specimens were subjected to three-point bending and nano-indentation hardness measurements. Nano-indentation hardness testing measured the Vickers hardness (H_V) per International Standard Organization (ISO) 14577 [56]. Three-point bending testing measured the flexural strength of the materials in the transverse direction which results in testing across the build direction. Strength of pure molybdenum specimens were compared to that

of Mo-0.1SiC to evaluate the influence of carbide additions.

1.4.3 Positron Annihilation Spectroscopy

In a novel use of PAS techniques, the microstructures of the as-printed specimens were analyzed to distinguish between print parameters and compositions. The parameters associated with the PALS measurements were correlated to the known differences in the microstructures of pure molybdenum and Mo-0.1SiC as understood from the preceding microstructural characterization techniques. PALS has been used only sparingly for AM materials and this analysis was the first to apply the technique to LPBF molybdenum.

1.5 Organization of Dissertation

The goal of this dissertation is to document and expound upon the material presented in this first chapter. The following chapters are organized as follows.

Chapter 1 provides the background and motivation for the research and results presented in this dissertation.

Chapter 2 introduces the properties, uses, background, and additive manufacturing of refractory metals and explores the current state of LPBF molybdenum in the literature.

Chapter 3 follows with a discussion on the theory of positrons, their interactions with matter, and the history and practicality of the PAS techniques used during this research.

Chapter 4 covers the traditional tools used to fully characterize the AM molybdenum and Mo-0.1SiC specimens. The chapter consists mostly of the work included in the original research article published in *Crystals*, with some additional data and analysis that was conducted after publication.

Chapter 5 includes the characterization of AM molybdenum and Mo-0.1SiC via PALS. The chapter consists mostly of the work included in the original research article published in *Materials*, with some additional data and analysis that was conducted after publication.

Chapter 6 provides options for further research and areas to continue based on conclusions drawn from Chapters 4 and 5.

II. Molybdenum: Production and Characterization

Broad understanding of many different specialties is inherent in the field of materials science, and as such, an introduction and discussion as a prelude to the work outlined in this dissertation is provided as foundational information. The AM of refractory metals encompasses a range of chemical and mechanical engineering related topics and many will play a significant role in support of the Problem Statements in Chapter 1.

The microstructure of a metal is dependent on the production methods involved and an understanding of the differences between traditional powder metallurgy (sintered, arc-casted, and electron beam melted) and AM molybdenum illuminates the need for advanced characterization techniques, and the potential best uses for these, both in-situ and post-build.

The background begins in Section 2.1 with a discussion of the material properties that are inherent to molybdenum and give it the properties and applications that make it desirable for enhanced manufacturing techniques like LPBF. Sections 2.1.1 and 2.1.2 begin at the simplest level and describe the electronic and crystal structure of molybdenum and other refractory metals that provide beneficial properties. The oxidation of pure molybdenum and the potential influences from added silicon and carbon are discussed in detail in Section 2.1.3 which is followed by a description of the solubility of silicon, oxygen, and carbon in molybdenum. Section 2.2 outlines the standards used to traditionally manufacture molybdenum and the heat treatments used to prepare the production components. Also present is a discussion on LPBF in general, including Section 2.2.2.3 which discusses key concepts behind laser absorption and the published work to improve the laser-powder coupling. The chapter concludes with a discussion on the current state of AM molybdenum.

2.1 Properties of Molybdenum

Molybdenum is part of the exclusive group of refractory metals that also, without a broader definition, includes niobium, tantalum, tungsten, and rhenium. Refractory metals have significant advantages over other metals with a high melting point (all above 2000°C) and excellent hardness and strength at room temperature. Refractory metals are also chemically inert to most non-oxidizing corrosive environments [57], making them highly wear- and corrosion-resistant. Molybdenum does not have the highest melting point among the five refractory metals; however, it is softer and more ductile allowing for superior machinability and it possesses a lower density than tungsten and the lowest thermal expansion coefficient of any element which is desirable for certain applications. The macroscopic properties of materials are dependent on the chemistry at the microscopic level. Even further, the structure of materials are a function of interactions at the atomic level. The following section is presented to provide sufficient background on molybdenum and its interactions with the elements relevant to this research.

2.1.1 Electronic Structure

The electronic structure of transition metals sets them apart from the rest of the elements in the periodic table and gives them unique properties, such as high melting temperatures, due to small energy differences between the *ns* and *(ns-1)d* subshells. Unlike non-transition metals and non-metals, where bonding occurs between electrons in unfilled s and p orbitals, in transition metals the electrons in the $(ns\text{-}1)d$ and the ns orbitals are considered to be valence electrons and participate in chemical bonding. These electrons can form covalent-like bonds with surrounding atoms yielding very high strength interactions and high melting points. The electron configurations for the five refractory metals are provided in Table 2.1.

Table 2.1. The electronic configurations of the refractory metals.

Element	Atomic Number	Electron Configuration
Nb	41	$[Kr]4d^45s^1$
Mo	42	$[Kr]4d^55s^1$
W	74	$[Xe]5d^46s^2$
Re	75	$[Xe]5d^56s^2$

Most notable about the electronic structure of the refractory metals that the (ns-1)d subshells are only partially filled while the ns subshells contain electrons and are, in all cases save for molybdenum and niobium, filled. This occurs because the ns subshell is lower in energy than both the (ns-2)f and the (ns-1)d subshells. All period six elements from lanthanum (atomic number 57) to gold (atomic number 79) experience some form of unfilled valence electron shells. This results in additional electrons that are available for chemical bonding. Generally, the electron behavior within a solid metal can be viewed through the electron-sea model wherein the solid metal is assumed to be a three-dimensional network of cations surrounded by delocalized electrons that are free to move throughout the network. Metallic bonding is generally quite strong due to the large amount of electrons available for bonding interactions. The significant energy required to break the bonding behavior results in high melting temperatures.

Molecular orbitals in metals, over the entire crystal, consolidate into a bonding band and an antibonding band due to overlap of valence orbitals. Transition metals in particular have s and d shells which combine to give six molecular orbitals that can hold up to 12 total electrons. Half of these electrons will be bonding and the other half will be antibonding, but this varies with atomic number. Molybdenum has six electrons in these orbitals available for bonding: five from the $4d$ subshell and one from the $5s$ subshell. Interestingly, this aligns with what is expected to be the maximum bonding configuration as all the bonding orbitals will be full compared to none of the antibonding orbitals. The hardness, high melting temperature, and

density of refractory metals are a direct consequence of this electronic behavior as niobium, tantalum, tungsten, rhenium, and molybdenum are all around this maximum bonding configuration. To contrast this behavior, mercury (also a period six element) has all the bonding and antibonding orbital filled, resulting in the property of being a liquid at room temperature. In addition to impacting basic macroscopic properties, experimental studies and theoretical calculations on phase stability of the transition metals have repeatedly indicated that the crystal structure is dependent on the number of valence d electrons per atom.

2.1.2 Crystal Structure

Transition metals predominantly have either a body-centered cubic (BCC), face-centered cubic (FCC), or hexagonal close-packed (HCP) crystal structure. The unique electronic environment in the valence shells of transition metals results in a pattern of HCP-BCC-FCC crystal structures across rows 3 through 7 of the periodic table.

Of the three common crystal structures, FCC and HCP are considered to be close packed structures as the coordination number, or the number of nearest atoms, is the highest among the known crystal lattices. The BCC structure is not considered close packing because its coordination number is eight as opposed to twelve for both the HCP and FCC structures. The determination of which crystal structure is preferred is dependent on the free energy involved in the packing, with the lower energy being adopted. As pressure or temperature changes, it is possible for a metal to undergo a phase transition where its crystal structure changes to another lattice type that minimizes the free energy in the system. The ratio of valence d electrons per atom determines the most stable crystalline structure for a specific element. Moving from left to right across the transition metal periods, the amount of valence d electrons increase, thus increasing this ratio. The free energy of the BCC crystal structure is

lowest for Group 5 and 6 metals [58]. In most of the transition metals, the energetically favorable crystal structure changes with increasing pressure which causes an electronic structure change that mimics an increase in the valence d electron-to-atom ratio. This phenomenon is known as the s-d transition [59] and is due to the spatial orientation of the s and p states. The s and p extend further from the nucleus and are more strongly effected by the high pressure than the d orbitals which are held closer to the atomic core. During this process, the s and p states increase in energy to become more d-like in nature. This transition does not induce large changes in the electronic structure however a move to the right by one periodic group has been experimentally observed in the lighter transition metals, namely titanium and zirconium, where their normal HCP structure transforms into a distorted BCC structure of vanadium and niobium at high temperatures [60]. Niobium has been shown to remain in the BCC structure up to 1000°C through multi-cell Monte Carlo computational analysis [61]. The heavier, central transition metals like molybdenum and tungsten do not exhibit this behavior and remain in their BCC at high temperatures and pressures, although the transition has been predicted in molybdenum by theoretical free energy calculations [58].

The BCC crystal structure is responsible for the numerous benefits that ensure molybdenum is a highly sought after additive to, or main constituent of, many different industrial and technological components; however, it is also responsible for deleterious behavior during AM processes due to decreased room temperature ductility. While the FCC structure tends to be more stable at high temperatures as it is a close-packed system, the BCC metal offers superior slip-resistance due to a smaller number of close-packed planes. This results in a metal that remains strong at high temperatures, but is less ductile at low temperatures. A common property among BCC metals is a high ductile-to-brittle transition temperature (DBTT) where the

metal is only ductile at elevated temperatures. Complicating ambient temperature ductility is the lack of any truly close-packed planes in the BCC lattice where, in a simplified model, none of the atoms are touching one another along the slip planes as they do in FCC metals. In order to activate the slip planes, energy needs to be added to the system. Below the DBTT there is not enough thermal energy available to activate the slip planes and promote ductility.

The BCC structure of molybdenum greatly affects the ductility of the metal at low temperatures; however, it drastically improves the high temperature strength. Ductility is a measure of a material's ability to undergo plastic deformation prior to fracture. The mechanism of plastic deformation is the process of slip. Slip occurs in crystal materials along preferred planes and in preferred directions. Each crystal system has preferred slip systems, the combination of a plane and direction. Deformation occurs through the movement of dislocations along slip systems containing close-packed planes. For BCC materials without close-packed planes, only certain systems can act as glide planes. The preference of plane is affected by various external factors such as temperature, strain rate, and sample preparation. In molybdenum the slip systems are shared with tungsten and include the <111> slip direction in combination with either the {110} or {211} slip planes. Deformation twinning in molybdenum can compete with the slip process in molybdenum at high strain rates and low temperatures. Generally, deformation twinning has a higher activation energy than slip at low and medium strain rates. If favorable, twinning can lead to large amounts of plastic strain [62]. Deformation twinning can occur more readily in the presence of stress concentrators, such as nanoparticle inclusions [63]. Due to deformation requiring planes of atoms to slip over one another, this becomes more difficult in the BCC structure without added energy.

2.1.3 Oxidation

Despite the numerous benefits presented by the BCC crystal structure, use of pure molybdenum is limited in high temperature operations due to rapid oxidation at elevated temperatures, to include those seen in LPBF, and requires the inclusion of so-called oxygen-getters, that will preferentially oxidize over molybdenum.

Two predominant stoichiometric oxides have been confirmed experimentally: molybdenum dioxide, MoO_2, and molybdenum trioxide, MoO_3 [64]. The oxidation process of molybdenum in oxygen occurs in four distinct phases. In the first phase molybdenum is oxidized to its +4 oxidation state and forms MoO_2 by the following equation,

$$Mo(s) + O_2(g) \rightarrow MoO_2(s). \tag{2.1}$$

Up until about 400°C the MoO_2 scale is relatively stable and adherent to the surface of the molybdenum substrate. During this phase, the rate-controlling process is the diffusion of either the metal or oxygen through the oxide layer. The second phase begins above 500°C, where the process is no longer controlled by diffusion in the bulk, but instead the reaction rate between oxygen and the dioxide on the surface. The surface, covered in a MoO_2 scale, becomes further oxidized to MoO_3 where molybdenum is in its +6 oxidation state by the following equation,

$$2MoO_2(s) + O_2(g) \rightarrow 2MoO_3(s). \tag{2.2}$$

The vapor pressure of the trioxide is relatively high and it volatilizes from the surface such that the oxide scales are not protective. In the third phase, above the melting temperature of MoO_3 (795°C) the oxidation rate increases further because diffusion of oxygen through the liquid oxide is higher than the solid [57]. The fourth and last phase occurs at very high temperatures where the oxide volatilizes as quickly

as it is formed on the surface and the oxidation rate is only governed by how quickly the oxygen can impinge on the surface of the molybdenum [65]. While these reactions are thermodynamically favored at room temperature and kinetically favored at elevated temperatures, induced reduction of molybdenum oxides can occur in the presence of hydrogen.

The reduction of molybdenum oxides is an important process in the production of powdered molybdenum. As will be discussed in Section 2.2.1, due to high melting point and volatility, normal production methods are not used and it is produced through powder based techniques. Molybdenum powder is produced through a two-stage process that reduces sequential oxides to pure molybdenum:

$$MoO_3(s) + 2H_2(g) \rightarrow MoO_2(s) + H_2O(g), \tag{2.3}$$

$$MoO_2(s) + 2H_2(g) \rightarrow Mo(s) + 2H_2O(g). \tag{2.4}$$

At temperatures above 400°C and in the presence of CO, MoO_3 can be reduced to MoO_2, albeit slowly at this temperature. At temperatures above 810°C, MoO_2 is further reduced to molybdenum carbide (Mo_2C) by the following reaction [66]:

$$2MoO_2(s) + 6CO(g) \rightarrow Mo_2C(s) + 5CO_2(g). \tag{2.5}$$

More recent literature points to a two-step reaction stoichiometry and mechanism for the reduction of MoO_3 to MoO_2, and further reduction of MoO_2 to Mo_2C that is shown in the following reaction [67]:

$$MoO_3(s) + 0.51C(s) \rightarrow MoO_2(s) + 0.485CO_2(g) + 0.025CO(g), \tag{2.6}$$

$$MoO_2(s) + 4.175C(s) \rightarrow Mo_2C(s) + 2.35CO(g) + 0.825CO_2(g), \qquad (2.7)$$

as determined through thermogravimetric analysis. The preparation of Mo_2C requires 5.87 wt% carbon which is significantly more than the carbon present in the 0.1wt% silicon carbide. Oxygen levels during this work were held below 300 ppm which is about a third of the measured oxygen present in the LPBF build chamber [67].

The formation of Mo_2C has been documented in LPBF research. Braun et al. [34] demonstrated that at weight percentages of carbon from 0.25% up to 2.2 wt%, Mo_2C is formed during consolidation.

There has not been much work in the literature on the addition of hydrogen to the build chamber atmosphere of LPBF machines. Kemnitz et al. [68] added 3% hydrogen to argon in order to print pure tungsten and saw improved bend strength potentially due to an increased concentration of oxides found in the material. The oxides themselves demonstrated a needle-like structure that is more commonly associated with $WO_{2.9}$ and $WO_{2.72}$ indicating reduction of WO_3 occurring during the printing process [68]. The influence of hydrogen as a component of the shield gas mixture has been investigated on light metal alloys as well. The addition of 2% hydrogen to the argon shield gas for the printing of WE43, a magnesium alloy, significantly reduced the variation in print density and form factors of consolidation components [69]. Both of these studies represent initial, exploratory work; however, they show the benefits of a reducing atmosphere in the consolidation of metals through LPBF. Control of the build chamber environment has been shown to improve the consolidation process for refractory metals, but it is not the only method of limiting oxidation during the build process.

Additions to the refractory metal powder systems that have a higher affinity for oxygen are the so-called "oxygen-getters" and have improved LPBF functionality for

refractory metals like tungsten and molybdenum. The premise behind these additions are that their oxidation reactions are more favorable than the oxidation of molybdenum and will take a portion of the oxygen out of the system. For molybdenum, the main addition seen in the literature concerning LPBF is carbon [29, 32, 33, 34]. Carbon reacts with oxygen to form both carbon monoxide (CO) and carbon dioxide (CO_2). CO can further react with oxygen to form CO_2. Both species are gases and leave the surface of the consolidated material. In support of the research objectives outlined in Chapter 1, silicon carbide was added to the molybdenum powder prior to printing. The specific processes behind the oxidation of silicon carbide are described in Section 4.3, but the thermodynamics behind the oxidation preference for silicon and carbon over molybdenum will be discussed here.

Determining the thermodynamic preference of a certain chemical process is done by calculating the associated standard free energy change. An informative way to show these free energy changes and thus determine the thermodynamic driving force is through an Ellingham diagram. The diagram, a plot of the change in Gibbs free energy (ΔG) with temperature, will show the relative stabilities of the selected metals and their oxides, and in turn the thermodynamic preference between the oxidation reactions themselves. The lines in Ellingham diagrams are determined through the equation for Gibbs free energy,

$$\Delta G^\circ = \Delta H^\circ - T\Delta S^\circ, \tag{2.8}$$

where ΔH is the enthalpy and ΔS is the entropy. Enthalpy measures the energy that is either absorbed or released in endothermic and exothermic reactions and processess, respectively. Entropy measures the disorder of a system, i.e. a change in entropy will be positive when a phase change occurs from a liquid to a gas. Enthalpy and entropy are functions of the constant pressure heat capacity, which itself is a

function of temperature. While both enthalpy and entropy are relatively stable with temperature this only applies to small temperature changes, which are present during the LPBF process.

The Ellingham diagram presented in Figure 2.1 provides an avenue for determining the relative ease of reducing a given metallic oxide to metal. Ellingham diagrams are used for determining the equilibrium partial pressure of oxygen with the metal oxide at a given temperature. For the powder system used in this research, there are three elements (molybdenum, carbon, and silicon) that oxidize during the printing process and it is important to understand the thermodynamic preference at which this oxidation takes place. Figure 2.1 uses the thermodynamic quantities [70] shown in Table 2.2 to give a position of the line that shows the relative stability of the oxide as a function of temperature. It should be noted that, despite not being shown in Figure 2.1, at temperatures above the boiling point of the solid oxides, the lines for those reactions will change in slope due to the melting or vaporization of any of the species involved. The line for the oxidation of carbon to carbon dioxide is, coincidentally, horizontal due the stoichiometrically balanced reaction showing that a solid reacts with one mole of gas to produce a mole of gas. In the case of carbon oxidation to carbon monoxide two moles of solid react with one mole of gas to produce two moles of gas and results in a significant increase in the entropy.

If a line is positioned below another, the given metal on the lower line will reduce the oxides of the metals shown above it. As the lines for the oxidation of carbon into carbon monoxide is negatively sloped while the molybdenum oxides are positively sloped, at the elevated temperatures seen in the powder system during LPBF, the carbon oxidizes and reduces the molybdenum oxide to pure molybdenum. Similarly, the lines of the silicon oxides are lower than molybdenum. Comparing the silicon and carbon oxidation line indicates that silicon will also reduce carbon oxides under

Table 2.2. Standard thermodynamic properties of the materials used in this research at 298.15 K. (s) and (g) denote the solid and gas phase, respectively.

Chemical Formula	ΔH_f° (kJ/mol)	ΔS_f° (J/mol · K)
Mo (s)	0.0	28.7
MoO_2 (s)	-588.9	46.3
MoO_3 (s)	-745.1	77.7
C (s)	0.0	5.74
CO (g)	-110.525	197.674
CO_2 (g)	-393.509	213.74
Si (s)	0.0	18.83
SiO_2 (s)	-910.94	41.84
O_2 (g)	0.0	46.3

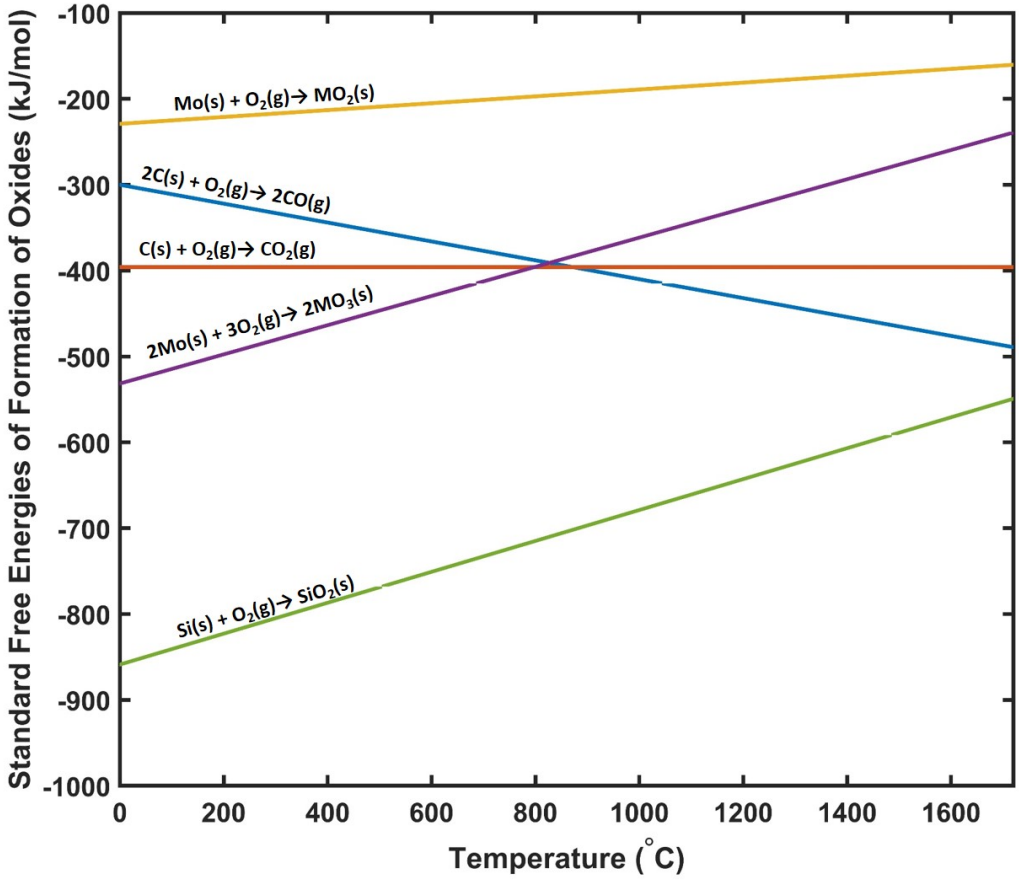

Figure 2.1. Ellingham diagram depicting the standard Gibbs free energy for the oxidation reactions of interest in this research as a function of temperature.

thermodynamic equilibrium.

Ellingham diagrams assume that equilibrium is achieved at a particular temperature. The rapid cooling and changing diffusion rates during the LPBF process indicate that achieving equilibrium is unlikely. However, experimental and theoretical oxidation studies have shown that bulk oxidation follows thermodynamic preference [71]. Oxidation occurs rapidly during the LPBF process, even at low partial pressures of oxygen [72], and although a simple approximation, Figure 2.1 provides evidence for the use of silicon carbide as an oxygen-getter in the molybdenum powder system.

2.1.4 Solute Behavior in Molybdenum

While oxidation occurs rapidly at the molybdenum surface, the solubility of oxygen within the bulk material is very low and after consolidation the oxides are found to have segregated to the grain boundaries. The molybdenum-oxygen phase diagram demonstrates this low solubility and is shown in Figure 2.2 [73].

The partial pressure of oxygen present in the build chamber is purged by the build chamber atmosphere and kept under 1000 ppm, but there is oxygen present on the powder particles themselves, due to the high surface area, that is available for oxidation. Figure 2.2 shows that oxygen has a negligible solubility in solid molybdenum and as the primary molybdenum phase forms during solidification, it is pushed to the surrounding liquid phase which solidifies by eutectic transformation. In this partially melted zone, if there is enough oxygen present, it can embrittle the material and result in hot cracking. The oxygen present in the melt solidifies as molybdenum oxide rather than remain in the gaseous phase. The eutectic regions where these oxides form become grain boundaries in the consolidated material and, due to their brittle nature, are deleterious to the overall mechanical properties.

The Hume-Rothery rules state that a substitutional solute should have an atomic

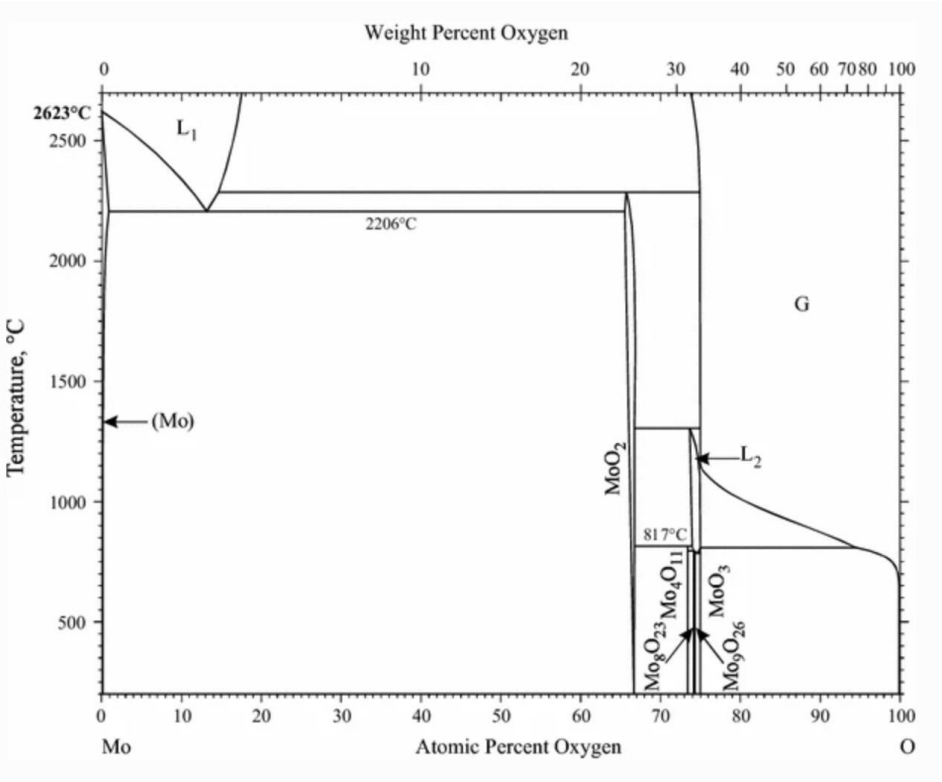

Figure 2.2. Molybdenum-oxygen binary phase diagram. Permission to use this figure has been granted by the publisher.

radius that differs by no more than 15%, whereas for interstitial solutes, the atomic radius of the solute atoms should be less than 59% of the radius of the solvent atoms. The differences for oxygen, carbon, and silicon are 74%, 65% and 42%, respectively. Oxygen and carbon are interstitial solute atoms in molybdenum; however due to their large differences in electronegativity and valencies, solubility is limited and intermetallic compounds form if the solute concentration increases [74]. The molybdenum-carbon phase diagram is shown in Figure 2.3 [75]. The molybdenum-silicon phase diagram is shown in Figure 2.4 [76].

The radius of silicon is too large to be considered an interstitial solute atom in molybdenum, and is known for contributing a solid solution strengthening effect. Silicon is, however, rather small to act as an easy substitutional atom and first principle calculations show that the solubility is limited as the bonds formed between the sili-

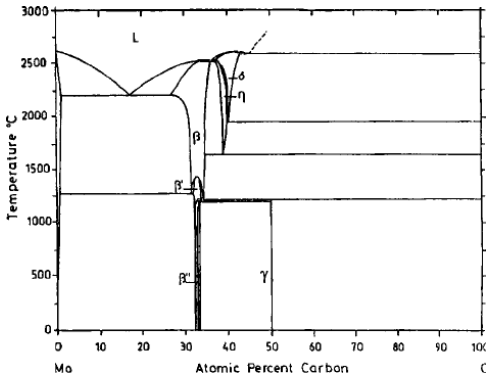

Figure 2.3. Molybdenum-carbon binary phase diagram. Permission to use this figure has been granted by the publisher.

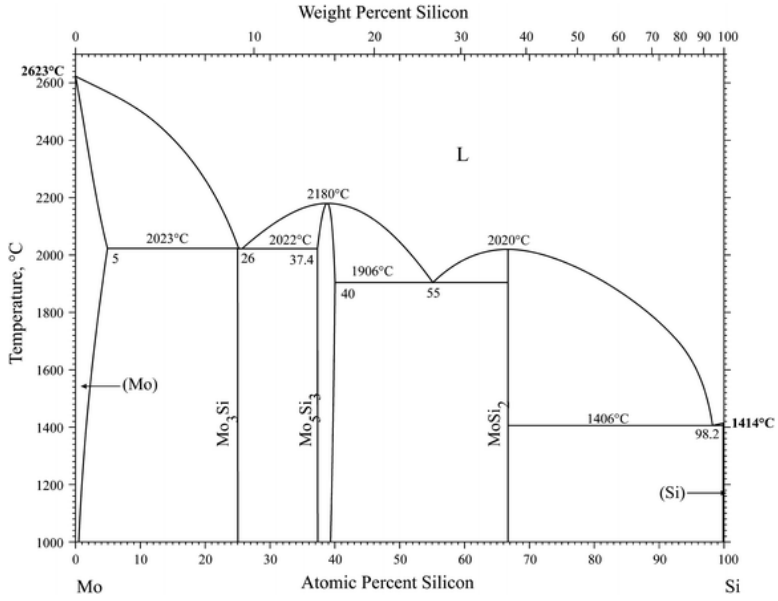

Figure 2.4. Molybdenum-silicon binary phase diagram. Permission to use this figure has been granted by the publisher.

con and molybdenum do not energetically balance with the energy cost of removing a molybdenum atom from the lattice [77]. Due to their limited solubility in molybdenum, it is unlikely to find these smaller atoms well distributed throughout the bulk of the metal. More likely there will be segregation to the grain boundaries as the melt-pool cools and solidifies.

2.1.5 Strengthening Mechanisms

A proven solution to strengthening molybdenum is through adding dopants, whether through pure alloying or the addition of oxides. The addition of lanthanum oxides to molybdenum wire improved the tensile strength through dislocation, or strain hardening [78]. TZM, an alloy of titanium (0.50 wt%), zirconium (0.08 wt%), carbon (0.03 wt% and molybdenum (balance), experiences higher strength due to the formation of secondary phase carbides (precipitation hardening) and a finer grain structure (grain-boundary hardening) [79]. The limited solubility of silicon, carbon, and oxygen in molybdenum likely rules out a strengthening effect due to solid solution hardening; however, there are numerous other mechanisms still available to both the pure molybdenum and Mo-0.1SiC specimens that could influence the mechanical properties.

Grain-boundary strengthening, also known as Hall-Petch strengthening, results from changing the grain size of a material. Grain boundaries impede dislocation motion resulting in a higher activation energy for deformation. Smaller average grain sizes indicate the presence of more grain boundaries and dislocation pinning points resulting in the increased strength of a metal. The development of a secondary phase could lead to dispersion or precipitation hardening depending on the size of the secondary phase particles. The presence of a secondary phase creates strains within the crystal lattice impeding dislocation. Incoherent secondary phases that create mismatches in the crystal lattice are more effective at impeding dislocation motion than coherent phases which can be crossed by more favorable processes. Finally, strain, or work, hardening can be used to increase dislocation density. A microstructure containing a high dislocation density generates more strain in the lattice where dislocation entanglement and intersections, or jogs, act as another form of pinning points to impede dislocation motion, preventing slip, and increasing the strength [74]. Gen-

erally in traditionally manufactured metals these strengthening mechanisms can be controlled with very high precision through post-processing heat and work treatments. For as-built LPBF materials, the development of these mechanisms is governed by the processing parameters.

2.2 Manufacturing and Processing

The following section provides information on the fabrication methods available for producing molybdenum components. The material properties of molybdenum place inherent limitations on production methods; however, these limitations provide an opening in the design space for alternative fabrications methods, such as LPBF. Section 2.2.1 describes the methods by which molybdenum is currently produced and the associated microstructure and mechanical properties. Section 2.2.2 introduces the terminology and background on the LPBF technique and provides an update on the current state of molybdenum produced by this method available in the literature.

2.2.1 Traditional Material Processing

The volatility of molybdenum oxides at relatively low temperatures (>550°C) prevents the use of methods such as smelting for molybdenum production. Generally molybdenum components are produced through sintering, arc casting, and electron beam melting techniques. Sintered products are the most common commercial form. Arc cast products are significantly more expensive while electron beam melting components are essentially laboratory grade and prohibitively expensive [80]. LPBF offers an adaptable and relatively inexpensive avenue for commercial production if the issues mentioned in Section 2.2.2 can be solved.

2.2.1.1 Fabrication

The three traditional routes for producing molybdenum: sintering, arc casting, and electron beam melting, are all powder metallurgy methods that require powder produced through a two-stage reduction process. Molybdenum is generally found in nature as molybdenite (MoS_2) ore which contains roughly 59% molybdenum by mass. Preparation of the raw ore requires chemical and mechanical processing to separate the MoS_2 from surrounding minerals followed by oxidation to MoO_3 and sulfur dioxide through a roasting process. The oxide is either converted to ammounium dimolybdate or reduced directly by hydrogen to the lower oxide, MoO_2, before the second stage of the reduction process that reduces MoO_2 to pure molybdenum powder. The morphology of the powders are controlled during this part of the process. Further processing of the powders are accomplished through the three production methods mentioned above [80]. Following consolidation of the powder the pressed and sintered, or cast, ingots are formed through mechanical means.

2.2.1.2 Mechanical Finishing and Heat Treatments

Pressed and sintered molybdenum was used as a standard for positron measurements presented, so the discussion on mechanical finishing, heat treatments, and mechanical properties in this section will be limited to rolled plates. Compared to the arc-cast and electron beam melting methods, pressed and sintered molybdenum lacks rigid control of grain boundary formation and behavior. Post-consolidation, and during the rolling process, the metal ingot is passed through one or more pairs of rollers to reduce the thickness. This can be done above or below the recrystallization temperature.

During the hot rolling process the molybdenum is kept above the recrystallization temperature which allows for the deformed grains to recrystallize during the process.

The recrystallization temperature of molybdenum is around 900°C and hot rolled molybdenum kept above this temperature will have an equiaxed microstructure. The hot rolling process is generally easier due to the increased workability of the metal. Grain sizes of sintered and pressed molybdenum are smaller than those of the other two production methods, but they can be increased during the hot rolling process. The rolling of pure molybdenum at 1700°C and 2300°C resulted in significant grain size increases [81]. While the larger, recrystallized grains of hot rolled molybdenum result in a material with reduced internal stresses and increased ductility compared to cold rolled molybdenum, the strength and hardness are negatively impacted. The process of cold rolling decreases grain size through mechanical work and does not provide the thermal energy required for recrystallization or grain growth. According to the Hall-Petch equation,

$$\sigma_y = \sigma_0 + \frac{k_y}{\sqrt{d}}, \tag{2.9}$$

where σ_y [MPa] is the yield strength, σ_0 [MPa] represents the stress at which dislocation movement begins, k_y [MPa/μm] is a material constant, and d [μm] is the grain diameter, a reduction in the grain size increases the strength of the material. The molybdenum plate used as a standard for this research was manufactured per ASTM-B-387-18 [82]. The EBSD map is shown in Figure 2.5 and has a dense, equiaxed, microstructure with a strong <111> fiber texture. The average grain diameters were determined to be 4.66 $\pm$0.28μm.

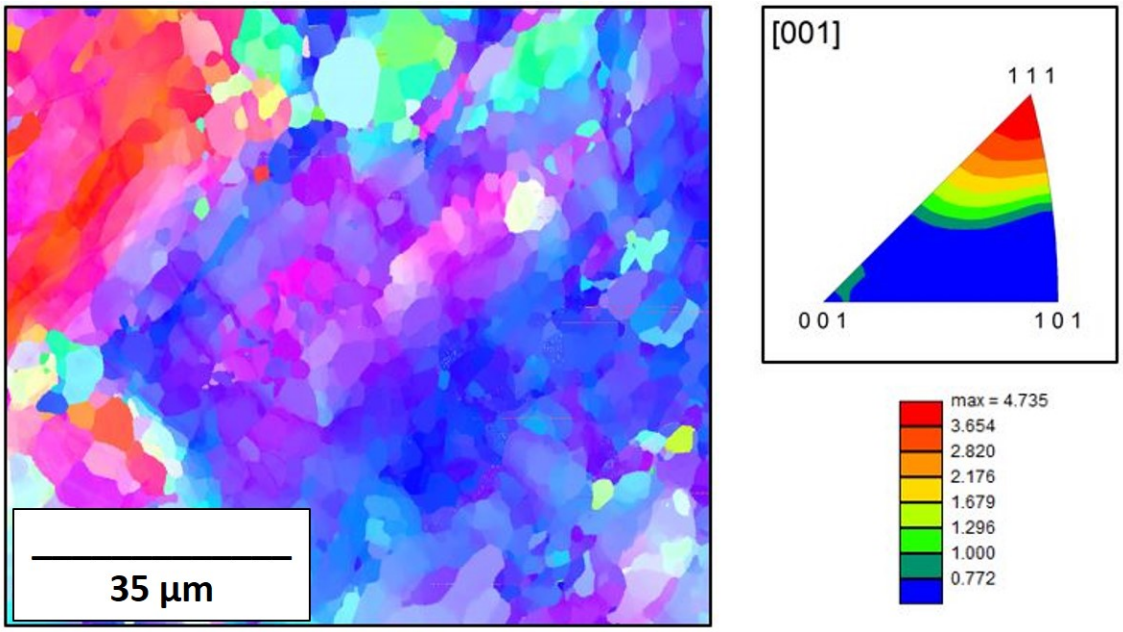

Figure 2.5. EBSD inverse pole figure (IPF) map for traditionally manufactured molybdenum with determined texture intensity.

The kernel average misorientation map (KAM), Figure 2.6, measures the local grain misorientation in the traditionally manufactured molybdenum. Areas of higher misorientation are indicated by the color green. Generally, misorientation is higher in areas of high dislocation density or lattice distortion. Figure 2.6 exhibits very little green within the grains, indicating low distortion and residual stress.

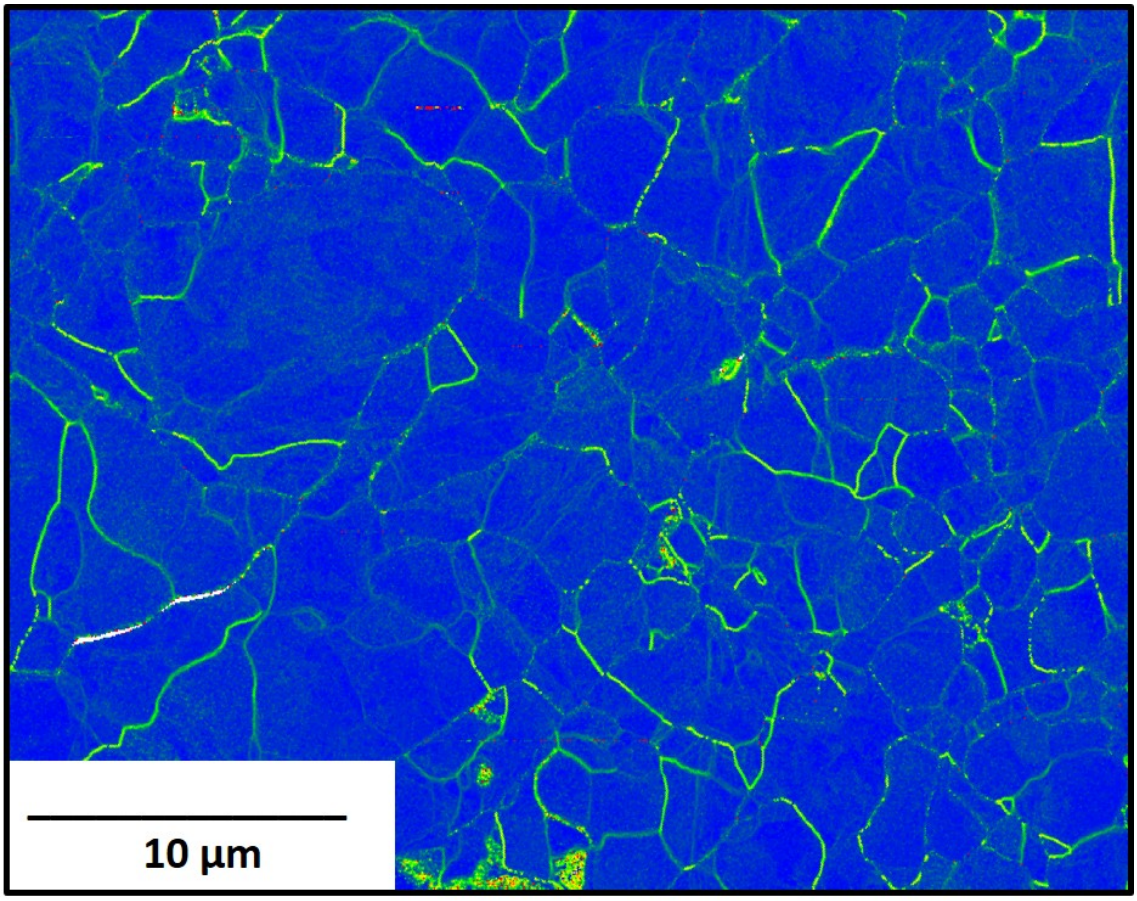

Figure 2.6. KAM map for traditionally manufactured molybdenum.

By the standard, ASTM-B-387-18 [82], the molybdenum products are to be delivered in a wrought and stress-relieved state. The molybdenum bar used for these initial treatments was likely rolled and only acceptably stress-relieved, with very little grain growth, to yield the displayed microstructure.

2.2.2 Additive Manufacturing

Additive manufacturing is a large family of processes that have become known for their ability to produce complex three-dimensional components in a more time, material, and cost effective manner than traditional subtractive manufacturing techniques. There are a variety of AM processes that can be broken down into different categories,

but this research will focus on the LPBF process. Commercially this process goes by many names including selective laser sintering (SLS), selective laser melting (SLM), direct metal laser sintering, and LPBF. A basic understanding of the LPBF technique, process parameters, and build chamber environments is vital to sifting through the vast amount of work published on the LPBF of refractory metals.

2.2.2.1 Laser Powder Bed Fusion

The first successful application of laser-based AM to metals was reported in 1990. This work applied the SLS process to copper, tin, and lead [83]. The SLS process differs from LPBF or SLM because full melting of the metals is not achieved. The LPBF process uses a high-power laser to melt successive layers of nano- to micron-sized powders, essentially welding layers of metal together into a three-dimensional structure. Software such as MATLAB or computer aided design programs are used to develop the designs. The designs are loaded into the printer and the build process is mostly hands-free and automated. AFIT has a Concept Laser Mlab Cusing 200R 3D metal printer, produced by General Electric in Boston, Massachusetts. This printer has a 200W Yb:YAG fiber laser that produces a wavelength of 1080 nm and a focus diameter of around 50 μm [84]. The standard atmosphere within the build chamber is pure argon. Oxygen levels are maintained at $\leq$1000 ppm. Recently, modifications were made to introduce a 3% hydrogen/97% argon atmosphere to reduce oxygen levels even further.

A useful benefit of LPBF is the ease of which combinations of different powder materials can be mixed and printed. The first step in the AM process is preparing the powders. If the build is a pure metal, the powder is simply placed into the build chamber of the printer and the build process can begin. If a combination of powders is desired, the powders are separated into 200 g portions according to the

weight percentages of the desired combination. This is the ideal amount of powder for mixing in the FlackTec, Inc Speed Mixer. Powders are added by wt% meaning that a 200 g quantity of Mo-0.1SiC would contain 199.8 g of molybdenum and 0.2 g of silicon carbide. The Speed Mixer is designed to accept disposable sample cups that limit cross contamination. Each mixing run takes approximately a minute. Longer mixing times are unadvised due to the heat generated through friction between the mixing metal particles. After each mixing run the samples are allowed to cool before any subsequent mixing. Multiple runs are often needed to ensure a sufficient homogeneous mixing. Once mixed and cooled the powders are placed into the powder chamber of the printer.

The build process begins with the input of the build design, addition of powders, and selecting of process parameters. About 2000 g (10 mixing cups) worth of metal powder is needed for a 10 mm tall build. After the printer receives a thorough cleaning to ensure no cross contamination of powders, the powder chamber is lowered to accommodate the new powder. For the prints conducted in support of the research objectives in Chapter 1, the build chamber contained a steel build plate with four round copper inserts that the build are actually printed on. Copper has been shown by work at AFIT to be the best substrate for molybdenum-based prints due to its high thermal conductivity.

At the initiation of the build, the plates in the build chamber are first exposed to a few laser passes. This melts the copper inserts in the same manner (i.e. scan speed and pattern) that the prints will be processed and prepares them to accept the metal powders. The powder is introduced to the build chamber by a wiper blade. The first few layers of powder are printed using standardized parameters to ensure proper cohesion to the build plate and successful melting is occurring. The build chamber plate lowers and the powder chamber plate raises layer after layer. Once adhesion

to the build plate is confirmed through visual inspection, the desired parameters are input and the rest of the print is automated and hands-free. Each layer of powder is exposed to the laser and melted. The melting process remelts a few layers underneath the surface which ensures the new layer is welded to the rest of the component. With every pass of the wiper blade, excess powder is expelled to an overflow container. At the end of the build, the printed components are surrounded by unmelted powder. This powder is added to the overflow container during the cleanup process and this powder can then potentially be recycled. Components are removed from their build plates through electric discharge machining (EDM) at the AFIT Model Shop.

2.2.2.2 Process Parameters

The process parameters that can be adjusted for each build are the laser power, scanning speed, hatch spacing, layer thickness, and scanning strategy. Laser power and scanning speed combine to dictate the energy that is directed at the powder. Increasing the laser power and reducing the scanning speed produces higher energy deposition and reducing the laser power and increasing the scanning speed has the opposite effect. Hatch spacing refers to the distance between scanning paths. A reduced hatch spacing results in remelting of previously melted scan paths. Reducing the hatch spacing can lead to excessive remelting and longer build times, while increasing the hatch spacing can result in poor build quality due to poor welding between scan paths. Layer thickness can be dictated by adjusting the height that the powder chamber floor rises between laser exposures. Excessive thickness can lead to poor melting and welding of the surface layer to the bulk material. A number of these parameters contribute directly to the amount of energy supplied to the powder system. The volumetric energy density (VED) is calculated by Equation 2.10,

$$E = \frac{p}{hvt}, \tag{2.10}$$

where p is the laser power, v is the scanning speed, h is the hatch spacing, t is the layer thickness, and E is the volumetric energy density [85]. The scan strategy of a build is the path that the laser takes across the surface of the build. Theoretically any path is possible, but in practice only a select few are chosen. A continuous scanning strategy, where the laser melts the entire powder surface through a winding path, with a rotation of 90° for each layer has been shown by work at AFIT to reliably produce relatively high-quality surfaces. Printing refractory metals, like molybdenum, requires careful optimization of the printing parameters, as defects and porosity are driven by improperly balanced procedures.

2.2.2.3 Laser Absorbance of Powder Systems

The process parameters of LPBF are easily altered; however the determination of an optimal set of parameters is difficult due to a large design space. Modeling efforts take into account the various parameters described in the preceding section, but another very important component is the absorption of the laser energy by the metal powder system and the nature of its spatial distribution.

The absorbance of a material is the ratio of the absorbed radiation to the incident radiation which is generally determined by transmission spectroscopy measurements. Absorbance is dependent on the wavelength of the laser, powder morphology, build chamber atmosphere, and temperature. The pore structure of the powder particles creates areas where additional radiation is absorbed and metals generally exhibit higher absorbance in the powder form than in the solid form. As the powder begins to melt, the structure of these pores changes rapidly inducing a change in the laser absorbance during processing [86].

Diffusive radiation transport has been used to model laser absorption [87], however, this model assumes a deep powder bed and is not in agreement with the thin layers of the powders used during the LPBF process. Boley et al. [88] conducted a study that focused on the laser absorption of metal powders used in AM processes through a ray tracing model. Initial calculations showed that the absorptivity of a powder is much higher than a flat surface due to scattering contributions. The vast majority of absorptivity occurs within the top two layers of the powder particles and multiple scattering events have a significant impact.

In the case of the molybdenum and mixed Mo-0.1SiC powders, a beam of light cannot be passed through a pressed pellet to make use of transmission spectroscopy and instead diffuse reflectance measurements were conducted. The absorptivity of a material can be measured through diffuse reflectance spectroscopy and it is commonly employed for powders which generally have internal inhomogeneities where scattering plays an important role in the propagation of incident radiation. The Kubelka-Munk (K-M) theory is the most commonly used model to analyze diffuse reflection. The K-M equation is shown in the equation for diffuse reflectance,

$$R_\infty = 1 + \frac{k}{s} - \sqrt{\frac{k}{s}\left(2 + \frac{k}{s}\right)}, \tag{2.11}$$

where k is the absorption coefficient of the powder and s is the scattering coefficient. R_∞ is the absolute reflectance for an infinitely thick sample. For a perfect diffusely reflecting sample, this value is unity [89] The absorption coefficient is given by,

$$k = 4\pi\frac{\kappa}{\lambda}, \tag{2.12}$$

where λ is the wavelength of the laser and κ is the extinction coefficient, an intrinsic property. The K-M model can be simplified so that a ratio of the absorption and scat-

tering coefficients can be determined from only the diffuse reflectance measurements as given by,

$$\frac{k}{s} = \frac{(1 - R_\infty)^2}{2R_\infty}. \tag{2.13}$$

The K-M model treats the scattering coefficient as a constant in regards to the wavelength of the laser, but while it is predominantly a function of particle size and refractive index, not the wavelength of the laser it does vary slightly with wavelength. Additionally, the photon scattering is greatly impacted by the packing density and morphology of the powder itself as demonstrated by Boley et al [88]. The impact of scattering on laser absorbance has been investigated in various metal powders, although no work has been accomplished in this field with refractory metals to date.

Jadhav et al. documented the effect of coating copper particles with carbon and tin [90, 91]. Uncoated copper has high optical reflectivity in the IR range at which LPBF lasers operate. This results in poor coupling of the laser to the powder system. Through calculations using the Fresnel law, it was determined that tin offers much higher optical absorption than copper with values of ∼21% and ∼3%, respectively at 1080 nm. It should be noted that these values are for the flat metals and powders would exhibit much higher values due to the aforementioned scattering effect. By coating the copper with a dilute addition of tin (0.28 wt%), the optical absorbance increased by 32%. Similarly, mixing 0.1 wt% carbon produced an increase of 62% in absorbance.

Tertuilano et al. [92] also addressed LPBF of copper by introducing three different nanoparticles: copper sulfide, titanium boride, and graphene flakes. Graphene showed the largest improvement of absorption with an increase from pure copper at 0.9 to 0.48. This research varied the laser power and showed that the absorptivity decreases as a function of increasing laser power. Copper sulfide has the highest intrinsic

absorptivity among the three additives, but its instability under LPBF conditions resulted in a very minor increase in the mixed powder system.

Both Pannitz et al. [93] and Gu et al. [94] investigated the addition of nano-sized silicon carbide additions to LPBF steel and AlSi10Mg, respectively. Diffuse reflectance measurements showed that the silicon carbide reduced the reflectance of steel powder from 10.2% to 9.2%. The decrease in reflectance was attributed to an increase in surface roughness which improves coupling between the laser and the powder system. This was correlated to atomic force microscopy measurements. Gu et al. showed that the absorptivity of a randomly packed powder bed of pure AlSi10Mg ranged from 0.19 to 0.32 as the laser beam traveled across. The addition of silicon carbide increased this to between 0.37 and 0.59. Again, the increased interactions between the laser beam and powder particles was highlighted.

The small set of previous research that was presented in this section consistently identifies the impact of nanoparticle additions to the LPBF powder system. By increasing the opportunities for the laser beam to scatter off of particles, the absorbance is increased. It is clear that the morphology and stability of the additions under LPBF conditions is important. Research into the influence of laser-powder coupling continue, but has not yet been applied to refractory metals.

2.2.2.4 Current Progress of LPBF Molybdenum

The following section provides a literature review on the current state of the art in the LPBF of pure molybdenum. Initial work into the LPBF of molybdenum began in 2015 [30] and has subsequently received attention by various groups almost every year since. The concerns of the technique became clear very early on and the following work has strove to increase the density, decrease the cracking, and improve the mechanical properties of the consolidated components. The production of molybdenum through

the LPBF process has not received as much attention in the literature as other metals; however, the high-temperature applications for which refractory metals are best suited has driven a considerable amount of research over the last decade.

Faidel et al. [30] first reported research on the LPBF of pure molybdenum in 2015. The work was accomplished using a Concept Laser M2 Cusing printer fiber laser at a laser power of 200 W, a beam diameter of 200 μm, and a nitrogen shield atmosphere. This study investigated the influence of changing printing parameters, namely the scan speed, layer thickness, and hatch spacing. Two parameters were changed while the third was held constant. Comparisons of the printed components were made via optically determined porosity measurements. Results showed that at a laser power of 200 W, and a combination of process parameters yielding a VED of 480 J/mm^3, only a maximum density of 82.5% was achievable. Sets of parameters that yielded higher and lower VED values results in decreased density. Of the three parameters, hatch spacing proved to have the largest uncoupled impact. If the hatch spacing was too large, the weld tracks did not overlap and the powder particles could not fuse together. The scan speed and layer thickness couple together to determine the VED supplied to the powder system. Altering the scan speed alone did not significantly impact the porosity values. Faidel et al. concluded that improving density requires increasing the VED, through an optimized combination of scan speed, laser power, and layer thickness.

The first modeling and simulation of SLM molybdenum was conducted in 2017 by Leitz et al. [95]. This group used a thermo-fluid dynamical multi-phase simulation model to compare the SLM process for steel and molybdenum. Compared to steel, which is a relatively mature SLM product, the melt pool of molybdenum is much smaller due to a high thermal conductivity and the predominant factor affecting printing is the VED. This was followed up by experimental work that demonstrated

the models were able to show good correlation in the scale and trends to the depth and width of weld tracks based on the print parameters chosen. The model did not properly account for the large energy input dependence of the molybdenum powder system which continued to highlight the need for optimized printing parameters. Additionally, the group determined that due to the small molybdenum melt pool, the quality of printed components depends more heavily on the morphological characteristics of the powder than other metals [96].

Wang et al. [31] investigated the impact of increased VED by using a SLM machine with a 400 W laser and a spot size of 75 μm. The powders used were processed prior to printing through dry granulation and plasma spheroidization which increased the powder diameter, packing density, fluidity, and laser absorptivity. The density of these prints, as determined through Archimedes' law, was increased to 99.1%, however cracks were present in the dense samples. The cracks propagated both along and across the weld tracks on the print surface. A columnar grain structure was present in the build direction, but this was partially mitigated by the rotation of the laser scan path each layer.

A predictive model using a statistical design of experiments approach was identified for both aluminum and molybdenum, which were targeted by Bajaj et al. [97] due to high thermal conductivity and difficulty in SLM manufacturing. The model was developed using analytical heat transfer models and experimentation. Through their heuristic model the process parameters: hatch spacing, layer thickness, exposure time, and point distance, were optimized to produce samples with a relative density, determined through optical measurements, of 97.4% at a laser power of 200 W. Cracking was still present in the consolidated specimens and it was noted that additional optimization would be required to reduce balling and the build up of thermal stresses.

Braun et al. [29] investigated the impact of oxygen, the process atmosphere, and

the temperature on the LPBF of molybdenum. It was found that oxygen present on the powder particles prior to printing and in the build chamber during printing increased the oxygen content of the consolidation materials. The oxygen, in the form of molybdenum oxide was found, by TEM imaging, to be segregated to the grain boundaries. Even while heating the substrate plate to 1000°C and limiting the oxygen levels in the build chamber to 20 ppm, molybdenum printed with sufficient laser power was still unable to be produced crack-free. This group concluded that the impurities must be reduced in order to produce fully dense and crack-free molybdenum components.

Following up on this work, Kaserer et al. [32] added 0.45 wt% of carbon to the pure molybdenum mixture in an effort to limit the impact of the oxygen impurities on the grain boundary strength. In order to achieve crack-free, fully-dense molybdenum, the oxygen content of the powders and build chamber was minimized, the substrate was heated to mitigate thermal gradients, and carbon was added to the molybdenum to address the formation of molybdenum oxides. A chemical analysis of the printed components revealed a reduction in the carbon and oxygen content from the starting powder indicating the oxidation of carbon. Dense and crack free SLM molybdenum components with a 340% increase in bending strength were produced through the addition of a small amount of carbon. Reducing the VED or substrate temperature reduced the strength of the material. Density and hardness were also increased and the fracture mode was converted from intergranular to mostly transgranular.

Another investigation by Braun et al. [33] further studied the carbides found in the Mo-0.45 wt% C material. The carbide was found to be a type of Mo_2C that has a solubility for oxygen and a semi-coherent interface with the primary phase of molybdenum. The linkage between the phases resulted in increased interfacial strength promoting stronger ground boundary behavior and preventing cracks. The

solubility of oxygen prevented the segregation to grain boundaries as it was trapped in the carbides.

Higashi et al. [98] conducted an extensive study on the process parameter design space for pure molybdenum, focusing on defect formation and crystallographic texture. Laser power, scan speed, and layer thickness were varied and evaluated individually. The crystallographic texture exhibited a strong <110> texture at high (350 W) laser power and low scan speed (400 mm/s) which changed to a <001> texture at high scan speeds (1000 mm/s). It was determined through this study that scan speed was the only parameter to have a direct effect on the texture. The other parameters such as laser power, layer thickness, and hatch spacing only tangentially affected the texture through the VED. The two main defects found in molybdenum: lack-of-fusion and key-hole pores, were observed but the lack-of-fusion pores disappeared at higher VEDs. The key-hole pores were present through the range of parameters studied. High porosity at extremely low VEDs led to a completely random crystallographic texture.

Oehlerking et al. [99] added 47.5 wt% rhenium to molybdenum and were able to produced as-built components with >98% density. The addition of rhenium increased the strength and ductility over that of the pure molybdenum parts, but an increase in the final oxygen content resulted in persistent cracking. Notably, the columnar structure typically found in the build direction was mitigated and the texture randomized due to the addition of rhenium.

Rebesan et al. [100] provided another investigation of the effect of print parameter variation on the LPBF of pure molybdenum. A laser power of 150 W and scan speeds between 650 and 800 mm/s yielded densities above 97.6%, per the Archimedes method. While considered fully dense, cracks and unmelted particles were still present in the as-built components. The thermal conductivity of the AM components was

found to be about 50% less than traditionally prepared molybdenum owing to the microstructural differences and oxygen impurities.

A new method of preparing the molybdenum powders was studied by Guo et al. [101]. In this study the powders were subjected to a process called the freeze-dry pulsated orifice ejection method. This process was capable of producing spherical powder with controllable particle size and distribution. The powders exhibited improved laser absorptivity due to their shapes and resulted in the consolidated components' lack of unmelted powder particles. The density of the consolidated components and the presence of cracking were not reported. The process did, however, result in an increase in oxygen content. The presence of oxides in the consolidated components inhibited grain growth and increased the hardness.

After the last eight years of research into the LPBF of pure molybdenum, it is clear that the production of fully dense components is possible, however there is not yet a clear way to reduce the oxygen impurities to a level that would prevent the development of cracking throughout the consolidated material. Further research that focuses on the mitigation of oxidation during the print process is warranted in order for the LPBF production method of molybdenum to be commercialized.

III. Positrons: Theory and Experimental Measurements

3.1 Overview

The use of PAS techniques to investigate the microstructure of LPBF molybdenum and Mo-0.1SiC over the course of the work conducted for this dissertation requires an introduction and discussion on the core principles of positrons, their interactions with condensed materials, specifically metals, and the measurement techniques that are employed to discern useful information from the collected data. The chapter begins with a brief history lesson detailing the discovery of the positron in Section 3.2. The interactions between positrons and materials can occur by several different mechanisms from the incredibly quick annihilation of para-positronium (p-Ps) to the much longer lifetime of ortho-positronium (o-Ps). A breakdown of the positron behavior in metal is described in Section 3.4. Section 3.5.2 describes the lifetime deconvolution software package used in this research which is followed by a detailed introduction to the practical aspects of PALS measurements where examples are provided of data that was collected on the pure metals: aluminum, copper, titanium, and molybdenum. Section 3.6 discusses the practical aspects of DBAR measurements to include information on the experimental setup and how the data was analyzed.

3.2 Discovery

Paul Dirac developed what has become to be known as the Dirac Equation, combining quantum mechanics, electron spin, and special relativity in 1928 [102]. While the equation's validity was proven by an accurate, mathematical depiction of the fine spectrum of the hydrogen atom, it also suggested the presence of antimatter in that for the electron, there was both a positive and negative solution. Later, in 1928, Dirac published a second paper in defense of the negative-energy electron and postulated

that the proton might be the particle that his equation was suggesting existed [103]. Robert Oppenheimer did not agree with this assertion, and in 1931, Hermann Weyl published an article showing that the negative and positive energy electrons must have the same mass [104], one drastically lower than that of a proton. In response to this, Dirac published a third paper arguing that his equation must be accounting for some not-yet-discovered particle. Quickly following this in 1932, Carl Anderson discovered the positron while observing cosmic rays in a cloud chamber. In this chamber, particles make streaks along photographic plates that correspond to the mass-to-charge ratio of the particle. Under the effect of a magnet there was evidence of particles with the same mass of an electron, but bent in the opposite direction. While Anderson was the first to publish his findings, Frederic and Irene Joliot-Curie and Patrick Blackett and Guiseppe Occhialini had evidence of the positron in separate experiments, but did not publish the results. Carl Anderson won the Nobel Prize in Physics in 1936 for his discovery of the positron, a particle with the same mass and half-integer spin, but the opposite charge to that of the electron [105, 106].

3.3 Positron Sources

Positrons can be employed experimentally through either the use of bulk or beam-based techniques. The positrons are produced through a radioactive decay process for certain radioisotopes. There is a large number of positron emitting radioisotopes, but the most commonly used is ^{22}Na. This is a practical choice for experimental work due to its relatively long half-life of 2.6 years. The decay scheme for ^{22}Na is shown in Figure 3.1.

^{22}Na has a high positron yield of over 90% through its decay into an positron and an electron neutrino. The nucleus then enters into an excited state which is relaxed via the emission of a 1.275 MeV photon which occurs within 4 ps [107]. Positrons

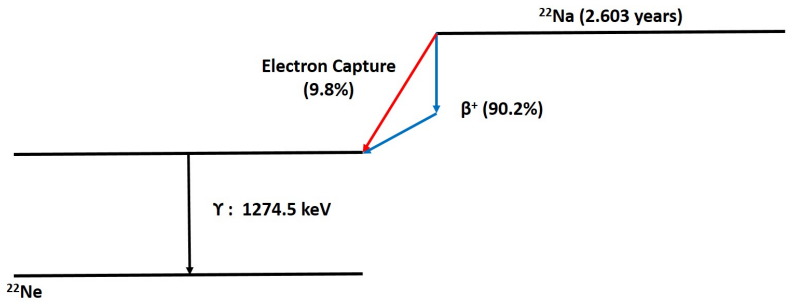

Figure 3.1. Nuclear decay scheme for ^{22}Na.

are emitted with a maximum energy (E_{max}) of 0.544 MeV, but an average energy of 0.260 MeV. In fact, the positrons are emitted with a distribution of energies ranging from thermal to the E_{max}.

For bulk positron measurements, a ^{22}Na source can be applied experimentally as a sealed source or by depositing an aqueous solution of ^{22}NaCl containing the radioisotope directly onto the samples. There are benefits to both options. Using sealed source allows the source to be reused and the material under test to remain uncontaminated; however depositing an aqueous solution directly on to the samples, removes any influence of annihilations that might occur in the sealing material from the collected spectra. The measurements that were conducted in support of this dissertation used a ^{22}Na source sealed in titanium foil. The implications of and corrections for this source choice are described in detail in Section 3.5.4.

3.4 Positron in Materials

Positrons interact with matter in a variety of ways that are decipherable through measurement techniques and can tell a unique story depending on the material under test. All experimental techniques require implantation of the positrons into the material with as little interference from the source itself or the environment between the source and the sample. As mentioned, positrons are emitted in a distribution of

energies and thus it is expected that the positrons will have an implantation profile based on their energies.

The implantation profile for positrons emitted from a radioactive source can be empirically described by the equation,

$$P(x) = e^{(-\alpha x)}, \tag{3.1}$$

where α is the linear absorption coefficient [cm^{-1}] and x is the depth [cm]. A number of empirical linear absorption coefficient expressions have been provided in the literature. Brandt and Paulin [108] developed the expression,

$$\alpha = 17\frac{\rho}{E_{max}^{1.49}}, \tag{3.2}$$

where ρ is the density of the material [g/cm^3] and E_{max} is the maximum energy of the positron [MeV]. Mourino et al [109], using experimental measurements involving materials with a wide range of atomic numbers determined the following expression,

$$\alpha = 26.8Z^{0.15}\rho, \tag{3.3}$$

where Z is the atomic number of the material under test. Dryzek and Singleton [110], through experimental and theoretical analysis, presented the following expression,

$$\alpha = 12.6\rho\frac{Z^{0.17}}{E_{max}^{1.28}}. \tag{3.4}$$

The implantation profiles for positrons in molybdenum using the linear absorption coefficients above are shown in Figure 3.2. There are differences in the calculated linear absorption coefficients determined from the three expressions. It should be noted that the uncertainty associated with the value calculated through the Drzyek and Singleton method is about 30% [110], which was much higher than many of the

other materials analyzed, and thus some variation in the profiles from various works should be expected.

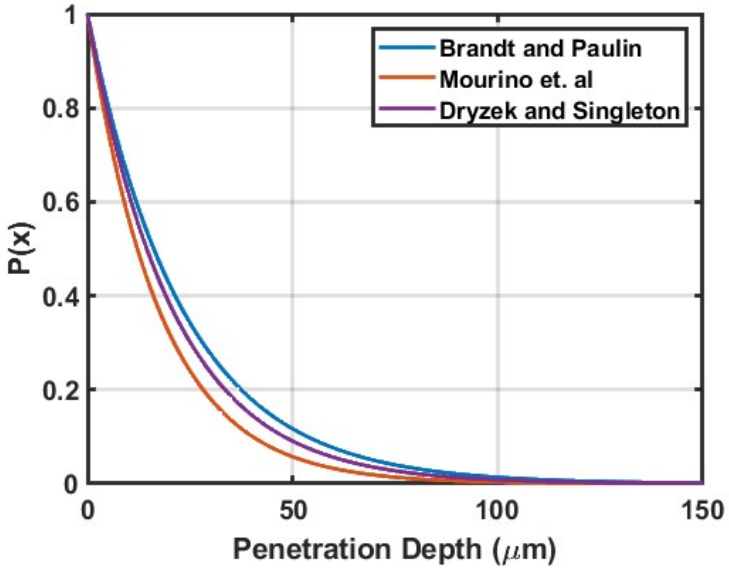

Figure 3.2. Probability functions for the implantation depths of positrons in molybdenum from a ^{22}Na source are plotted for the three linear absorption coefficients referenced from previous literature.

Even with the variation, it is clear that the vast majority of positrons emitted from ^{22}Na are expected to be stopped within about 100 μm of the molybdenum surface. This illustrates the fact that the positrons are sampling a three-dimensional space within the molybdenum, dependent on the energy of the positron and distribution of the radioactive material within the active area of the sealed source.

After implantation into the material, the positron will reach thermal energies very quickly (within a few ps) [107] relative to the lifetime of the positron within the material. This thermalization can occur by a number of different processes based on the energy of the positron. At high energies, the positron can ionize atomic nuclei or excite plasmons and at low energies, the positron will lose energy through interactions with phonons and by forming electron-hole pairs [107]. After thermalization the positron will diffuse through the crystal lattice in a random-walk manner. The

distance through which the positron diffuses is based on the material. In molybdenum, this diffusion length is somewhat less than 100 nm with the distance increasing depending with annealing time or temperature [111].

The diffusion of the positron through the crystal lattice allows for the positron to sample relatively large swaths of volume compared to other measurement techniques and contributes to the usefulness of PAS measurement techniques. As positrons impinge the surface of a material, some fraction are returned to the source due to backscattering and increases with atomic number [112]. For those positrons that implant and remain, the movement through the material is manifested predominately by Coulombic interactions. Positrons are positively charged and attracted to regions of low atomic density, or relatively high electronic density. Positrons will be predominantly attracted to regions of negative charge such as open-vacancy type defects. In materials with large regions of low electronic density, the positron may diffuse out of the material and be re-emitted. If a positron remains in the material and thermalizes, it will eventually annihilate with a rate that is dependent on the overlap of the positron and electron wavefunctions.

The annihilation of positrons and electrons results in the conversion of mass to energy according to Einstein's theory of relativity, via the equation,

$$E^2 = m_0^2 c^4 + p^2 c^2, \tag{3.5}$$

where m_0 is the rest mass of the particle, c is the speed of light, and p is the momentum of the particle. Positrons annihilate through either direct interaction with an electron or after forming positronium. Positronium is a quasi-stable, hydrogen-like, bound state between an electron and a positron. Annihilation occurs through two most probable mechanisms corresponding to the p-Ps and o-Ps. p-Ps forms when the spin states are parallel, whereas o-Ps forms when the spin state are anti-parallel.

During the annihilation process energy and momentum must be conserved. While a number of different mechanisms are possible as a result of this, the most common annihilation products are either two or three photons. The two photon mechanism refers to the annihilation of p-Ps which has a characteristic lifetime of 125 ps in a vacuum. The three photon mechanism refers to the annihilation of o-Ps which has a characteristic lifetime of 142 ns in a vacuum. The two-photon mechanism is the most common where the three photon occurs only at a ratio of 1:370 [113]. While higher order processes are also possible, the probability grows significantly smaller as the order increases. While the three-photon mechanism still occurs at an appreciable rate, the two-photon mechanism is of the most practical use in the experiments conducted during this research. The formation of positronium in condensed metals is rather unlikely due to the high electron density, however if there are low electron density areas such as large voids or open porosity available, these can be locations of positronium formation. Positronium annihilation is subject to pick-off events with nearby electrons or spin-conversion to p-Ps that significantly reduce the lifetime of the positron.

The two-photon annihilation mechanism results in the production to two nominally, co-linear 511 keV photons. Deviations in either the momenta or angle of the photons are measurable and used to decipher details about the microstructural environment in which the positron annihilated. The momentum of a thermalized positron is negligible compared to the electron [114], so deviations are considered to be solely due to the electron that was annihilated.

The annihilation rates within many solids are well understood both experimentally and theoretically through quantum mechanical calculations and modeling. The lifetime of a positron in a material and the positron's annihilation rate are inversely related. The annihilation rate will differ based on charge density, with defects and

regions of low electron density resulting in smaller annihilation rates and, thus, longer positron lifetimes.

The vacancies in a material will act as a trapping site for the thermalized positrons. If the Coulombic repulsion is lowered due to the a missing nuclei and associated electrons, than the defect can result in a potential well that traps the positron. Besides open-volume defects, negative charged impurities and dislocations can trap positrons causing a transition from the delocalized state to the localized state where the energy of the binding is transferred to the surrounding lattice. The binding energy associated with these types of defects is less than that for open vacancies and vacancy clusters, but is still significant at low temperatures where thermally activated detrapping is not possible [115].

The defect-specific trapping probability, μ_d, of a specific defect is a characteristic value dependent on the defect and the material. This is related to the positron trapping rate by the following equation,

$$\kappa_d = \mu_d C_d, \tag{3.6}$$

where κ_d is the positron trapping rate, and C_d is the defect concentration. If the material can be characterized by a single defect lifetime along with the defect-free state, then the annihilation rate of the defect site can be related to the positron trapping rate through the two-state trapping model. The two-state trapping model can be represented by the following equation,

$$\frac{1}{\tau_1} = \frac{1}{\tau_b} + (\mu_d C_d), \tag{3.7}$$

where τ_1 and τ_b are the lifetimes of the defect and defect-free (bulk) annihilation channels, respectively. Through the following equation,

$$\tau_b = \left(\frac{I_1}{\tau_1} + \frac{I_2}{\tau_2} \right)^{-1}, \tag{3.8}$$

where I_1 and I_2 are the intensities associated with the defect-free and defect lifetimes determined through PALS measurements. It is common to use a mean positron lifetime, $\bar{\tau}$,

$$\bar{\tau} = I_1\tau_1 + I_2\tau_2, \tag{3.9}$$

where τ_1 and τ_2 represent the two lifetimes determined through spectral deconvolution analysis. It should be noted that while the two-state trapping model suggests only two active annihilation channels, this is a simplification of the positron behavior in materials with multiple defects, such as those being investigated in this research. The experimental spectrum is not always readily deconvoluted into the multitude of lifetime components that are truly present in a spectrum if the lifetimes are too close together or if there are not enough counts to identify the lifetime. A mean lifetime reflects microstructural changes and can be used if the individual components are not easily identifiable through component analysis.

As mentioned earlier, the lifetime of a positron in a material is dependent on the charge density of the region in which it thermalizes. The charge density decreases as the void size increases and thus the annihilation rate drops and the lifetime of the positron increases. A model for the positron lifetime as a function of pore size was initially determined through the semi-empirical Tao-Eldrup model, but has been updated through a few different works [116]. The lifetime of positronium in defects and voids is reduced due to quenching of positronium through pick-off annihilations by electrons from the walls of the open volume defect. It has been shown that the pick-off rate is insensitive to the material [117] allowing the size of the pore to be

estimated from the lifetime of the positron. If the size of the void exceeds a certain diameter, around 100 nm, the possibility of positronium formation increases and the lifetime of positrons approach 142 ns or the lifetime of ortho-positronium in a vacuum. Positron lifetimes in metals are on the order of 100-500 ps and increase with the size of the free volume available in the defect. The atomic-level defect sensitivity of positron measurements allows for the study of vacancy behavior because of the direct change in the annihilation lifetime up to about 100 nm.

3.5 Practical Aspects of PALS

The lifetime of a positron is determined through the measurement of the time between the emission of the positron from the ^{22}Na, signaled by the subsequent 1274 keV photon, and the emission of the 511 keV annihilation photons. These measurements are generally carried out using fast scintillation detectors (e.g. barium fluoride (BaF_2)) which has a very fast decay component and a high atomic number providing improved efficiency and response over other options [118]. PALS measurements reported in this document were collected on the AFIT PALS Array developed by Gearhart as part of his doctoral research [119]. Six scintillation detectors were used as space was made to simultaneously collect data with a high-purity germanium detector. The scintillation detectors are coupled to fast photomultiplier tubes. The output is digitized and post-processing software determines the relevant start/stop events from the thirty detector pair couplings. Use of a system, such as the one in this work, that can perform digital pulse and timing analysis significantly improves the timing resolution over analytical systems [120].

3.5.1 Positron Lifetime Spectra

The lifetime of a positron in a material, or a specific defect in that material, is a characteristic property. Lifetimes can be determined experimentally or modeled theoretically through density functional theory (DFT). DFT calculations use quantum-mechanical electronic-structure calculations and have been utilized to calculate the positron lifetimes in bulk materials as well as vacancies in a large quantity of different materials. Lifetimes determined through DFT are generally lower than those determined experimentally [121].

A positron lifetime spectrum is a histogram of all the annihilation events measured from positrons that have been implanted in the material under test. Generally PALS spectra, at a minimum, include 10^6 counts in order to ensure proper deconvolution [107]. An example of a PALS spectrum collected on the AFIT PALS array is shown in Figure 3.3. Generally in order to perform spectral analysis, 3-5 x 10^6 counts in the spectrum are required for each lifetime [107]. Integrating over the entire spectra collected on the AFIT PALS array yields counts on the order of 10^7.

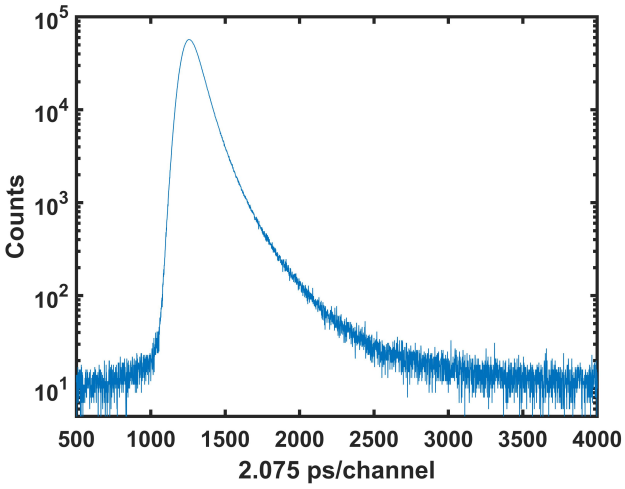

Figure 3.3. An example PALS histogram collected on the AFIT PALS array.

A PALS spectrum consists of a group of exponentially modified Gaussian func-

tions that are convoluted with the instrument resolution function of the detection equipment. Components of the Gaussian functions represent specific lifetimes and intensities for the various lifetime parameters associated with the material under test. Numerous non-linear, least squares fitting routines have been developed to aid in the deconvolution of PALS spectra; however the one used for this work is the PALS*fit*3 [122].

3.5.2 PALsfit3

PALS*fit*3 is a computer program that was developed by the group at the Technical University of Denmark. Only a brief introduction to the software will be presented here. An in-depth, mathematical treatment of the software package is presented in the PALS*fit*3 documentation prepared by the development team [122]. PAL*fit*3 includes two modules for fitting lifetime spectra, RESOLUTIONFIT and POSITRONFIT. RESOLUTIONFIT is used to determine the instrument resolution function which can then be imported into POSITRONFIT for use in fitting the lifetime components to the spectra. Both modules fit a model function to the lifetime spectrum that includes a function which models a convolution of the positron decay, instrument resolution function, and constant background using the least squares criterion in an iterative fitting technique. The software employs a modified Levenberg-Marquardt algorithm with a trust-region enhancement and a restricted minimization procedure. POSITRONFIT has been used for metallic systems to determine up to three lifetime components reliably [122]. A large number of input parameters can be altered prior to fitting using the two modules. Generally, the convergence produces the same lifetime components regardless of inputs; however, spectra with a large number of counts (10^7) can have local minima in the chi-square criterion used to determine the goodness of fit [122]. This results in erroneous lifetime parameters often warranting multiple fitting

procedures with varying input parameters to avoid this outcome. PALSfit3 outputs three statistical parameters, chi-square (χ^2), reduced chi-square ($V = \chi^2/f$, where f is the degrees of freedom), and the significance of imperfect model. When using RESOLUTIONFIT or POSITRONFIT to fit lifetime spectra, a good fit to the data should result in a reduced chi-square value as close to unity as possible.

3.5.3 Instrument Resolution Function

In order to properly analyze the lifetime components convolved in a PALS spectrum, it must be corrected for the spectrometer instrument resolution function. The RESOLUTIONFIT allows for fitting the parameters that determine the shape of the resolution function. Up to five width components and associated shifts can be selected as fitting parameters. The intensities of these components; however, must be fixed prior to running the module in order to limit the number of fitting parameters. The instrument resolution function for the AFIT PALS Array was determined using two single crystal copper samples. Two identical samples are required to sandwich the source and ensure no positrons are annihilating in the surrounding environment. The procedure used to determine the instrument resolution function followed the method outlined by Dr. Christopher Williams and Dr. Stephanie Johnson in a document co-authored by the AFIT Engineering Physics Department and the Air Force Research Laboratory (AFRL) Munitions Directorate [123].

The parameters describing the optimal instrument resolution function are shown in Table 3.1.

The components of the instrument resolution function were used to estimate the timing resolution of the array as about 204 ps (FWHM) which is roughly equivalent to other digital positron lifetime measurement systems [107]. The same single crystal copper spectrum used to determine the instrument resolution function was then an-

Table 3.1. Widths, intensities, and shifts associated with the optimal instrument resolution function for the AFIT PALS Array. The reduced-χ^2 parameter for this fit was 1.048.

	Component 1	Component 2	Component 3
WHM (ns)	0.20682	0.20633	0.16392
Intensities (%)	79	15	6
Shifts (ns)	0.0000	0.09010	0.00720

alyzed through the POSITRONFIT module to determine the source correction that accounts for annihilations due to the experimental set up.

3.5.4 Source Correction

Generally source contributions are determined experimentally by measuring the lifetime spectra of defect-free materials. The same single crystal copper spectrum used to determine the instrument resolution function was also used in this capacity. Experimentally, positrons in defect-free copper have a lifetime of 120 ps [121]. Deconvoluting the spectrum using the POSITRONFIT module yielded three lifetimes and intensities. The lifetime spectra revealing these components is shown in Figure 3.4 and tabulated in Table 3.2.

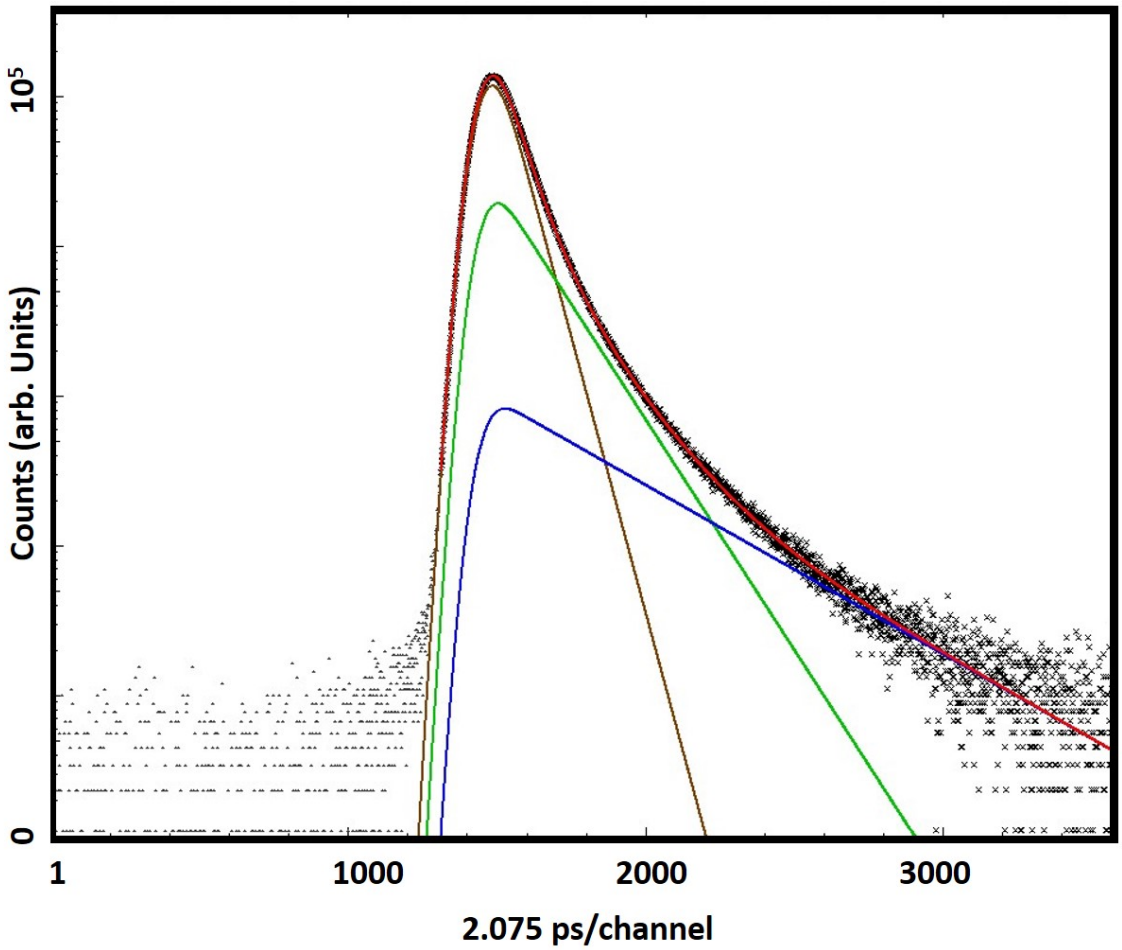

Figure 3.4. Positron lifetime spectrum of single crystal copper used to determine the correction for the titanium sealed ^{22}Na source. Brown (τ_1), green (τ_2), blue (τ_3), red (combined fits), black (collected counts).

Table 3.2. Lifetime and intensity parameters that provide the best fit to the single crystal copper lifetime spectrum. The reduced-χ^2 parameter for this fit was 1.048.

τ_1 (ps)	I_1 (%)	τ_2 (ps)	I_2 (%)	τ_3 (ps)	I_3 (%)
121.0 ±1.2	77.14 ±0.77	282.8 ±5.3	20.76 ±0.65	745.1 ±18.8	2.09 ±.15

The first lifetime component represents the copper while the second and third lifetime components were attributed to the source's contribution. The expected experimental lifetimes of annealed and defected titanium are between 150 and 190 ps depending on the defected state of the metal [124]. The increase in lifetime component to 282.8 ps is due to the convolution of the annihilation signals from the foil and

NaCl crystallites which have a lifetime around 430 ps. The 745.1 ps lifetime can be attributed to interactions with the surfaces of the source [125].

Historically, only a small number of reports have been published focusing on the effect of source contributions to positron lifetime measurements and the majority of these only assess Kapton as the foil material [125, 126, 127, 128]. Staab et al. [129] addressed source corrections in aluminum encapsulated sources while McGuire and Keeble [125] included nickel foil as an additional material to both Kapton and aluminum. In these studies an 10 μCi source was deposited on aluminum, Kapton, and nickel source foils with thicknesses of 2 μm, 7 μm, and 5 μm. The intensities of the foil components were determined to be about 5%, 16%, and 38% respectively for molybdenum samples. The intensity of the source contributions are a function of the atomic number of the material under test and the thickness and electron density of the encapsulating material. The ^{22}Na source used during this research is sealed by a 5.1 μm thick titanium foil. As titanium has a lower atomic number than nickel, at the same thickness, it is expected that the intensity of the source contribution would be less. Based on the previously reported source contribution numbers, the roughly 21% contribution from the titanium foil used in our experiment is consistent with literature.

3.5.5 Fitting Procedure

The instrument resolution function and source correction discussed in the previous section convolved with the signals produced from annihilations in the sample under test and provided the data included in the overall PALS spectrum for each sample. The POSITRONFIT module accepts the resolution function as in importable data file and the source correction can be subtracted during the fitting process. Prior to deconvoluting the spectrum, input parameters such as fit ranges and background

must be defined. The spectrum produced through the AFIT PALS Array contain over seven thousand channels, most of which can be considered background. The established fitting procedure was to set the minimum and maximum fit channels to points that allowed for measurement of the specific region containing the lifetime information of annihilations in the samples only, after subtraction of background and source contributions. Background limits were set to the first 800 channels in the spectra, a location that contains only background signal. The fitting procedure focused on parameters that could be applied across all of the LPBF lifetime spectra and result in consistently acceptable goodness-of-fit parameters. This was an iterative process that resulted in the minimization of the reduced-χ^2 parameter for all fits. As mentioned earlier, the spectra collected on the AFIT PALS Array produce fit regions with greater than 10^7 counts. Due to the possibility of generating erroneous fitting parameters, an in-depth iterative process was used to initially determine the influence of changes on the many input parameters such as fit ranges, time-zero and lifetime guesses, and background subtraction techniques. For specific spectra, the fit parameters could be altered to reduce the χ^2 further, however these differences were not consistent across the collected spectra, and applying a standardized procedure was considered prudent.

3.6 Practical Aspects of DBAR

DBAR samples the electronic environment of a material by measuring the momentum distribution of the annihilation photons. The characteristics of positron annihilation are sensitive to the electronic environment. Variation from the expected 511 keV photon energy occurs due to conservation of momentum requirements during annihilation. DBAR measurements take advantage of this variation by measuring the energy associated with positron annihilation. A Doppler shift occurs that corre-

sponds to the momentum of the electron involved in the annihilation event. As the momentum of the positron is assumed to be negligible, all of the Doppler-broadening information is attributed to the electronic structure of the material. The broadening of the annihilation line can be determine via the following equation [107],

$$E_\gamma \simeq mc^2 \pm \sqrt{\frac{1}{2}mc^2E}, \tag{3.10}$$

where mc^2 is the rest mass of an electron, E_γ is the energy of the Doppler-broadened γ, and E is the energy of the annihilating pair. The difference between E_γ and mc^2, ΔE, is the observed broadening in the annihilation line. If the electron is assumed to have a momentum, p, corresponding to an energy, E, of 5 eV, then per Equation 3.10 the observed broadening is roughly 1.13 keV. Obtaining a Doppler-broadening spectrum requires measuring the annihilation events with a detector with sufficient resolution (e.g. high purity germanium (HPGe) detector) and convert pulse height to energy. Typically, collecting 10^6 counts in the 511 keV peak is considered for proper counting statistics.

3.6.1 Experimental Setup

HPGe detectors are often chosen for DBAR measurements due to their sensitivity to incoming radiation and a detector response that is proportional to energy. DBAR measurements naturally require a detector with high energy resolution, often on the order of 1.1 keV at the 511 annihilation peak [130]. The detection setup used in this research includes an cryo-cooled Ortec HPGe detector coupled to a Canberra Digita Spectrum Analyzer (DSA) 1000 multichannel analyzer (MCA). The data was collected using the Ortec GammaVision Gamma Acquisition and Analysis software package and processed in MATLAB. Manufacturer specifications state the detector resolution at the 1333 keV of the cobalt-60 radioisotope is 2.1 keV. Figure 3.5 shows

a cobalt-60 spectrum collected using this experimental setup.

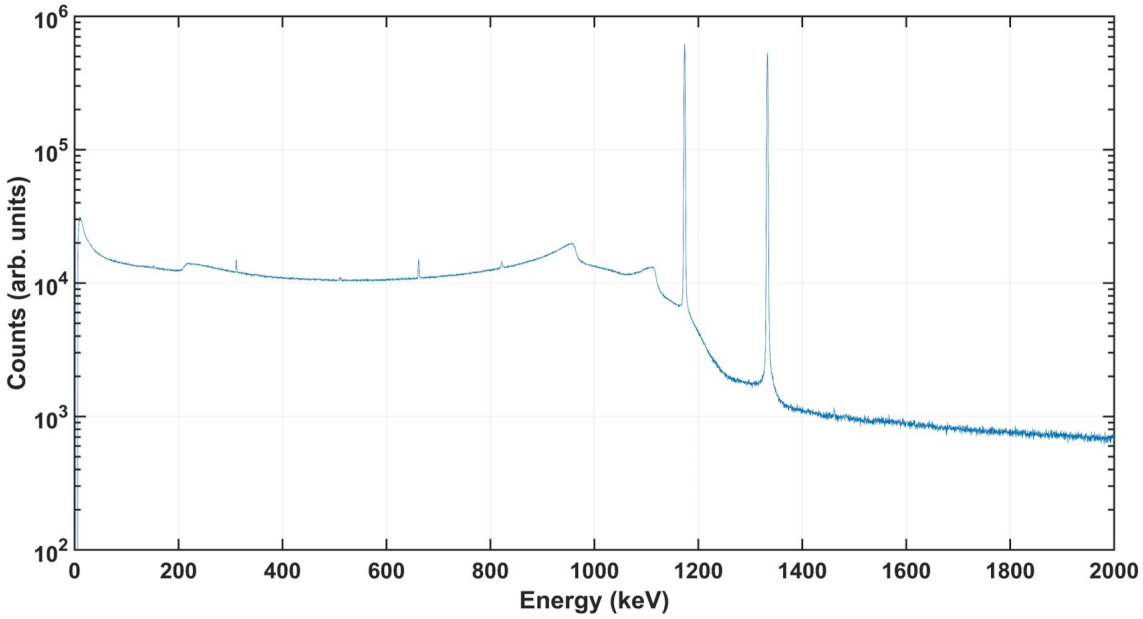

Figure 3.5. Calibrated cobalt-60 spectrum.

Calibration of the detector was performed using the photopeaks in Table 3.3. The energy calibration was determined through a linear fit of the photopeaks and yielded the following equation,

$$Energy(keV) = 0.2596 * Channel + 1.1901, \tag{3.11}$$

with an R^2 value of unity. The resolution was calculated as 2.08 keV by fitting a Gaussian function to the 1333 keV photopeak.

Table 3.3. Peak positions used to determine calibration and resolution of the HPGe detector.

Channel	Energy (keV)	Photopeak
1194	311	1333 keV double escape peak
2545	662	1173 keV single escape peak
3161	822	1333 keV single escape peak
4516	1173	gamma photon
5130	1333	gamma photon

Background radiation was measured three times during the experimental period, twice near the beginning (February and March, 2022), and once more near the end (January, 2023). The background spectra are shown in Figure 3.6.

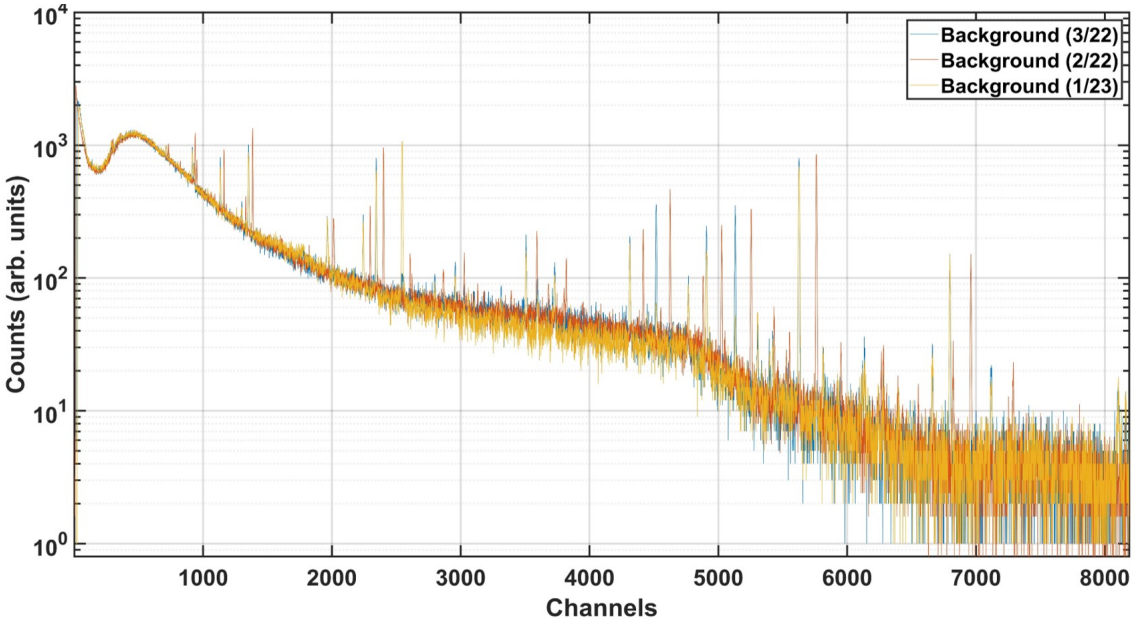

Figure 3.6. Spectra from three background collection measurements.

The sources contributing to background radiation in the area clearly changed significantly over the period in which these measurements were taken. Additionally, the amount of background radiation was variable and it can be seen that the detection equipment experienced a level of gain shift as the location of the background peaks were not consistent. Fortunately the background in the region of interest, roughly 511 to 526 keV is much smaller than the collected spectra. Background counts are on the order of the counting error. Due to the inability to accurately remove background from the collected spectra, and the magnitude of the counts present in the annihilation peak, the background was considered negligible for the analysis of the DBAR spectra.

The DBAR measurements were taken over a year long period and during this time, as evidenced by the background measurements, a measure of detector resolution variability occurred during this time. While this required individual calibration of

each spectra, with a linear calibration and a resolution within the manufacturer limits confirms that this detector is suitable for DBAR measurements.

3.6.2 Post-Processing and Error Analysis

Analyzing a Doppler-broadened spectrum usually consists of determining the lineshape parameters that partition the spectrum into regions of low momentum and high momentum. Figure 3.7 demonstrates, generically, the definitions of the two lineshape parameters.

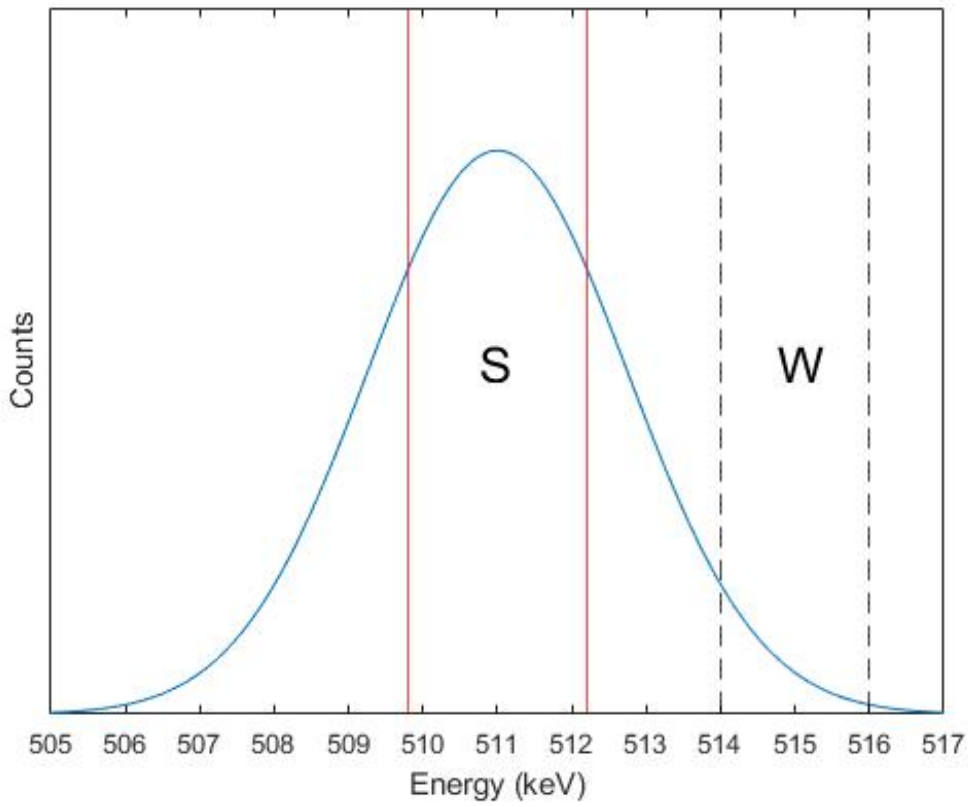

Figure 3.7. Partitioning of the Doppler-broadened spectrum for lineshape parameter analysis.

The S (shape) parameter accounts for the low momentum events that are associated with annihilations of valence electrons. It is defined as the ratio of the central region (0.8 keV around the 511 keV peak) to the counts in the total region (505 to 517

keV). The W (wing) parameter accounts for the high momentum events associated with annihilation events with core electrons. The W parameter is defined as the ratio of the wing region (514 to 516 keV) to the total region [107]. As additional shells are added to the nucleus of an atom (traveling down rows of the periodic table) the number of core electrons increases. As would be expected, the ratio of annihilation events with core electrons increases resulting in a larger W parameter. Generally the W parameter is only measured on the high energy side of the peak as there are no contributing three-photon annihilations from *o*-Ps [107]. The S parameter can be used to study defect concentrations. Vacancy-type defects generally have a lower concentration of core electrons and result in a larger S parameter. A common investigation using the S parameter involves studying the change in the S parameter with annealing time or temperature. As annealing a metal results in the removal of vacancy-type defects, the S parameter decreases as these defects disappear. In order to appropriately determine the S and W parameters for a Doppler-broadened spectrum, calibration, background correction, normalization, and error propagation of the data is required.

Due to slight differences in the detector response for each data set collected, individual energy calibrations were performed for each data set. The DSA 1000 MCA produces a histogram with 8190 channels; however, through initial measurements it was evident that the calibration of the DBAR spectra were not able to be accomplished without performing a sub-bin analysis. The calibration as performed by interpolating the original number of channels in the 511 and 1274 keV peaks to increase the bins by three orders of magnitude. This allowed for sub-bin identification of the centroid and a calibration with increased fidelity. MATLAB and the associated curve fitting tool were used to perform these functions. To calculate the linear calibration equation, the regions containing the peaks were separated and fit with an

appropriate number of Gaussian functions in the curve fitting tool and the parameter describing the centroid was identified.

Once calibrated, the spectra were peak-area normalized to the sum of the counts in the 505 - 517 keV region. The error associated with the counts produced in the spectra prior to normalization are given by,

$$\sigma_n = \sqrt{n}, \tag{3.12}$$

where n is the number of counts in each bin. This produces an error at each bin in the spectrum. In order to determine the error associated with the normalization, the absolute error is propagated by,

$$\sigma_R = R\sqrt{\left(\frac{\sigma_{N_1}}{N_1}\right)^2 + \left(\frac{\sigma_{N_2}}{N_2}\right)^2}, \tag{3.13}$$

where R is the value of the normalization, N_1 is the number of counts in each bin, and N_2 is number of counts in 505 - 517 keV region [118]. The error associated with this normalization is generally very small compared to the differences in the broadening of the annihilation peak in the wing region of 514 - 516 keV.

3.6.3 Analysis of Metal Standards

In this analysis, four, traditionally manufactured metal standards were compared: aluminum, titanium, copper, and molybdenum. Aluminum is located in period 3, titanium and copper are located in period 4, and molybdenum is located in period 5 of the periodic table. The electron configurations of the metals in Figure 3.8 are shown in Table 3.4.

In the series of metals shown in Figure 3.8, the broadening of the annihilation line trends with increasing atomic number which is expected due to the filling of

Table 3.4. Properties of selected pure metals.

Element	Atomic Number	Electron Configuration
Al	13	$[\mathrm{Ne}]3s^2 3p^1$
Ti	22	$[\mathrm{Ar}]3d^2 4s^2$
Cu	29	$[\mathrm{Ar}]4s^1 3d^{10}$
Mo	42	$[\mathrm{Kr}]4d^5 5s^1$

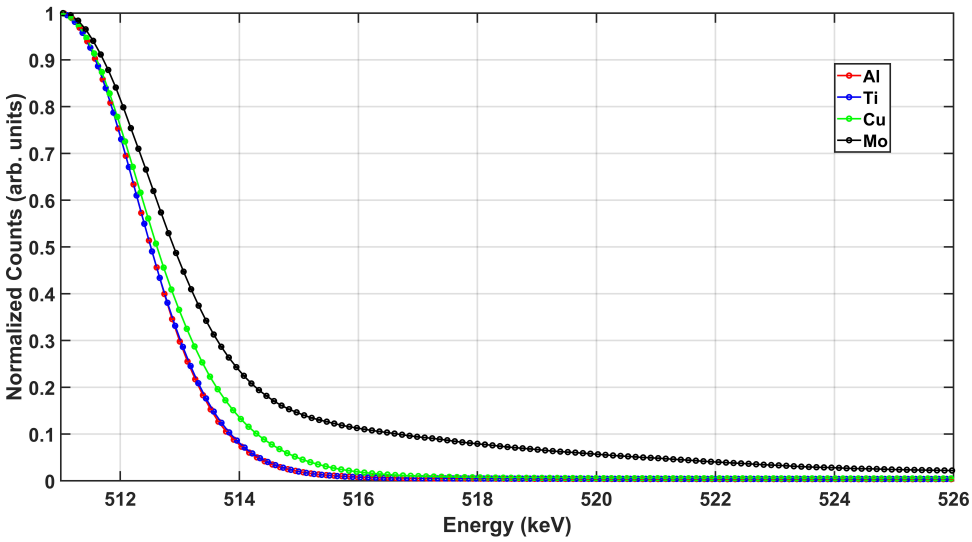

Figure 3.8. Momentum broadening spectrum of a series of metals: including aluminum, copper, titanium, and molybdenum.

higher level electron shells. The broadening of annihilation curves take the expected shapes with the central and wing regions reduced and enhanced, respectively, as the atomic number of the metal increases. While copper and titanium are in the same period, copper's additional electrons fill the $3d$ shell while leaving an incomplete $4s$ shell. Titanium shows little broadening over that of aluminum. The broadening in molybdenum is large compared to the other metals, but this is to be expected given the differences in atomic number.

As part of the PALS analysis that was discussed in Section 5.1, multiple single crystal copper pieces were available for DBAR spectra collection. Two measurements were conducted in March, 2022, that involved four distinct pieces. Three additional measurements were conducted in December, 2022, which involved only two pieces.

In December, the measurements were conducted without changing the experimental setup, only resetting the 8 hour counting time. It should be noted that these single crystal copper pieces were nominally identical. Figure 3.9 shows the variability in the broadening curves. The width of the line represents the propagated statistical error obtained through Equation 3.13.

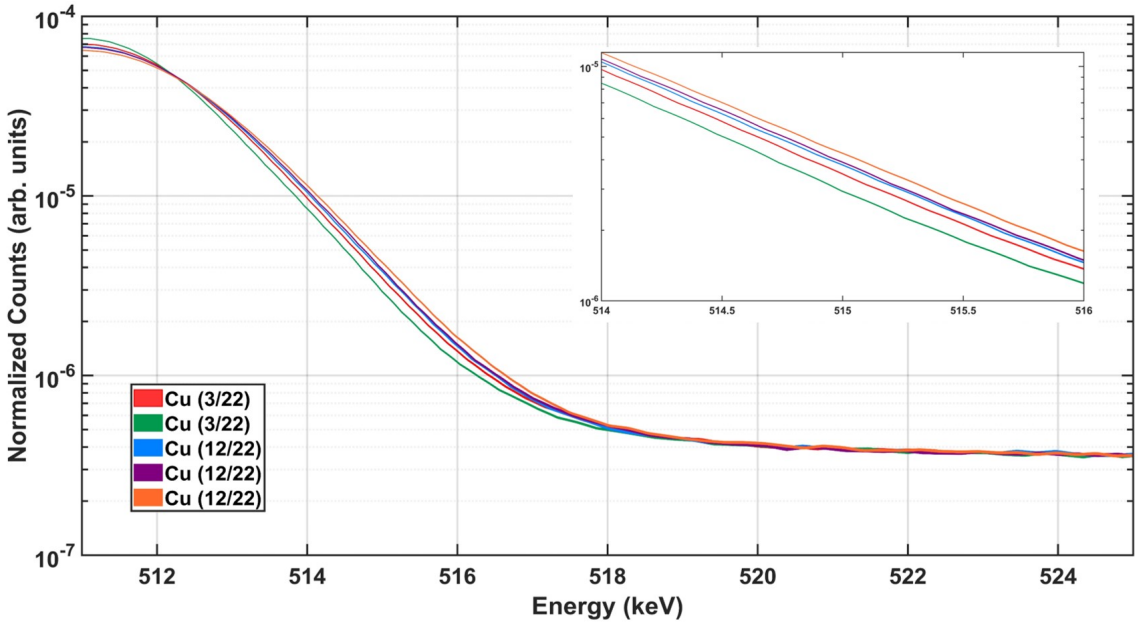

Figure 3.9. Momentum broadening spectrum of five copper data collection periods.

There is no material-specific reason why the five measurements of the copper samples should yield different amounts of broadening of the 511 keV photopeak, however as the broadening of the curve is, in part, a function of the detector resolution it is clear that the resolution drift is effecting the DBAR data collection. The variability in the detector resolution directly impacts the determination of the lineshape parameters as they are a function of the 511 keV photopeak broadening. As the detector resolution increases, the S-parameter decreases. This relationship is shown in Figure 3.10.

It is clear that that there is a level of systematic variation not confined to the statistical error in the data collected. The cause for this variation is the detector

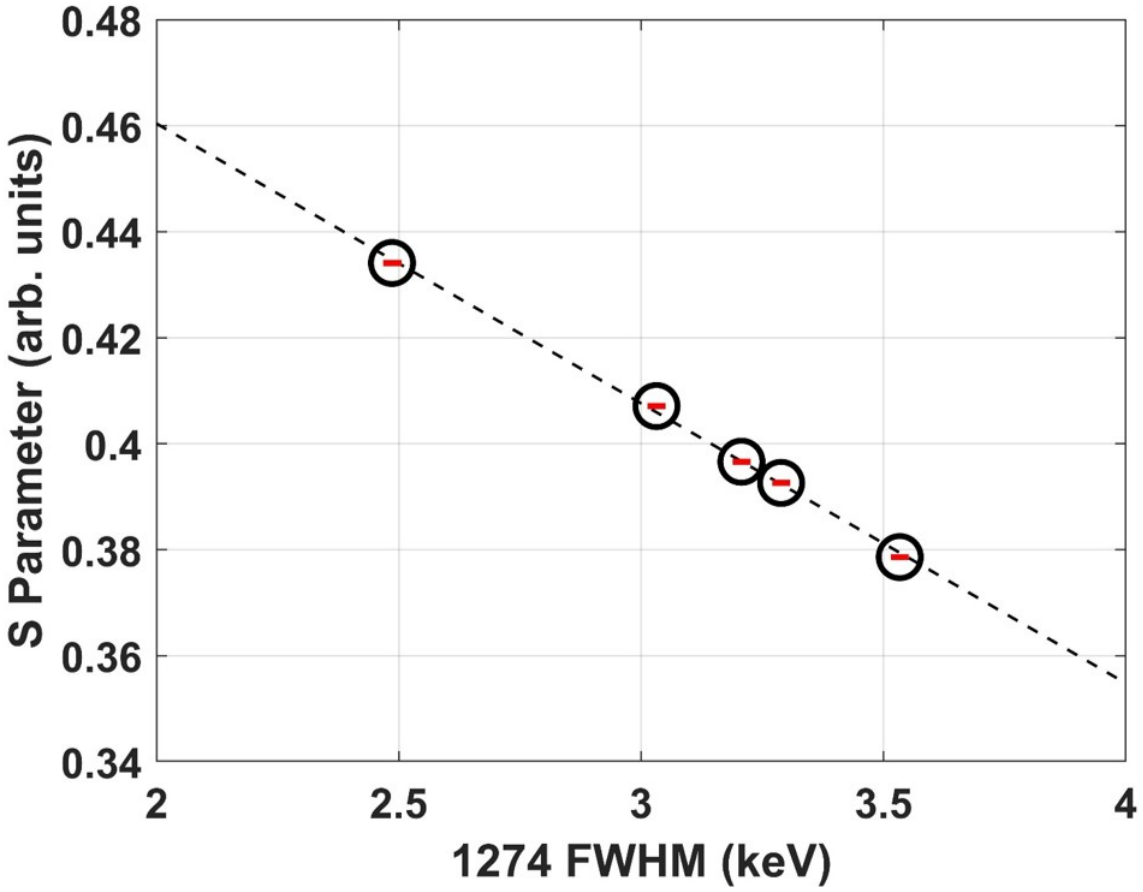

Figure 3.10. The S parameter determined from the five copper measurements as a function of 1274 keV FWHM.

resolution drift and should be considered representative of the DBAR data collected on all samples. Further work will need to be completed on the relationship between the FWHM and S parameters in order to correct for the detector resolution drift.

3.7 Current State of PALS Regarding AM and Molybdenum

The following section provides a literature review on the PALS studies of molybdenum and AM metals. Molybdenum has often been studied through the use of positron techniques, most commonly after irradiation in an effort to understand the defect structure during recovery processes, but more recently after plastic deformation and annealing. AM metals have garnered much less attention in terms of PAS

analysis despite the remarkable amount of research into the microstructure and defect behavior of AM metals.

Even though the usefulness of positrons to study metals was first documented in the early 1960s, it wasn't until ten years later that molybdenum was used as a subject material. Irradiated molybdenum has been studied by positron techniques since the early 1970s due to concerns with radiation damage suffered during use in nuclear power reactors. The first recorded positron study of molybdenum was published by Mogensen et al. [131] and involved analyzing the angular correlation of irradiated molybdenum. This early study showed that voids in molybdenum could be assessed using positron techniques, but was unable to provide unambiguous data interpretation. At the same time Cotterill et al. [132] studied neutron-irradiated molybdenum with voids in the range of 30-40 $\mathring{A}$ in diameter. Measurements of the irradiated molybdenum produced lifetimes that were 400-500 ps longer than what was measured in annealed molybdenum. The authors found the large discrepancy in lifetimes of the irradiated and annealed molybdenum surprisingly as such a drastic increase hadn't been observed in metals and questioned the theoretical understanding that positronium could not form in condensed metals. Comparison to angular correlation data showed that positronium was not forming and that the long lifetimes were a result of the large voids caused by irradiation. Interestingly the angular correlation was narrower for the small voids than the large voids, which was opposite the expected result. The authors noted that this was an indication that while the same positron annihilations were measured, angular correlation measures the center-of-mass momentum and lifetime spectroscopy measures the electron density. This understanding can also be applied to angular correlations counterpart in DBAR when considering the results of Doppler-broadening and comparing those to the positron lifetimes.

Cheng et al. [133] determined the lineshape parameters for neutron-irradiated

molybdenum in 1975. It was found that the S parameter increased with the amount of neutron fluence and was likely due to an increase in void concentration or void diameter. The same group measured the positron lifetime of the irradiated molybdenum in 1976 [134]. While at the time, transmission electron microscopy could not identify the voids in some of the samples, the positron lifetimes indicated that they were present. A 450 ps lifetime was assigned as a characteristic value for the voids formed in molybdenum between 350-500°C. Additional measurements showed lifetimes up to 600 ps at annealing temperatures of 600-1000°C. These results and other at the time were leading to the realization that the positron lifetimes can be correlated to the void size in molybdenum.

Grynszpan et al. followed this research with more positron analysis if neutron-irradiated molybdenum [135]. In this work irradiated molybdenum was isochronally annealed at various temperatures. At temperatures above 900°C, which is the recrystallization temperature of molybdenum, the intensity of the defect lifetime component decreased rapidly. It should be noted that the lifetime consistent with the presence of large voids (∼465 ps) was present throughout, but the intensity associated with it dropped from over 70% below the recrystallization temperature to below 10% when above. Another finding from this work was the presence of annihilations of positrons trapped at dislocation loops. Positrons annihilating in dislocation traps result in a lifetime that is roughly 60% greater than the annealed defect-free lifetime.

The application of positron studies to molybdenum plastically deformed as opposed to irradiated was shown by Petersen et al. [136]. In this work, pure molybdenum was plastically deformed through cold rolling to various degrees of thickness reduction. The S parameter increased with reduction thickness and decreased with annealing temperature. The lifetime of the defect component increases with annealing temperature as small voids aggregate to form larger vacancy defects. As the

temperature increases to the recrystallization temperature, thermal evaporation of smaller voids contributes to continued growth of large voids. Above the recrystallization temperature, dislocation recovery begins at the lifetime decreases. The intensity of the defect component decreases consistently with increasing temperature as the concentration of defect traps drops.

Hyodo et al. [137] studied single crystal molybdenum that was irradiated by neutrons at 100°C and identified characteristic lifetimes for a number of microstructural features. The lifetime found in the bulk, defect-free metal was 115 ps while vacancies, dislocations and large voids were found to be 190, 160, and 480 ps, respectively. These lifetimes are in agreement with previous measurements by other research groups. It was only possible to fit the data to two components, and after an extensive parameter search in an effort to identify an expected longer lifetime component for larger clusters of voids. The parameter search included choosing a fixed lifetime that ranged between 180 ps to 420 ps, consistent with various void sizes. Constraining the third component while leaving the first two components unconstrained allowed for a least square search using the reduced χ^2 parameter as a criterion. The presence of a third lifetime component significantly worsened the goodness-of-fit criterion and it was concluded that there were relatively few of these larger vacancy clusters contributing to the annihilation signal. The positron analysis conducted in this research used a similar approach of constraining known lifetimes and using the reduced χ^2 parameter to determine the presence of certain microstructural features.

A four state positron trapping model for neutron irradiated molybdenum was proposed by Pagh et al. [138] to study the temperature dependence of the lifetime parameters. Positrons can become detrapped from shallow traps if the thermal energy supplied overcomes the binding energy of the trap. The study found that the dominant trapping sites were voids and vacancy loops, with a similar lifetime for voids

of around 460 ps. A constrained analysis followed, setting the defect-free lifetime at 120 ps. A lifetime of 156 ps was found to correspond to dislocation jogs which are formed by the intersection of dislocations. The proposed model takes into account the detrapping of positrons in vacancy loops in favor of more strongly bound traps such as point-like defects.

Zhiyong et al. [139] conducted a positron study of proton-irradiated molybdenum and confirmed the characteristic lifetimes of positrons in molybdenum. An early version of the POSITRONFIT module was used to fit the collected lifetime spectra. Analysis was conducted for two and three lifetime components. The three lifetime analysis required constraining the second lifetime component at 174 ps and yielded a lifetime component that was longer than the characteristic monovacancy lifetime. This was understood to represent a convolution of vacancies and small voids. It was noted that vacancies migrate and agglomerate at lower temperatures thus increasing the lifetime. This formation of a longer lifetime can disrupt the fitting procedure where some of the contribution of the vacancies and dislocations is transferred to the first lifetime component representing the defect-free material and the intensity assigned to the defected component is artificially reduced. As the lifetimes of positrons in specific defects in molybdenum are characteristic and known from past research, it is possible to constrained additional lifetimes and reduce the effect of signal convolution in the analysis. These authors noted that by constraining the third lifetime, the reduction of the defected intensity was removed.

Most recently, positron studies into molybdenum by Dryzek et al. [140, 141], have investigated defect behavior during annealing after mechanical processes introduced plastic deformation. Lifetime analysis was correlated with both x-ray diffraction and electron backscatter diffraction methods. Two term lifetime analyses were used determine the positron diffusion length, which in turn was used to calculate the

activation energy associated with grain boundary movement. These results were compared to X-ray diffraction to study the recrystallization process at temperatures between 800° and 1050°.

In general, the studies described above were conducted to gain understanding in the defect behavior of molybdenum during annealing stages. The heat treatments involved in the standard annealing of molybdenum occur over relatively long periods when compared to the thermal cycling seen in LPBF, but the identification of the characteristic lifetimes of molybdenum allows for the examination of the defect structure in LPBF molybdenum. While there is a rather large amount of literature reporting the positron study of molybdenum, the same cannot be true with AM metals. As of the writing of this dissertation, no other work has been published on the positron study of AM molybdenum and only a handful of other AM metals have been reported on.

IV. Microstructural Characterization

This chapter outlines the techniques used to characterize the influence of laser scan speed and the addition of 0.1 wt% silicon carbide to molybdenum on the chemical composition, microstructure (average grain size, misorientation angle, texture, etc.), and mechanical properties. The contents of this chapter, in part, have been published as a original research article in the Multidisciplinary Digital Publishing Institute (MDPI) journal *Crystals*, which is an open-access journal with a 2021 Impact Factor of 2.670 per *Journal Citation Reports* by Clarivate [142]. *Crystals* focuses around all aspects of crystalline materials, including the characterization of mechanical, chemical, electronic, magnetic, and optical properties. The article was published on September 8, 2022, and has the following DOI.

DOI: 10.3390/cryst12091276 [143]

Further data and analyses have been added to the contents presented in the journal article as extensive EBSD analysis was conducted on the pure molybdenum samples after the article was originally published. The analysis presented in this chapter directly focuses on the research objectives under Problem Statement 1 presented in Chapter 1, and indirectly supports Problem Statements 2 and 3. The objectives of Problem Statement 1 are addressed by consolidating pure molybdenum and a homogeneous mixture of molybdenum and silicon carbide (0.1 wt%) at four different scan speeds (100, 200, 400, and 800 mm/s). The printing characteristics, chemical composition, microstructure, and mechanical properties were compared across the four scan speeds. The addition of silicon carbide improved the optically determined density and flexural strength at 400 mm/s by 92% and 80%, respectively. The oxygen content was reduced by an average of 52% over the four scan speeds. Two mechanisms of oxygen reduction were identified as responsible for the improvements: oxidation of free carbon and the creation of secondary phase nanoparticles.

Without the extensive characterization outlined in this chapter, the objectives of Problem Statements 2 and 3 would not be possible. Microstructural characteristics such as grain size, crystallographic orientation, the fraction of high-angle grain boundaries, and the presence of secondary phases can all influence the positron characteristics of a material and a knowledge of this information greatly aids in deciphering the meaning behind the PAS data presented in Chapter 5.

4.1 Materials and Methods

The pure molybdenum and Mo-0.1SiC specimens used during the course of research for this dissertation were produced using a GE Concept Laser Mlab Cusing 200R 3D metal printer (Boston, MA, USA), shown in Figure 4.1, equipped with a 200 W continuous wave Yb:YAG fiber laser.

Figure 4.1. Image of the Concept Laser 3D metal printer used during this research.

The Additive Manufacturing Laboratory (AML) run by AFIT/ENY has the capability of introducing argon, nitrogen, and hydrogen as shield gases in the build chamber. The specimens built for this research were printed under a pure nitrogen shield gas. Oxygen levels were maintained throughout the printing process at the lowest observable level (<1000 ppm) as monitored through system controls.

The feedstock powders consisted of raw spherical molybdenum powder (99.9% Mo) with an average particle size of approximately 30 μm, provided by Tekna (Sherbrooke, QC, Canada) and silicon carbide with average particle sizes on the order of hundreds of nm, provided by AFRL (Wright-Patterson Air Force Base, OH, USA). The molybdenum powder was sieved at 45 μm while the silicon carbide powder was nonspherical, nonuniform, and of sub-micron size. SEM images of the pure molybdenum, silicon carbide, and mixed powders are shown in Figures 4.2, 4.3, and 4.4, respectively. In Figure 4.4, backscatter electron imaging highlights the presence of the silicon carbide nanoparticles coating the surfaces of the molybdenum powder.

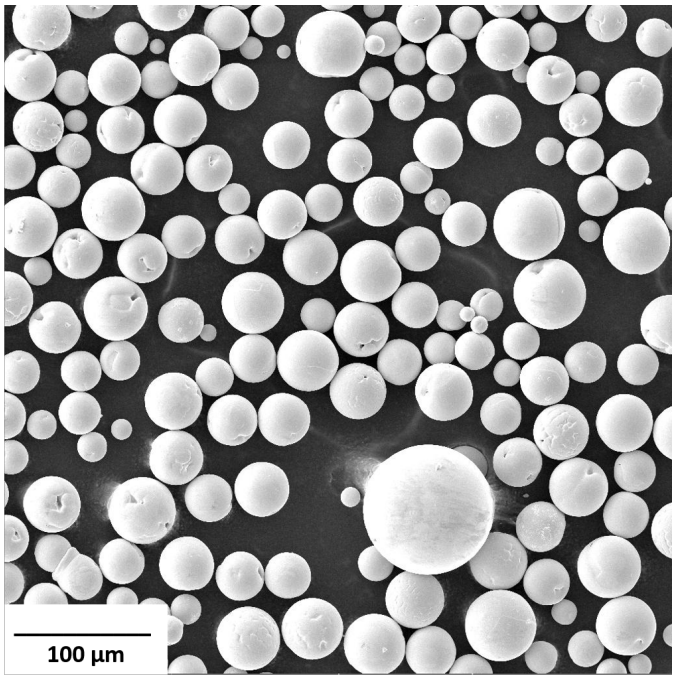

Figure 4.2. SEM image of spherical pure molybdenum powder.

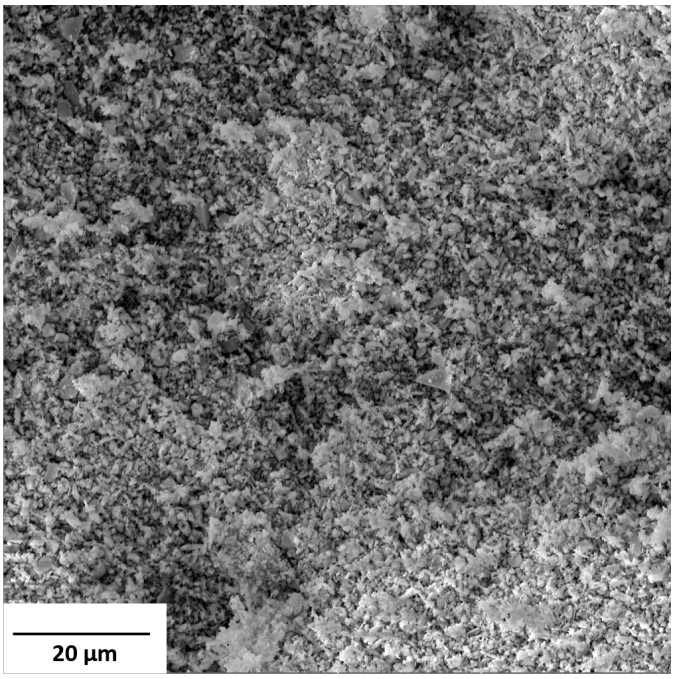

Figure 4.3. SEM image of nonuniform silicon carbide powder.

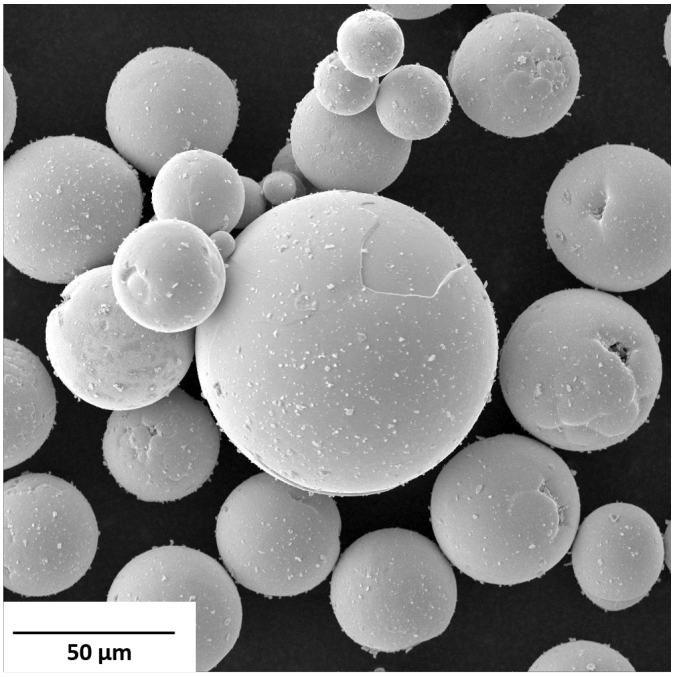

Figure 4.4. SEM image of mixed Mo-0.1SiC powder.

The powders were mixed using a DAC 250.1 FVZ-K SpeedMixer (FlackTek inc, Landrum SC, USA), shown in Figure 4.5. The mixer can handle 200 g of powder at

Figure 4.5. The FlackTek Inc. Speedmixer used during this research.

a time, so for the Mo-0.1SiC composition, 0.2 g of silicon carbide powder was added to a balance of molybdenum powder for each mix. Enough powder was mixed to ensure the powder chamber was at least 10 mm deep to account for the height of the built specimens. The batches were mixed for a pair of one-minute periods with one minute of cooling between. As soon as the powders were mixed, an SEM tab with carbon tape was used to take a sample of the mixed powders. The powders were immediately imaged in the SEM to ensure uniform mixing. Homogeneous mixing of the powders was confirmed with images such as the one displayed in Figure 4.4 where the silicon carbide particles are shown well distributed and adhered to the surface of the molybdenum particles.

Cuboid specimens with dimensions 12 mm x 4 mm x 2 mm were consolidated on a copper substrate using a fixed laser power of 200 W, hatch spacing of 50 μm, and a layer thickness of 20 μm at four different scan speeds: 100, 200, 400, and 800 mm/s. A meander laser scan strategy with a 90° rotation between layers was used. The

line energy densities (LED) and volumetric energy densities (VED) for the process parameters described above are shown in Table 4.1.

Table 4.1. Scan speeds with associated line and volumetric energy densities used to print pure molybdenum and Mo-0.1SiC.

Scan Speed (mm/s)	LED (J/mm)	VED (J/mm^3)
100	2.00	2000
200	1.00	1000
400	0.50	500
800	0.25	250

The cuboid specimens were used to perform bend strength measurements. Once broken, these bars were mechanically ground to 800 grit, polished to a 1 μm diamond suspension and etched using a 30% hydrogen peroxide and colloidal silica suspension (1:5) for EBSD analysis.

Using an established procedure described in Eckley et al. [4] and Kemnitz et al. [68], all specimens were printed on the copper substrate with a 0.5 mm offset at the scan speed of 800 mm/s. This offset was removed when the specimens were separated from the substrate using wire-cut electrical discharge machining (EDM).

The chemical composition of the powders and consolidated specimens were analyzed by Luvak Inc. (Boylston, MA, USA) following procedures outlined in ASTM 1019-18 [53]. The carbon content in the consolidated specimens was determined through infrared (IR) absorption where the total carbon content is measured through the IR absorption properties of carbon monoxide and carbon dioxide after the specimen undergoes combustion in a stream of oxygen. The nitrogen content in the pure and mixed powders and the consolidated specimens was determined through the inert gas fusion and thermal conductivity detection test method. Specimens were introduced to a helium environment at a temperature no less than 1900°C. The nitrogen present in the specimens is released as diatomic nitrogen and separated from other gases present. The thermal conductivity properties of nitrogen are used to quanti-

tatively measure the nitrogen content. The oxygen content in the pure and mixed powders, and the consolidated specimens, was determined through the inert gas fusion and IR absorption test method. Oxygen is fused under inert gas and combines with carbon to produce carbon monoxide and carbon dioxide of which the IR properties are used to quantitatively measure the oxygen content. The rounding of test results provided by Luvak Inc. were conducted in accordance with ASTM Practice E29 [144]. Carbon content wasn't measured in the powder samples as the Mo-0.1SiC mixture has a nominal content of 300 ppm.

The reflectance of the powders were measured by AZ Technology Inc. (Huntsville, AL, USA) following procedures outlined in ASTM E903-20 [54] over a 1 μm range from 400 nm to 1400 nm. The powders were placed in a specially designed polymeric cup that was sealed on the top by a 2 mm thick, uncoated potassium bromide (KBr) window supplied by Edmund Optics Inc. (Barrington, NJ, USA). The width and depth of the cup were such that any contributions of the polymeric material to the reflectance measurement would be minor. KBr was chosen as the sealing material of the window due to its consistently high transmission throughout the range of wavelengths measured. The reflectance of the KBr window was measured separately and subtracted from the powder measurements. Three measurements were taken for each powder and an average reflectance was calculated.

Print surfaces were examined using a MIRA-3 field emission scanning electron microscope (FE-SEM) (TESCAN, Brno, Czech Republic). The cuboid specimens were subjected to three-point bend strength testing with a displacement rate of 0.01 mm/s, and a load applied across the build direction using an MTS 810 load frame (MTS Systems Corporation, Eden Prairie, MN, USA). A diagram of the orientation of the applied load compared to the print samples is shown in Figure 4.6.

Measurements were taken on three samples from each scan speed and the results

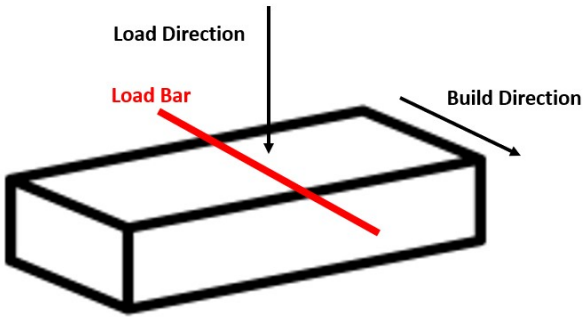

Figure 4.6. Diagram of the applied three point load. Measurements taken in this orientation result in fracture across the columnar grain structure seen along the build direction of many AM metals.

were averaged. Following bend strength measurements, the fracture surfaces were examined with FE-SEM imaging and analyzed via energy dispersive X-ray spectroscopy (EDS) using an EDAX TEAM Pegasus system (Ametek Materials Analysis Division, Mahwah, NJ, USA). The broken specimens were mounted in a conductive phenolic powder resin using a MetPress A automatic mounting press (Metlab, Niagara Falls, NY, USA) so that both the transverse and longitudinal surfaces were available for inspection. The specimens were mechanically ground to 800 grit with silicon carbide grinding paper using an EcoMet 300 grinding and polishing machine (Buehler, Lake Bluff, IL, USA). Vickers hardness measurements were conducted on the top surfaces using a QAtm QNess Q60 A+ Evo micro hardness tester (Verder Scientific, Newtown PA, USA).

Select samples were additionally polished with diamond suspension down to 1 μm and vibro-polished in an Saphir Vibro vibratory polishing device (ATM, Germany) using colloidal silica for 17 hours. The samples were analyzed by both electron backscatter diffraction (EBSD) and EDS using the EDAX TEAM Pegasus system. EBSD mapping was conducted at a beam voltage of 18 kV with an intensity set at 18. Three maps using the largest view field possible were taken of both the top and side surfaces. Cleanup of the maps was conducted using confidence interval (CI) stan-

dardization with a CI of 0.2 and lower being thresholded out. The majority of these points were in pores and their removal created less distraction in the maps. Grain boundary maps and kernal area misorientation (KAM) maps were also analyzed using the EDAX's OIM Analysis software.

The transverse surfaces of select cuboid specimens were further polished to 1200 grit such that only the pores present could be observed and not the cracks and grain boundaries. Cross-sections showing the transverse surfaces within the bulk of the samples were observed using optical microscopy, and three different images with a size about 2.4 x 1.8 mm were taken for each sample from the center position in the height. Those OM images were analyzed with imaging software using a binary process for evaluating the porosity was performed using the same threshold for all images. An automatic mode for calibrated greyscale detection was used to achieve constant measurement conditions. The software measures the total area of the sample and the percentage of black (defects) and white (metal) areas [30]. In this way, the average porosity for each sample was determined optically [98].

Images were taken of the plane horizontal to the build direction with width of roughly 2 mm x 2 mm. The average porosity values and standard deviations were estimated from 5 measurements. The image analysis method evaluates the porosity on the polished surfaces [145]. The porosity was calculated from the porosity area fraction, measured by OM from the average of transverse and longitudinal surfaces of the polished block specimens [146].

The Mo-0.1SiC cuboid specimen printed at 400 mm/s was prepared for TEM analysis by a LYRA3 GM focused ion beam (FIB) (TESCAN, Brno, Czech Republic). TEM and EDS analyses were carried out on a Talos F200X (Thermofisher Scientific, Waltham, MA, USA). The sample prepared for TEM analysis was oriented so that the viewing direction was through the build direction.

4.2 Results

4.2.1 Powder Analysis

The chemical composition of the starting feedstock powders and consolidated pure molybdenum and Mo-0.1SiC specimens are shown in Table 4.2. The nano-sized silicon carbide powder had a much greater concentration of oxygen present and resulted in a slight increase of oxygen in the mixed powders over the pure molybdenum. The carbon present in both the pure molybdenum and Mo-0.1SiC specimens was affected by the experimental setup. No carbon should be present in the pure molybdenum samples and the limited increase in the Mo-0.1SiC samples indicates a significant amount of carbon was lost during the build process. Nitride formation due to the nitrogen build atmosphere was more prevalent in the Mo-0.1SiC samples but no significant pattern was observed. Oxygen concentration positively correlates with increasing scan speed (decreasing LED and VED). The pure molybdenum samples do not show a trend in oxygen concentration with scan speed.

Table 4.2. Chemical composition of powders and LPBF specimens.

Sample	O (ppm)	N (ppm)	C (ppm)
Mo Powder	252	N/A	N/A
SiC Powder	9623	N/A	N/A
Mo-0.1SiC Powder	337	N/A	N/A
Mo (100 mm/s)	1730	420	80
Mo (200 mm/s)	2120	430	100
Mo (400 mm/s)	2190	290	130
Mo (800 mm/s)	1970	230	110
Mo-0.1SiC (100 mm/s)	828	650	120
Mo-0.1SiC (200 mm/s)	852	490	170
Mo-0.1SiC (400 mm/s)	1138	610	140
Mo-0.1SiC (800 mm/s)	1325	370	210

Figure 4.7 shows the room temperature reflectance of the pure molybdenum and Mo-0.1SiC powders. The reflectance of the Mo-0.1SiC powder is about 5% higher than

the molybdenum powder throughout the measured range. A Kubelka-Munk analysis results in k/s values of 2.0 and 1.5 for molybdenum and Mo-0.1SiC, respectively. A smaller k/s value for the Mo-0.1SiC highlights a larger contribution from scattering due to the addition of the silicon carbide nanoparticles.

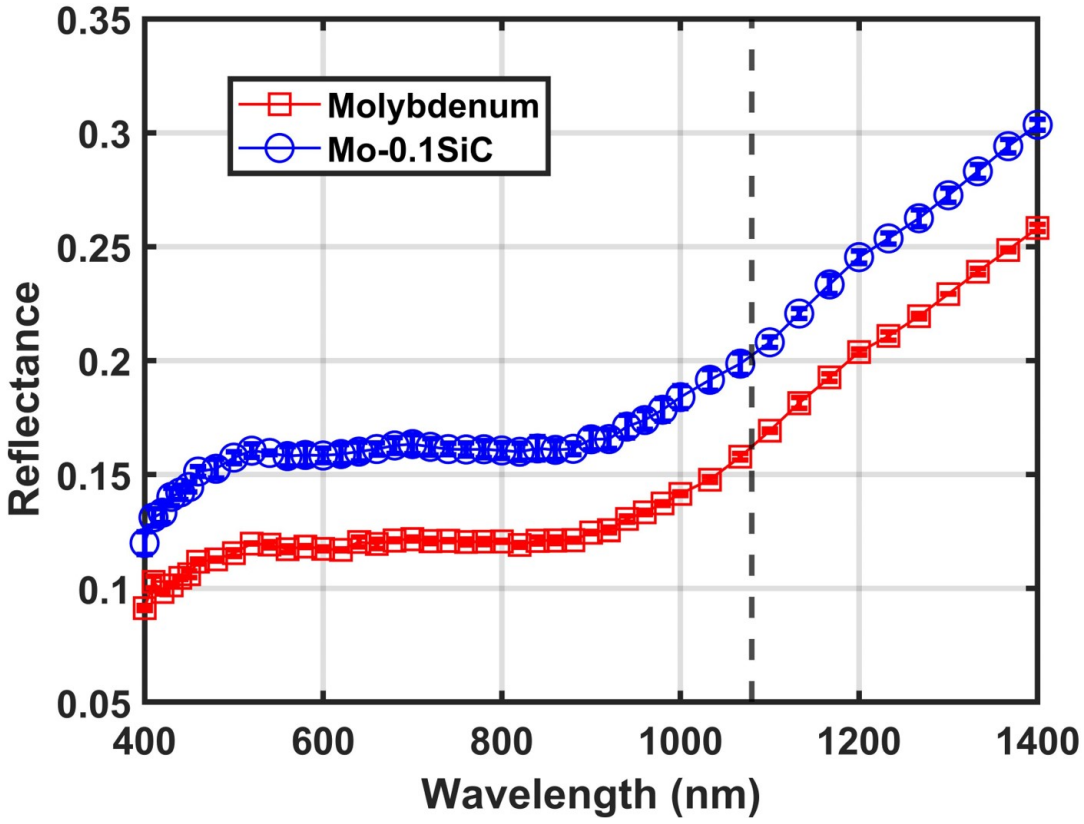

Figure 4.7. Reflectance of the pure molybdenum and Mo-0.1SiC powders presented for a range of wavelengths from 400 to 1400 nm. The wavelength of the laser in the LPBF machine is 1080 nm. This is represented by the black dashed line.

Diffuse reflectance measurements and the K-M analysis are highly sensitive to the preparation and analysis methods used. Most importantly, the scattering coefficient is susceptible to differences in the packing density of the powder particles. It is likely that a combination of the preparation method described in Section 4.1, the shipping of the samples, and the subsequent handling by the testing facility could have led to morphology and packing changes in the powder samples that are not quantifiable.

The samples measured were prepared as a proof-of-concept measurement, and as such, with only one replicate of each powder composition, the analysis should be considered inconclusive. While measurement in this manner has been proven possible, future studies should ensure a standardized and reproducible process is implemented in order to achieve consistent powder properties. Additionally, samples should be sent with enough replicates to statistically account for any variations still present.

4.2.2 Microstructural Characterization

Figures 4.8 and 4.9 show the top surfaces of pure molybdenum and Mo-0.1SiC specimens for the four different scan speeds. Cracking is noted on all samples although their presence in the pure molybdenum is obscured by the porosity. The addition of silicon carbide did not prevent that cracking that appears along the weld tracks and 45° to the weld direction as is commonly seen in welding images of tungsten and molybdenum. As mentioned previously, this is commonly due to the high DBTT of refractory metals and grain boundary embrittlement during the LPBF process. Surface morphology was negatively affected by an increase in scan speed for both the pure molybdenum and Mo-0.1SiC. At lower scan speeds, the weld tracks are less noticeable than at higher scan speeds. Surface porosity was greatly reduced in the samples with silicon carbide additions at all scan speeds.

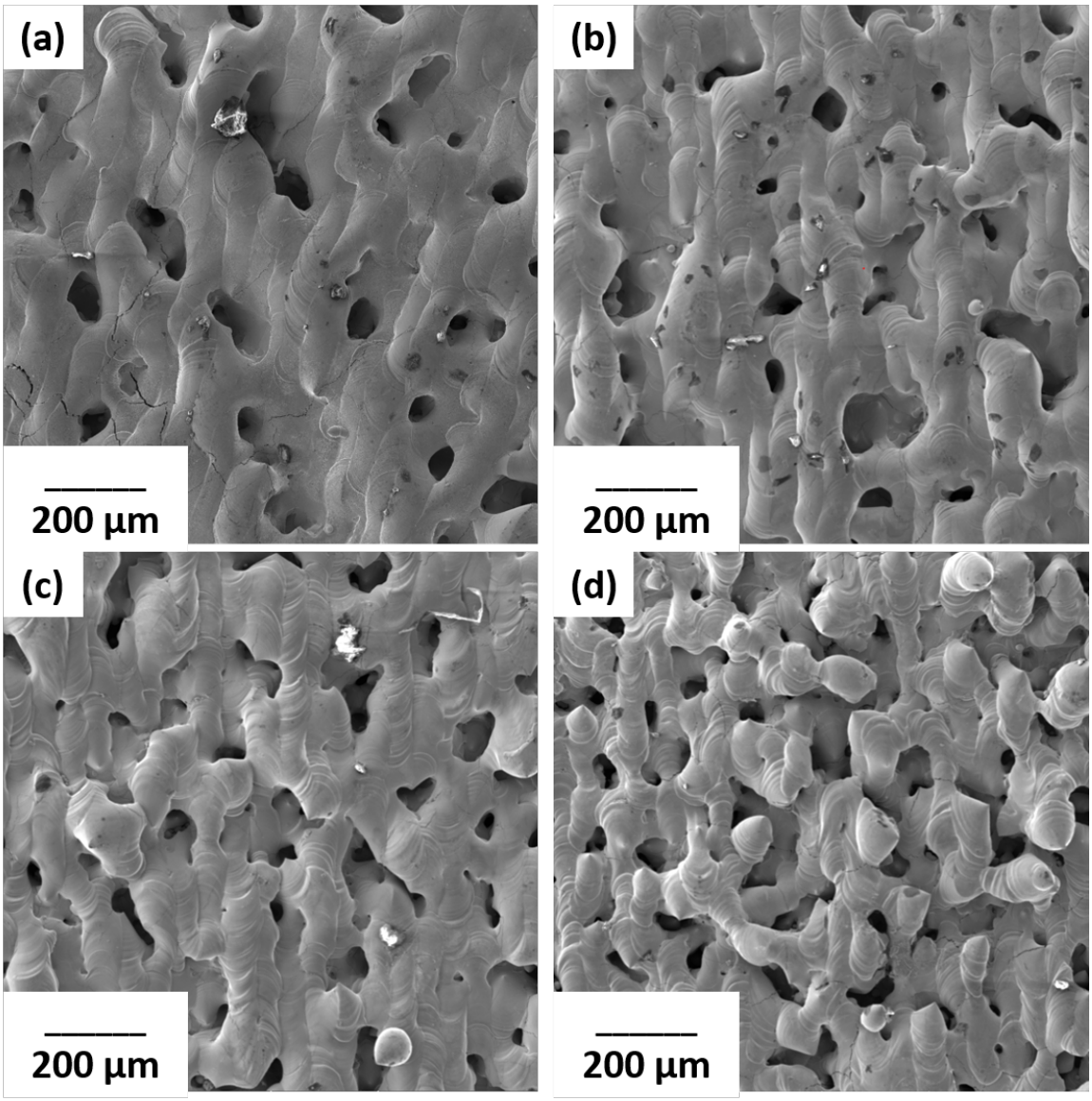

Figure 4.8. SEM images of the top surfaces of the pure molybdenum samples at all four scan speeds: 100, 200, 400, and 800 mm/s, (a–d), respectively.

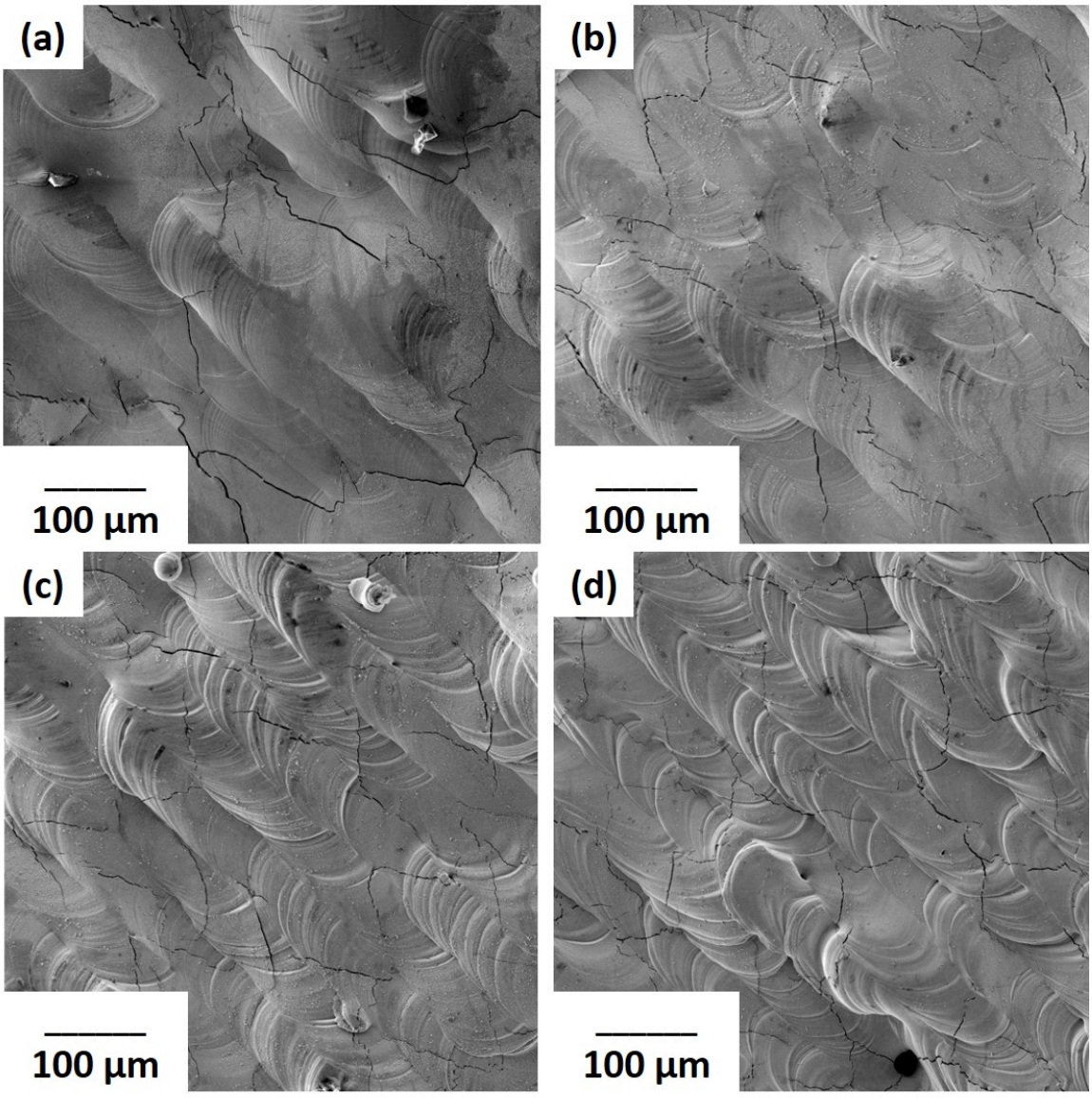

Figure 4.9. SEM images of the top surfaces of the Mo-0.1SiC samples at all four scan speeds: Mo-0.1SiC printed at 100, 200, 400, and 800 mm/s (a–d), respectively.

The ground and polished surfaces of the sectioned samples provided a bulk surface for porosity analysis. Comparisons of the surfaces are shown in Figures 4.10 and 4.11.

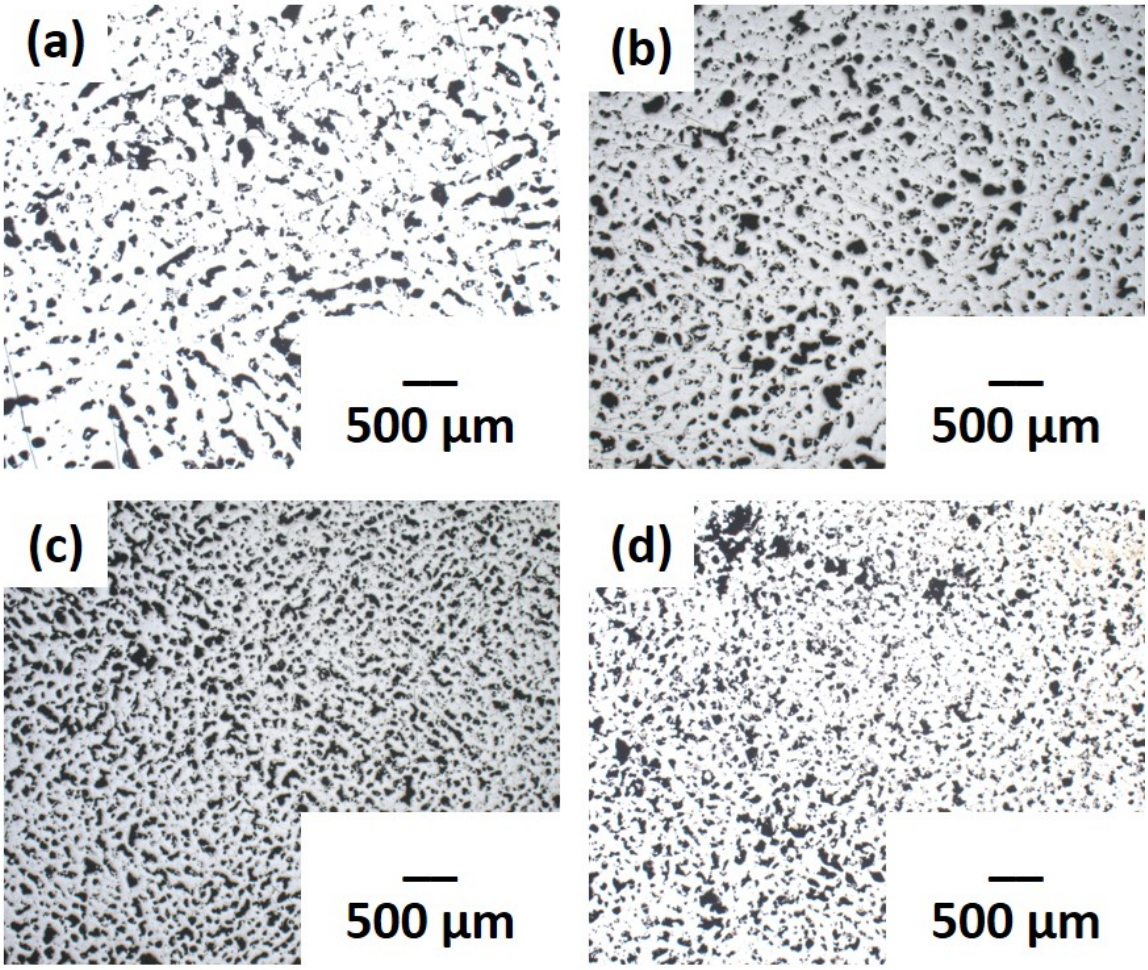

Figure 4.10. Optical images of bulks surfaces showing the porosity of the pure molybdenum at all four scan speeds: 100, 200, 400, and 800 mm/s, (a–d), respectively.

The consolidation in the pure molybdenum samples was very poor and the porosity does not show any regularity. The Mo-0.1SiC specimens showed improved consolidation and the pores were present along the weld tracks. The porosity lost its structure in the Mo-0.1SiC specimens printed at higher scan speeds, with the print at 400 mm/s showing the least porosity of all samples.

The average porosity values are given in Table 4.3. The values for Mo-0.1SiC are

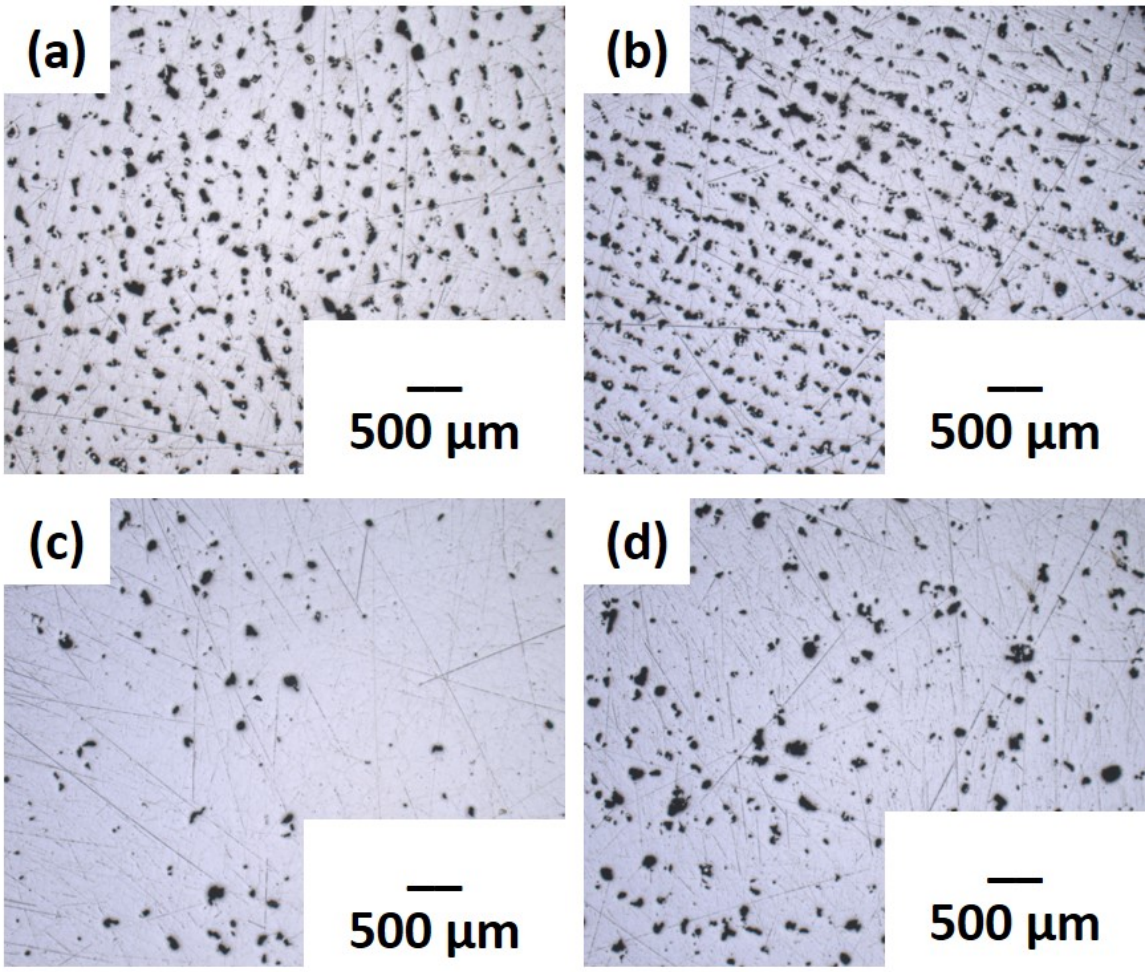

Figure 4.11. SEM images of the top surfaces of the Mo-0.1SiC samples at all four scan speeds: 100, 200, 400, 800 mm/s, (a–d), respectively.

significantly reduced compared to those of molybdenum, with the prints at 400 mm/s showing the largest disparity.

Table 4.3. Optically determined porosity values for all prepared specimens.

Material	100 mm/s	200 mm/s	400 mm/s	800 mm/s
Molybdenum	16.6 ± 2.2%	29.3 ± 2.6%	34.1 ± 1.2%	25.3 ± 5.5%
Mo-0.1SiC	7.2 ± 1.9%	7.9 ± 3.0%	2.6 ± 0.7%	5.2 ± 0.5%

EBSD maps were collected on all samples in the transverse and longitudinal orientations. The following EBSD maps, KAM plots, and associated data omit images and values for this specimen. Three maps were collected on the rest of the pure

molybdenum and Mo-0.1SiC specimens in order to provide statistical data. Maps were collected at the lowest magnification possible to ensure the largest area of grains were presented for analysis. Inverse pole figures, IPF maps, and KAM maps were generated for each specimen. EDAX OIM Analysis^{TM} software allowed for the determination of average grain diameters, grain orientation spread (GOS), crystallographic texture, and the fraction of high angle grain boundaries (HAGB). In general, the abundant porosity of the pure molybdenum samples prevents the expected trends with scan speed to be observed. The improved consolidation shown in the Mo-0.1SiC specimens allows for observation and discussion of microstructural evolution and mechanical properties to be substantiated by microstructural features and temperature effects as opposed to porosity, lack-of-fusion, and incomplete melting.

Figures 4.12, 4.13, 4.14, and 4.15 display the IPF maps and KAM plots for pure molybdenum printed at 100, 200, 400, and 800 mm/s respectively. Average grain diameters corresponding to the EBSD maps are given in Table 4.4.

Table 4.4. Average grain diameter (μm) for the transverse (XY) and longitudinal (XZ) directions of the pure molybdenum samples corresponding to Figures 4.12, 4.13, 4.14, and 4.15.

Scan Speed	**100 mm/s**	**200 mm/s**	**400 mm/s**	**800 mm/s**
XY Avg (Std Dev)	33.65 ± 4.34	27.63 ± 2.54	30.07 ± 3.10	22.91 ± 1.69
XZ Avg (Std Dev)	132.50 ± 26.40	84.28 ± 4.71	61.17 ± 10.30	50.13 ± 3.43

The IPF maps indicate that no there is no preferred crystallographic orientation in either the transverse or longitudinal directions. A texture intensity of 1.0 is representative of a sample with an ideal, random crystallographic structure in which no direction is preferred over another. While a preferred crystal orientation is usually identified in AM metals, the lack of observation in the pure molybdenum samples can be attributed to the abundance of pores in the microstructure limiting the formation of a continuous, uninterrupted grain structure. The EBSD maps reveal the expected columnar nature of grain growth in the longitudinal direction. The grain sizes are

significantly larger than those in the transverse direction at the same scan speed. The expected grain refinement is evident in the longitudinal direction as scan speed increases; however, the transverse direction doesn't show an obvious trend.

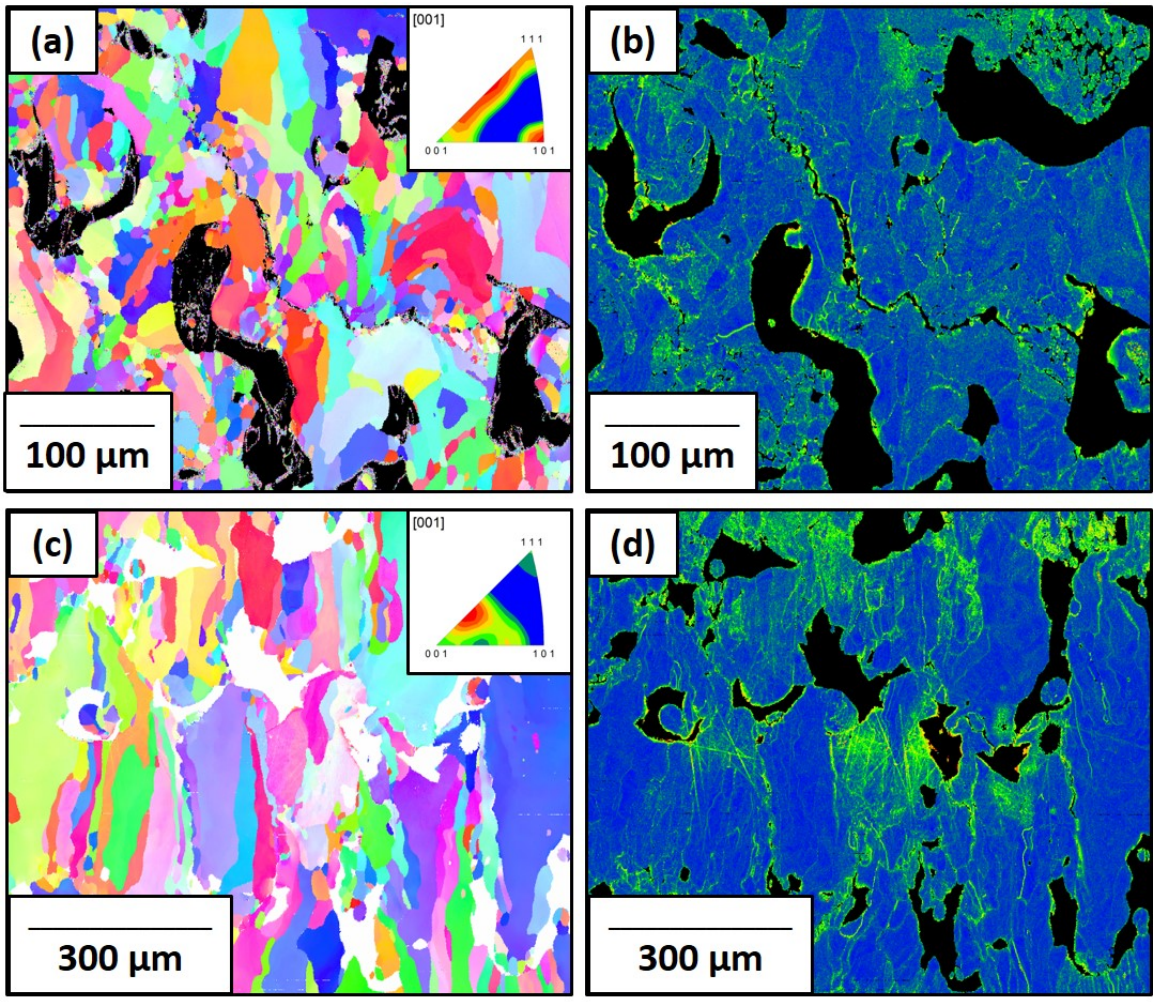

Figure 4.12. IPF maps (a,c) and KAM plots (b,d) for pure molybdenum printed at the 100 mm/s scan speed in the transverse (a,b) and longitudinal (c,d) directions. No preferred crystallographic orientation is identified with maximum IPF intensities of 1.47 and 1.41 in the transverse and longitudinal directions, respectively.

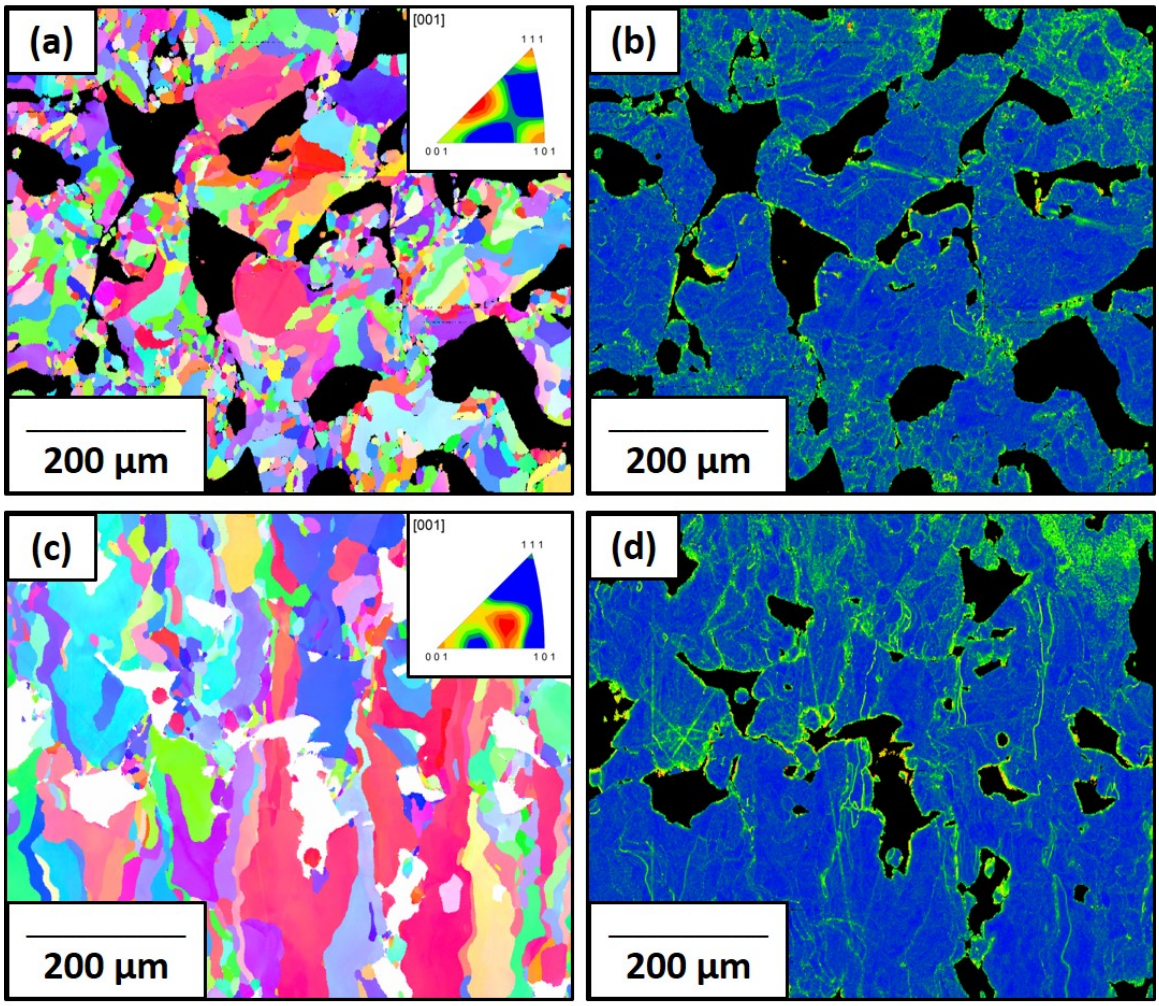

Figure 4.13. IPF maps (a,c) and KAM plots (b,d) for pure molybdenum printed at the 200 mm/s scan speed in the transverse (a,b) and longitudinal (c,d) directions. No preferred crystallographic orientation is identified with maximum IPF intensities of 1.56 and 1.69 in the transverse and longitudinal directions, respectively.

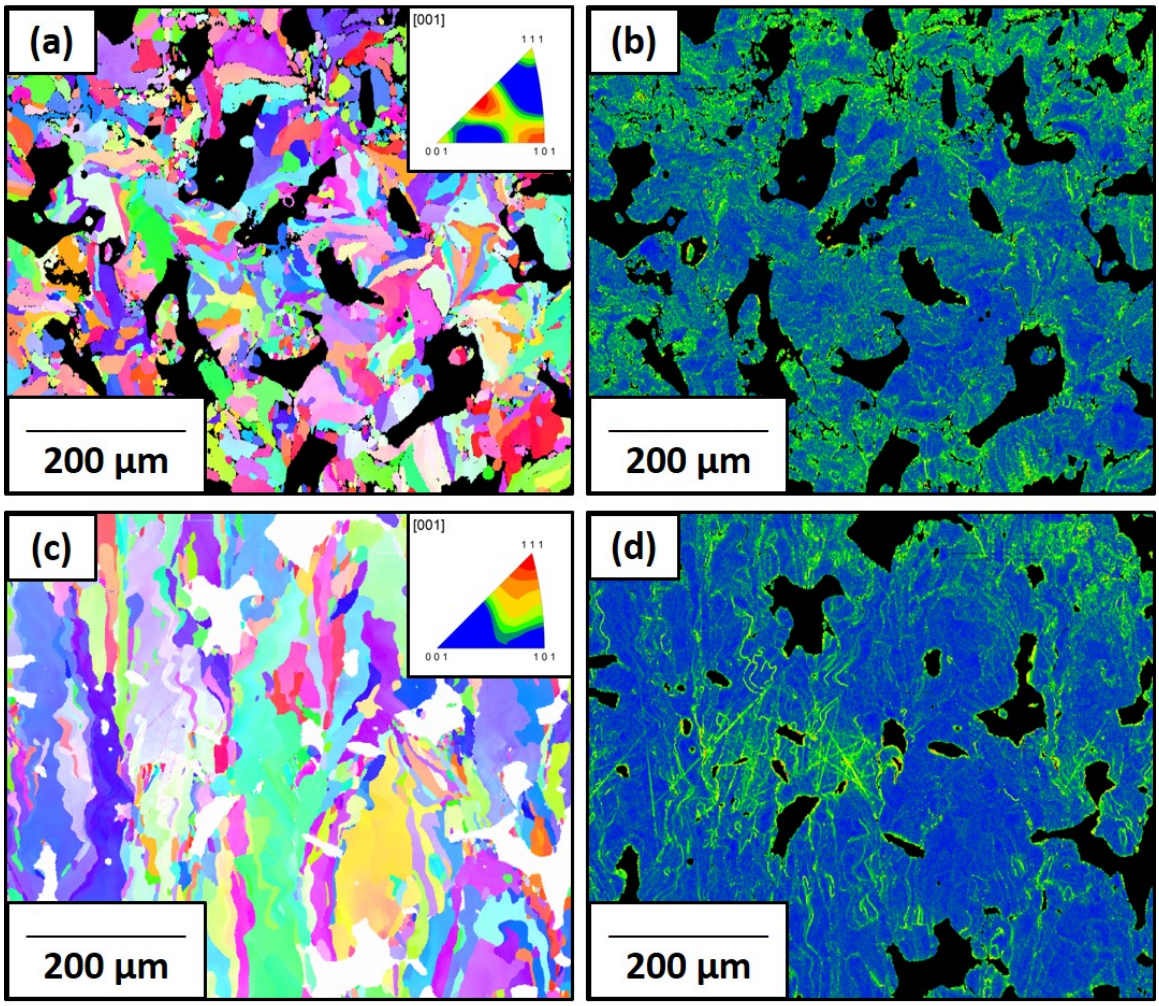

Figure 4.14. IPF maps (a,c) and KAM plots (b,d) for pure molybdenum printed at the 400 mm/s scan speed in the transverse (a,b) and longitudinal (c,d) directions. No preferred crystallographic orientation is identified with maximum IPF intensities of 1.36 and 1.47 in the transverse and longitudinal directions, respectively.

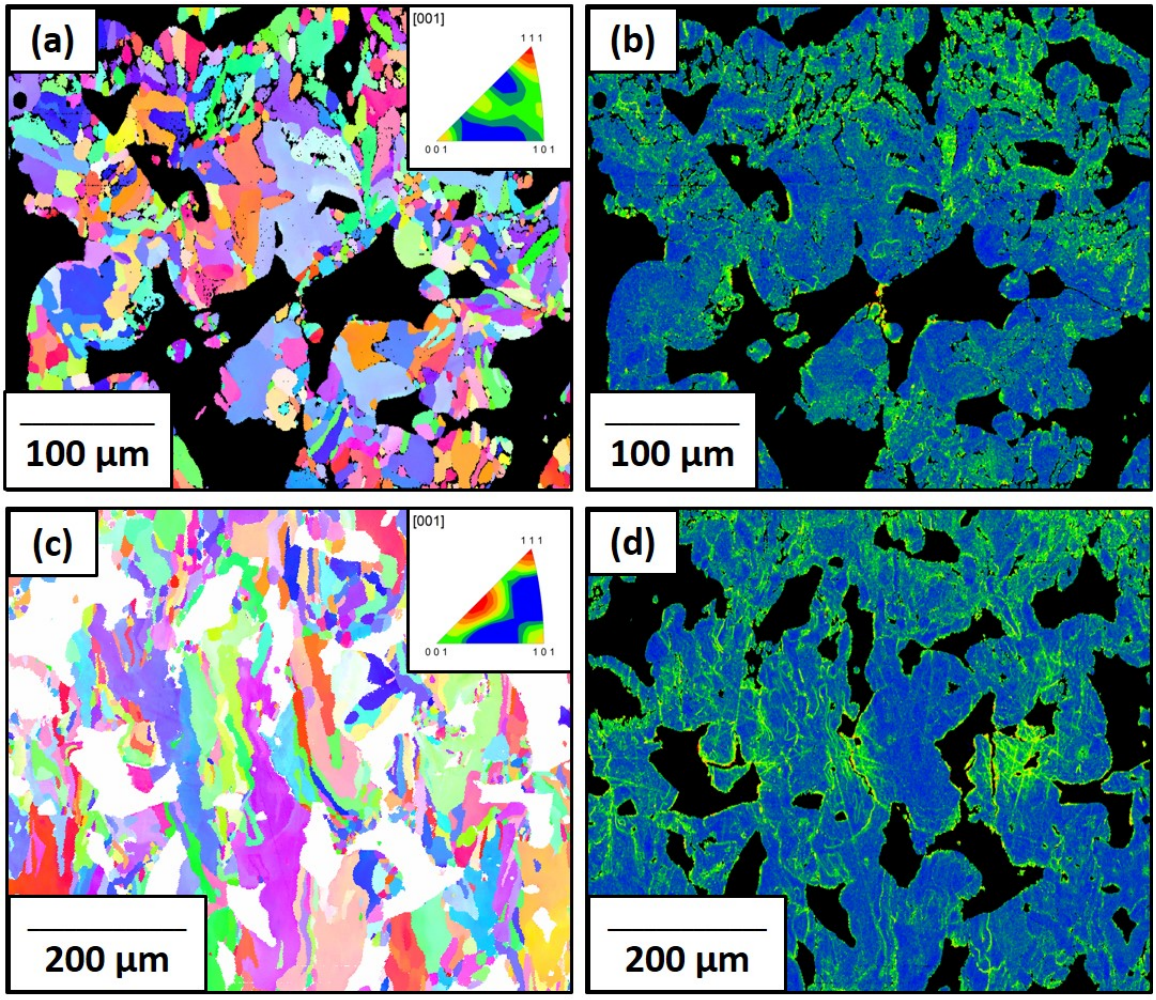

Figure 4.15. IPF maps (a,c) and KAM plots (b,d) for pure molybdenum printed at the 800 mm/s scan speed in the transverse (a,b) and longitudinal (c,d) directions. No preferred crystallographic orientation is identified with maximum IPF intensities of 1.54 and 1.55 in the transverse and longitudinal directions, respectively.

GOS graphs corresponding to the KAM plots are displayed in Figures 4.16, 4.17 for the transverse and longitudinal directions, respectively. The GOS graphs are an indication of residual strains present within the grains. As with other results, the pure molybdenum specimens do not show a clear trend. Due to how the nature of the melt pool changes with laser energy density, less residual strains, or a GOS that favors a high area fraction at the lower angles, is expected at the slower scan speeds. This is exhibited at the 100 mm/s scan speed in both the transverse and longitudinal directions, and through the 400 mm/s scan speed, the residual strain increases, but in both cases the residual stress is reduced in the 800 mm/s. This is postulated to be because at the high scan rate, much of the original grains are from the powder feedstock are still present and retain their original structure and stress state due to never fully melting as seen in Figure 4.15.

Figures 4.18 and 4.19 display the grain boundary analysis that was conducted on the transverse and longitudinal surfaces of the samples. Grain boundaries less than 5° were thresholded out. Green lines represent low-angle grain boundaries, or boundaries with a rotation angle between 5° and 15°. Blue lines represent high-angle grain boundaries (HAGB), or boundaries with a rotation angle between 15° and 180°. Table 4.5 displays the fractions of HAGB for the pure molybdenum specimens in the transverse and longitudinal orientations. As with the other analyses, the pure molybdenum specimens do not display a clearly identifiable trend with the print parameters. As grain sizes decrease, HAGBs are expected to become more prevalent, however this isn't observed in the transverse or longitudinal directions across scan speeds. When comparing orientations, the larger grains in the longitudinal direction do exhibit a lower fraction of HAGB than the smaller grains in the transverse direction.

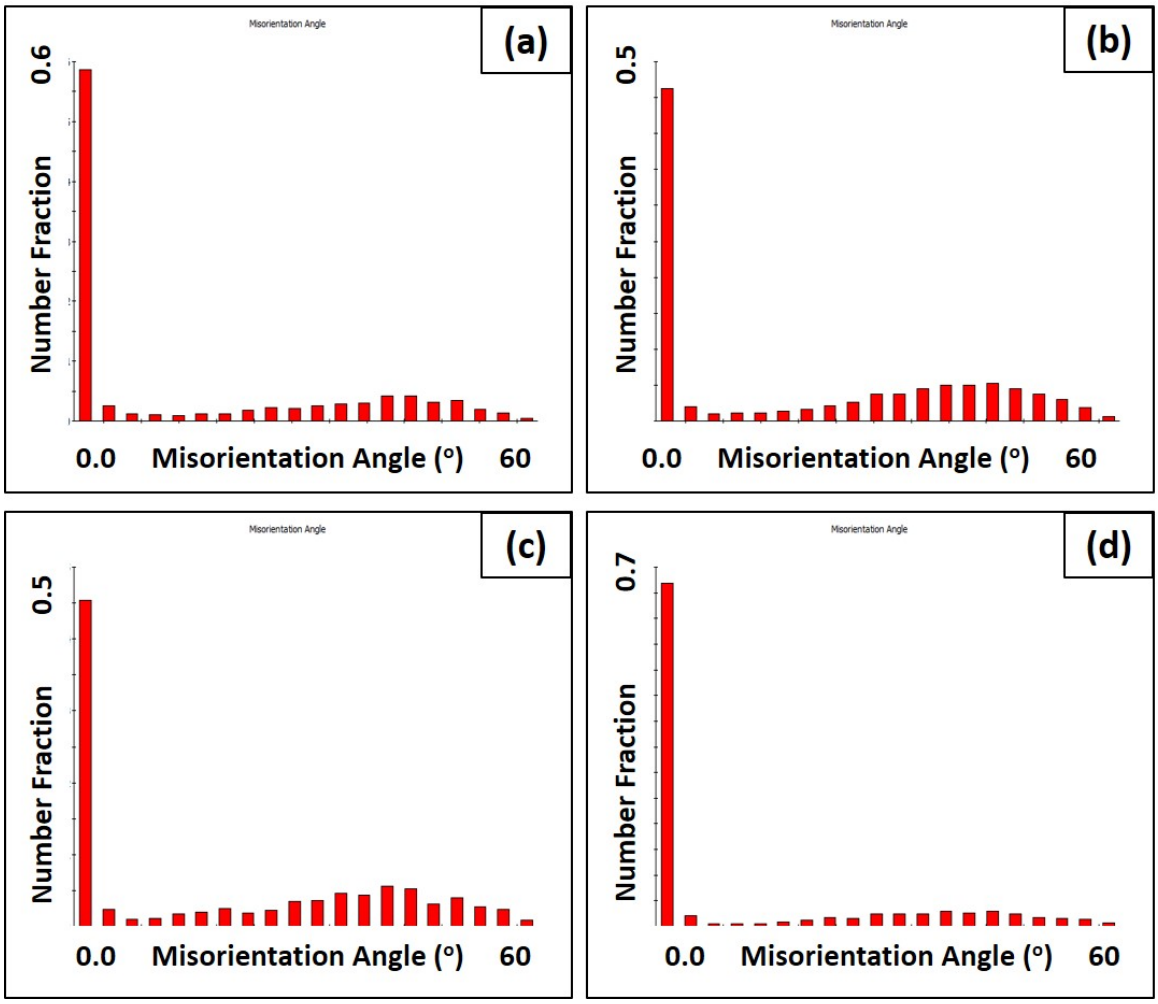

Figure 4.16. Grain orientation spread graphs taken from the transverse surface of the pure molybdenum samples at 100 (a), 200 (b), 400 (c), and 800 (d) mm/s.

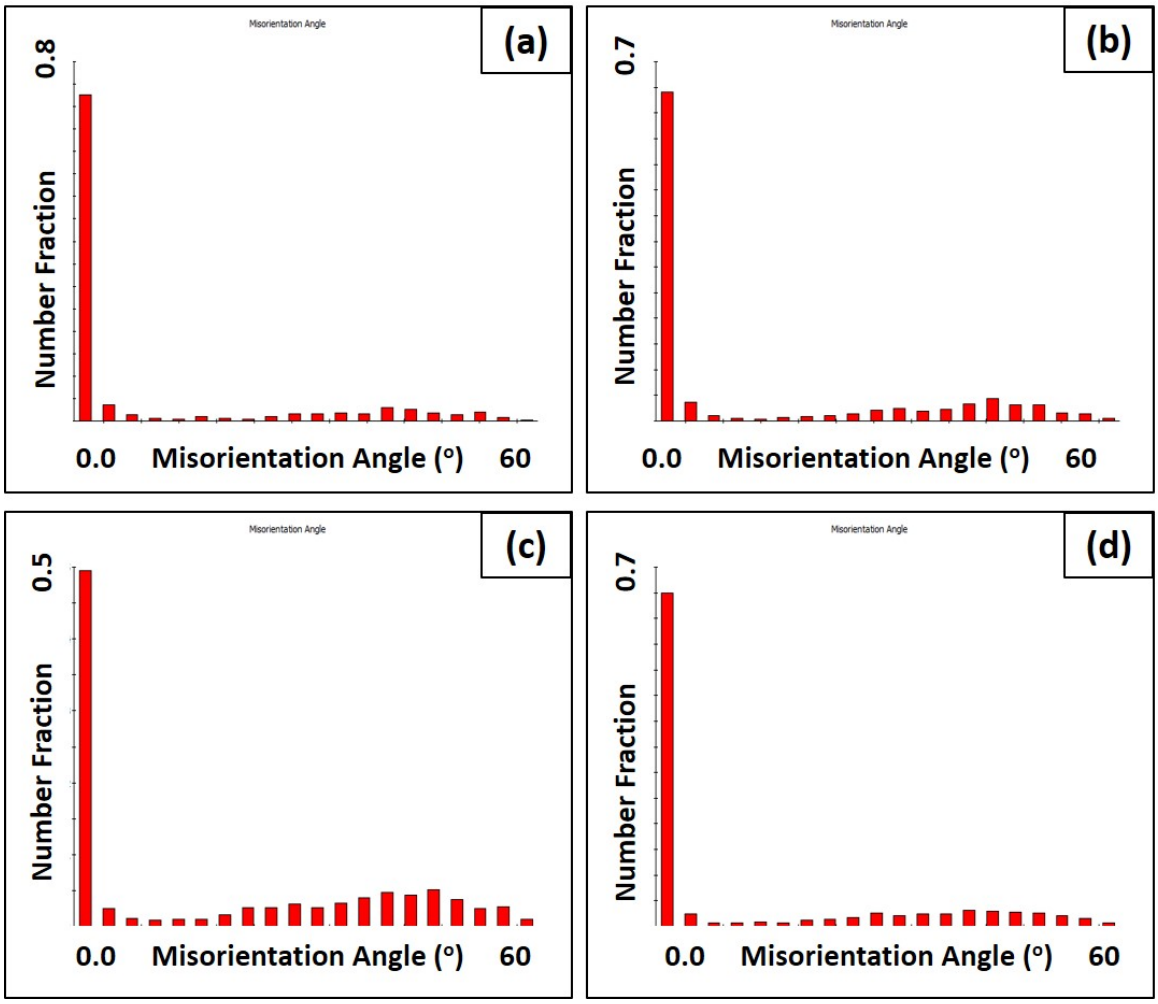

Figure 4.17. Grain orientation spread graphs taken from the longitudinal surface of the pure molybdenum samples at 100 (a), 200 (b), 400 (c), and 800 (d) mm/s.

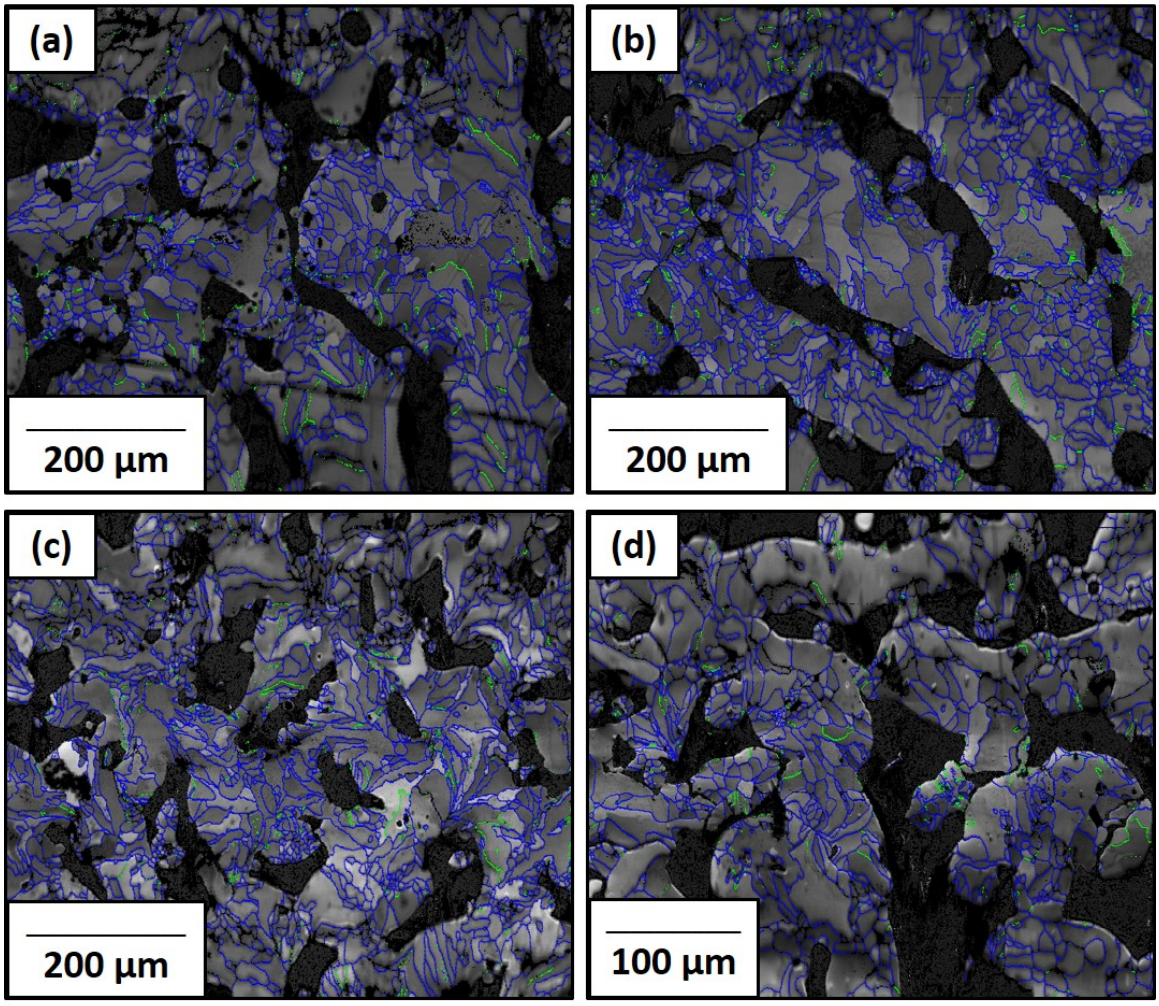

Figure 4.18. Grain boundary analysis maps for the transverse direction of the pure molybdenum samples printed at 100 (a), 200 (b), 400 (c), and 800 (d) mm/s respectively.

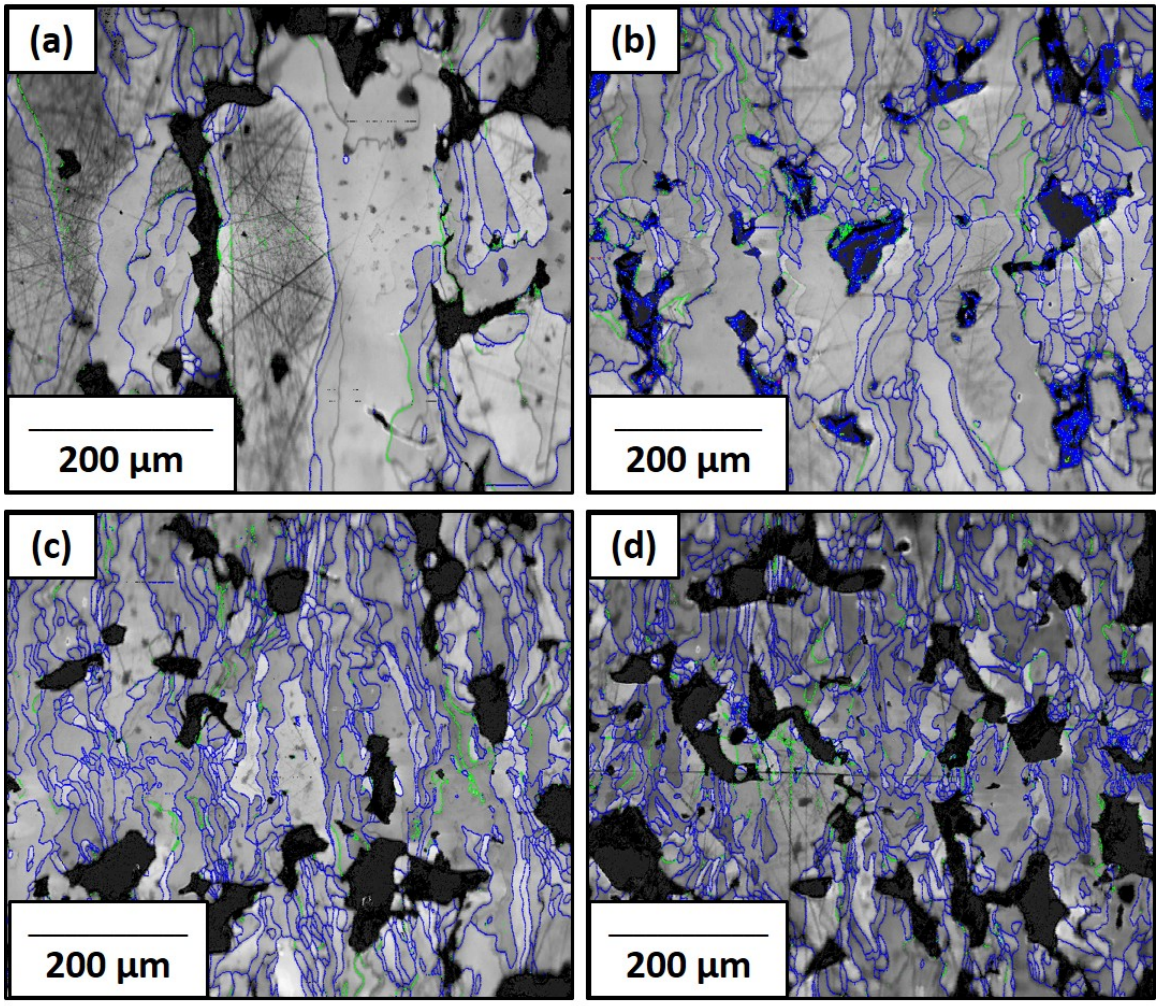

Figure 4.19. Grain boundary analysis maps for the longitudinal direction of the pure molybdenum samples printed at 100 (a), 200 (b), 400 (c), and 800 (d) mm/s respectively.

Table 4.5. Fraction of high angle grain boundaries for the pure molybdenum samples in the transverse (XY) and longitudinal (XZ) orientations corresponding to Figures 4.18 and 4.19, respectively.

Scan Speed	100 mm/s	200 mm/s	400 mm/s	800 mm/s
XY Avg (Std Dev)	0.333 ± 0.023	0.505 ± 0.025	0.450 ± 0.061	0.326 ± 0.025
XZ Avg (Std Dev)	0.144 ± 0.046	0.333 ± 0.026	0.429 ± 0.045	0.318 ± 0.023

Figures 4.20, 4.21, 4.22, and 4.23 display the IPF maps and KAM plots for Mo-0.1SiC printed at 100, 200, 400, and 800 mm/s respectively. Average grain diameters corresponding to the EBSD maps are given in Table 4.6. The disparity between the transverse and longitudinal directions is much larger in the Mo-0.1SiC specimens than the pure molybdenum and they decrease monotonically as scan speed increases.

Table 4.6. Average grain diameter (μm) for the transverse (XY) and longitudinal (XZ) directions of the Mo-0.1SiC samples.

Scan Speed	100 mm/s	200 mm/s	400 mm/s	800 mm/s
XY Avg (Std Dev)	47.94 ± 9.74	42.44 ± 5.89	26.32 ± 0.69	24.34 ± 1.05
XZ Avg (Std Dev)	214.08 ± 29.23	75.25 ± 13.33	64.49 ± 7.21	48.36 ± 8.67

Again, the expected strong columnar grains are present in the longitudinal orientation. Similar to the pure molybdenum specimens there is no strong crystallographic texture in the transverse direction of the Mo-0.1SiC specimens; however there is a strong texture in the longitudinal direction at the 100 mm/s scan speed. The preferred orientation is the <100> crystal direction. There were no strongly preferred directions observed at the 400 and 800 mm/s scan speeds and the max values are no longer located at the <100> vertex.

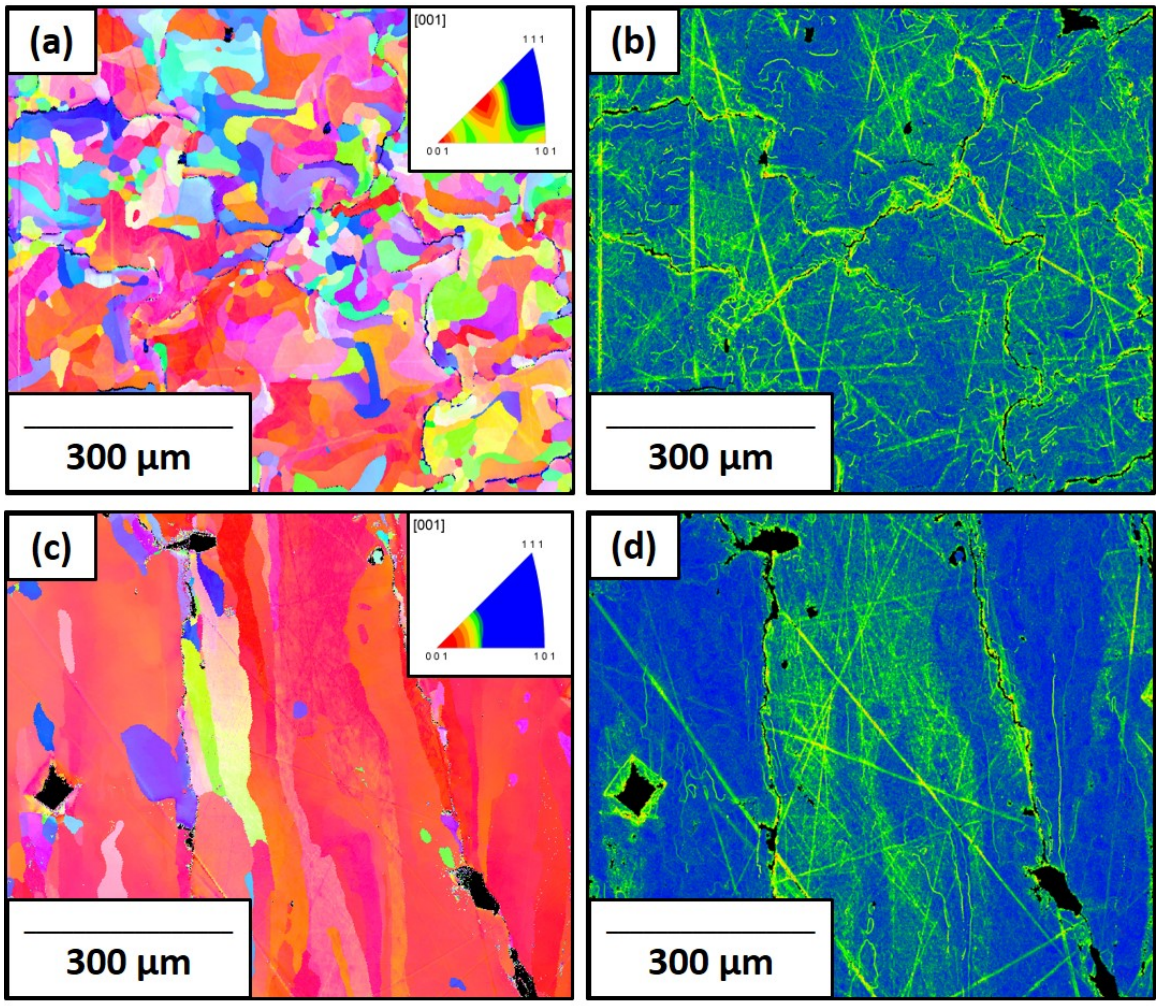

Figure 4.20. IPF maps (a,c) and KAM plots (b,d) for Mo-0.1SiC printed at the 100 mm/s scan speed in the transverse (a,b) and longitudinal (c,d) directions. Maximum IPF intensity is 1.405 and 10.876 in the transverse and longitudinal directions, respectively.

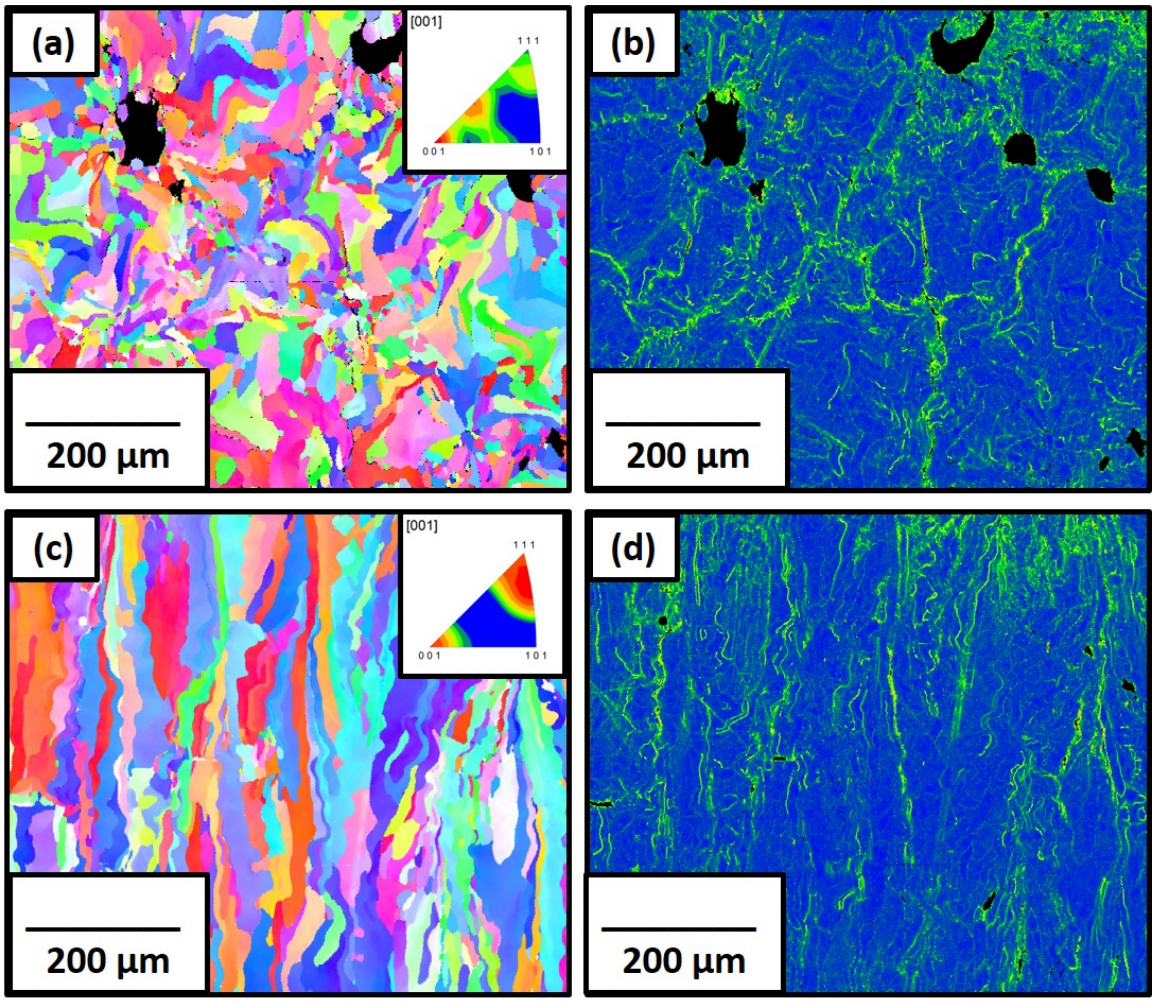

Figure 4.21. IPF maps (a,c) and KAM plots (b,d) for Mo-0.1SiC printed at the 200 mm/s scan speed in the transverse (a,b) and longitudinal (c,d) directions. Maximum IPF intensity is 1.734 and 2.360 in the transverse and longitudinal directions, respectively.

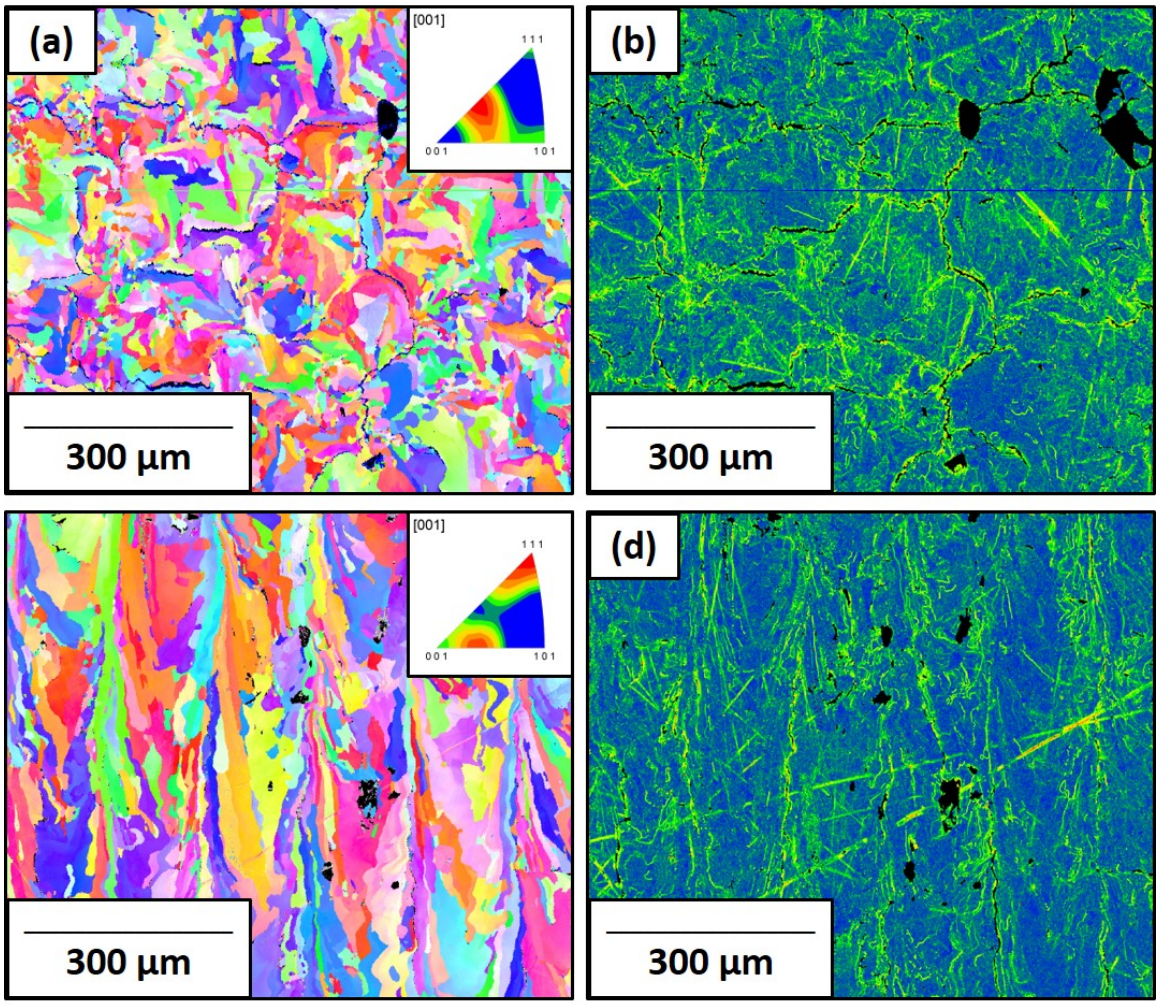

Figure 4.22. IPF maps (a,c) and KAM plots (b,d) for Mo-0.1SiC printed at the 400 mm/s scan speed in the transverse (a,b) and longitudinal (c,d) directions. Maximum IPF intensity is 1.544 and 1.268 in the transverse and longitudinal directions, respectively.

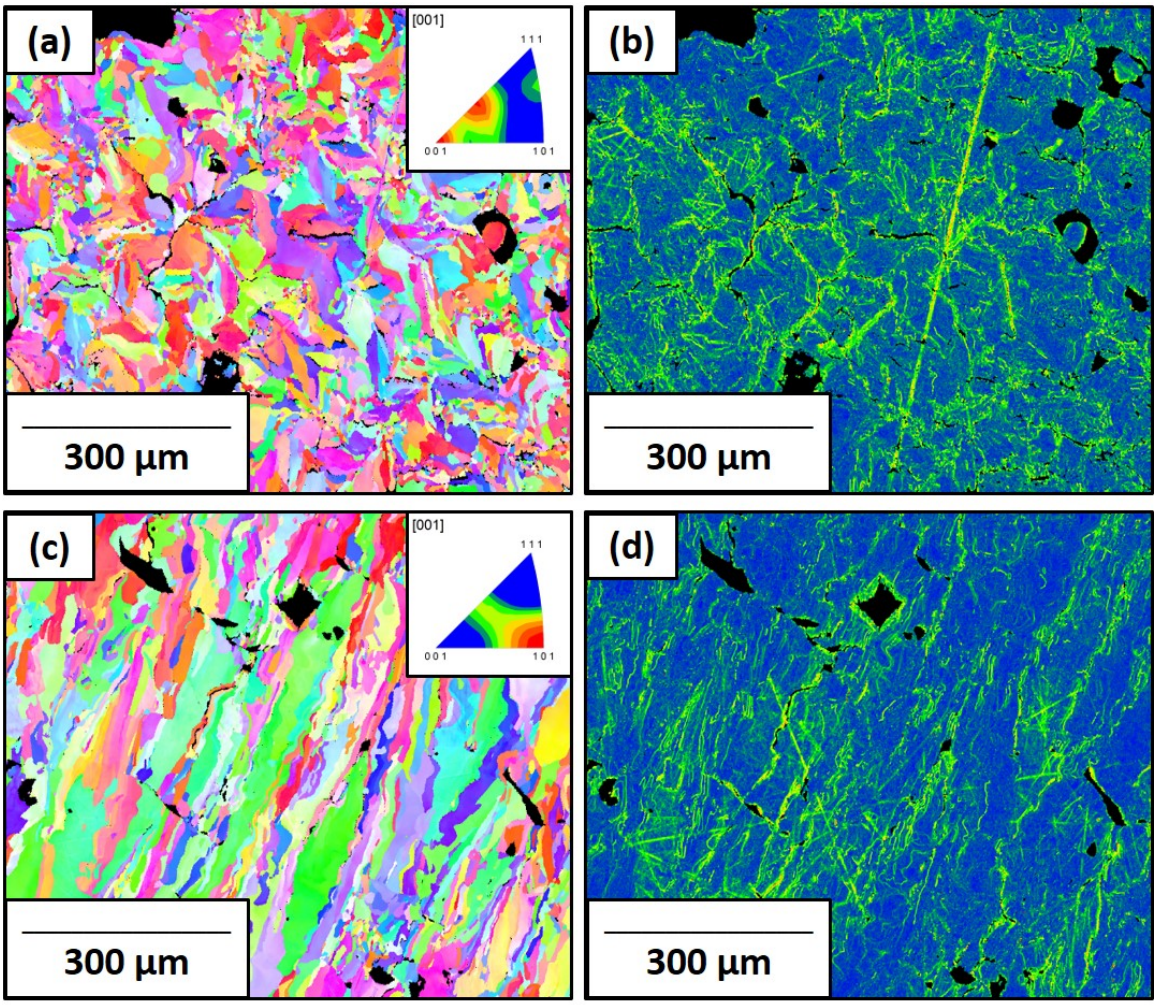

Figure 4.23. IPF maps (a,c) and KAM plots (b,d) for Mo-0.1SiC printed at the 800 mm/s scan speed in the transverse (a,b) and longitudinal (c,d) directions. Maximum IPF intensity is 1.399 and 1.590 in the transverse and longitudinal directions, respectively.

GOS graphs corresponding to the KAM plots are displayed in Figures 4.24, 4.25 for the transverse and longitudinal directions, respectively. The GOS data shows that the residual stresses present in the Mo-0.1SiC specimens are much reduced compared to the pure molybdenum specimens at comparable scan speed. The GOS values decrease with increasing scan speeds which corresponds to a growth in residual stress.

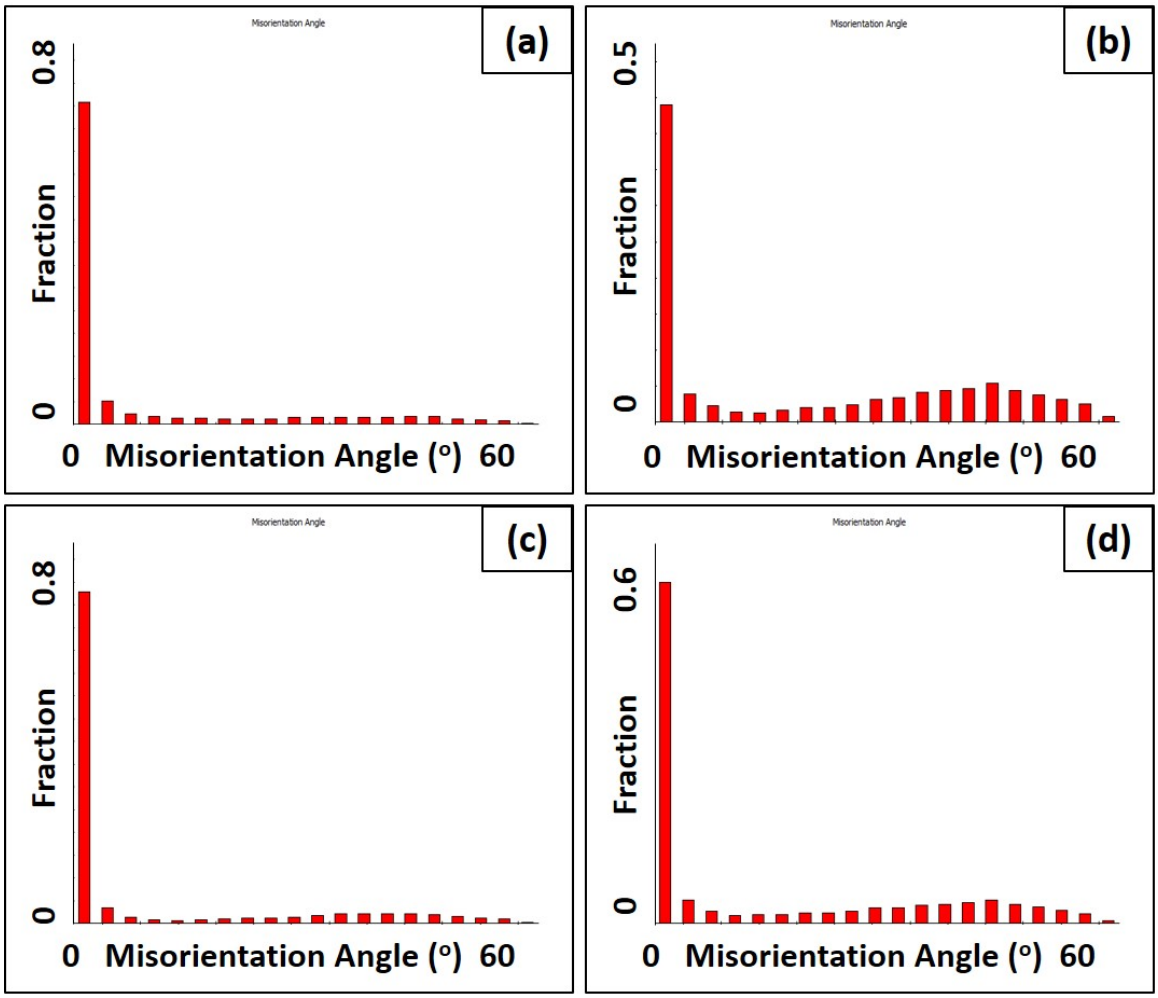

Figure 4.24. Grain orientation spread graphs taken from the transverse surface of the Mo-0.1SiC samples at (a) 100, (b) 200, (c) 400, and (d) 800 mm/s.

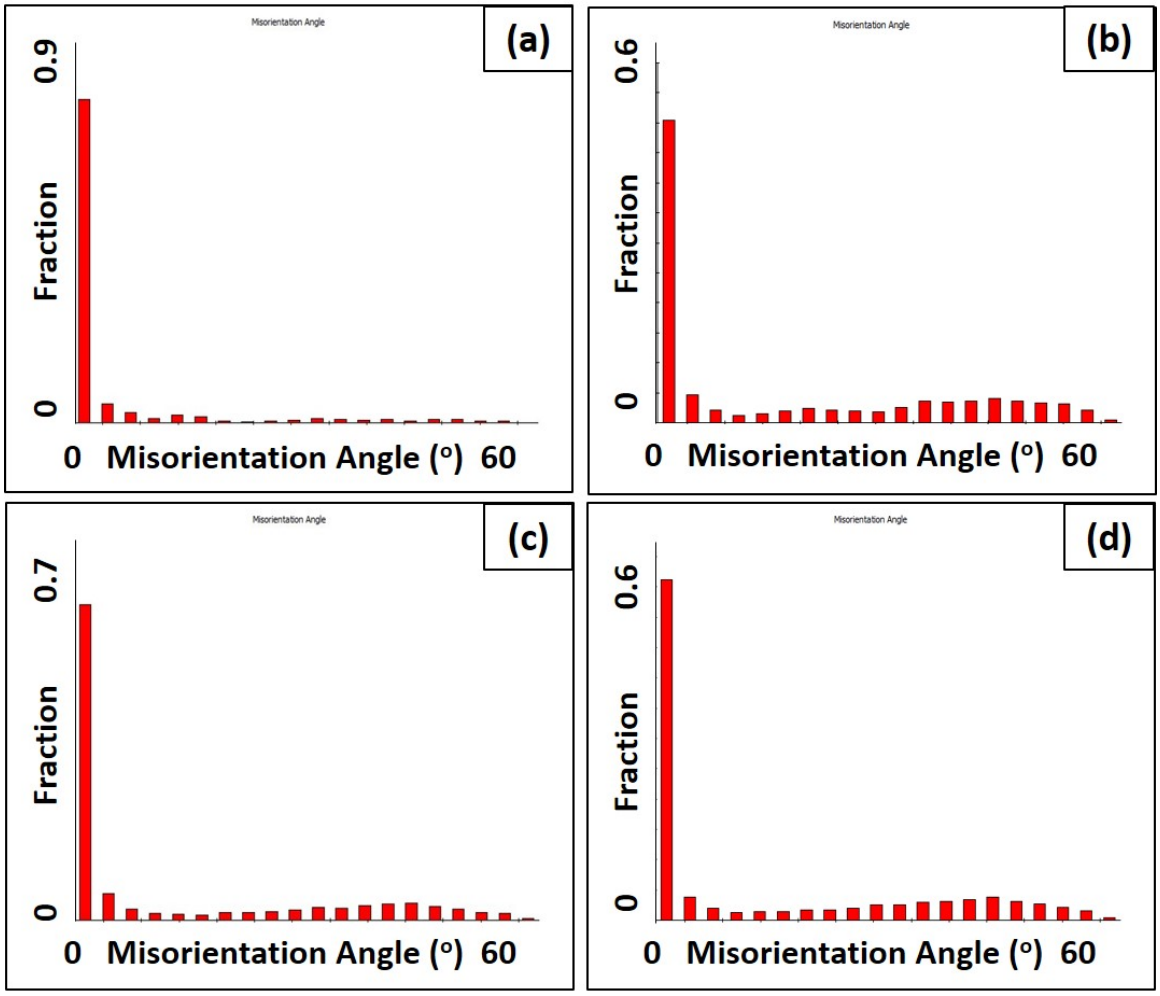

Figure 4.25. Grain orientation spread graphs taken from the longitudinal surface of the Mo-0.1SiC samples at (a) 100, (b) 200, (c) 400, and (d) 800 mm/s.

Figures 4.26 and 4.27 display the grain boundary analysis that was conducted on the transverse and longitudinal surfaces of the Mo-0.1SiC specimens. These maps clearly show the grain refinement seen with increasing scan speed. The fractions of HAGB for the pure molybdenum specimens in transverse and longitudinal directions corresponding to the grain boundary maps are displayed in Table 4.7. With the vast difference in grain sizes between the two directions at the 100 mm/s it is unsurprising to see that mirrored in the fraction of HAGBs. HAGBs are more prevalent at the higher scan speeds as grain size decreases, however at the 400 and 800 mm/s scan speeds the transverse and longitudinal directions have very similar fractions even though the grain sizes between the two directions at these scan speeds are significantly different.

Table 4.7. Fraction of high angle grain boundaries for the Mo-0.1SiC samples in the transverse (XY) and longitudinal (XZ) directions.

Scan Speed	**100 mm/s**	**200 mm/s**	**400 mm/s**	**800 mm/s**
XY Avg (Std Dev)	0.216 ± 0.043	0.441 ± 0.27	0.267 ± 0.077	0.397 ± 0.004
XZ Avg (Std Dev)	0.091 ± 0.017	0.429 ± 0.016	0.238 ± 0.068	0.369 ± 0.032

Figure 4.28 shows the TEM/EDS analysis maps that were generated for the Mo-0.1SiC specimen printed at 400 mm/s. EDS identifies the content of the secondary phase nanoparticles as almost entirely silicon and oxygen, devoid of any molybdenum. EDS analysis indicated that there was not any carbon present, above background, in or around the nanoparticles. The presence of multiple nanoparticles was first noticed in the TEM imaging which suggests a large number of occurrences throughout the material.

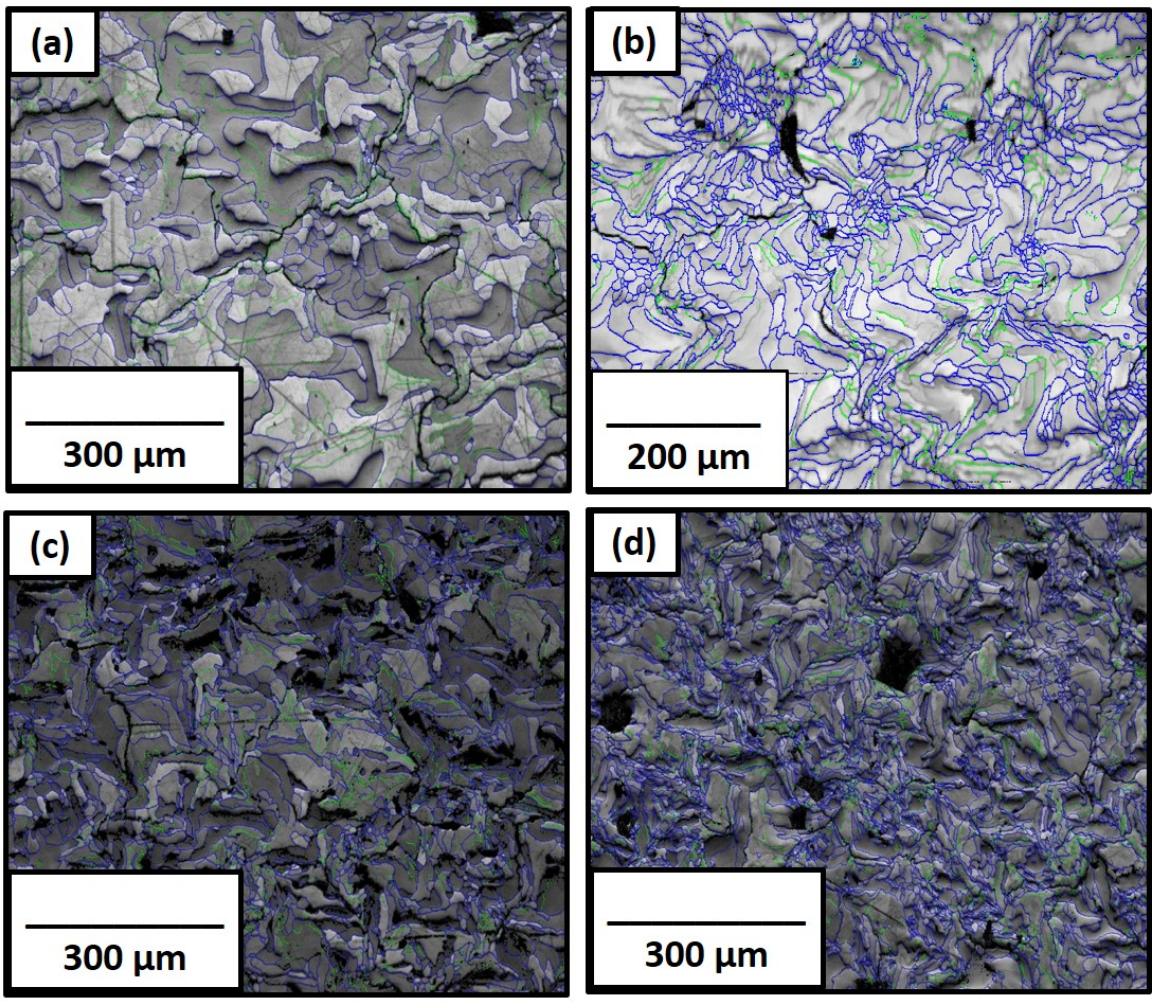

Figure 4.26. Grain boundary analysis maps for the transverse direction of the Mo-0.1SiC samples printed at 100 (a), 400 (b), and 800 (c) mm/s respectively.

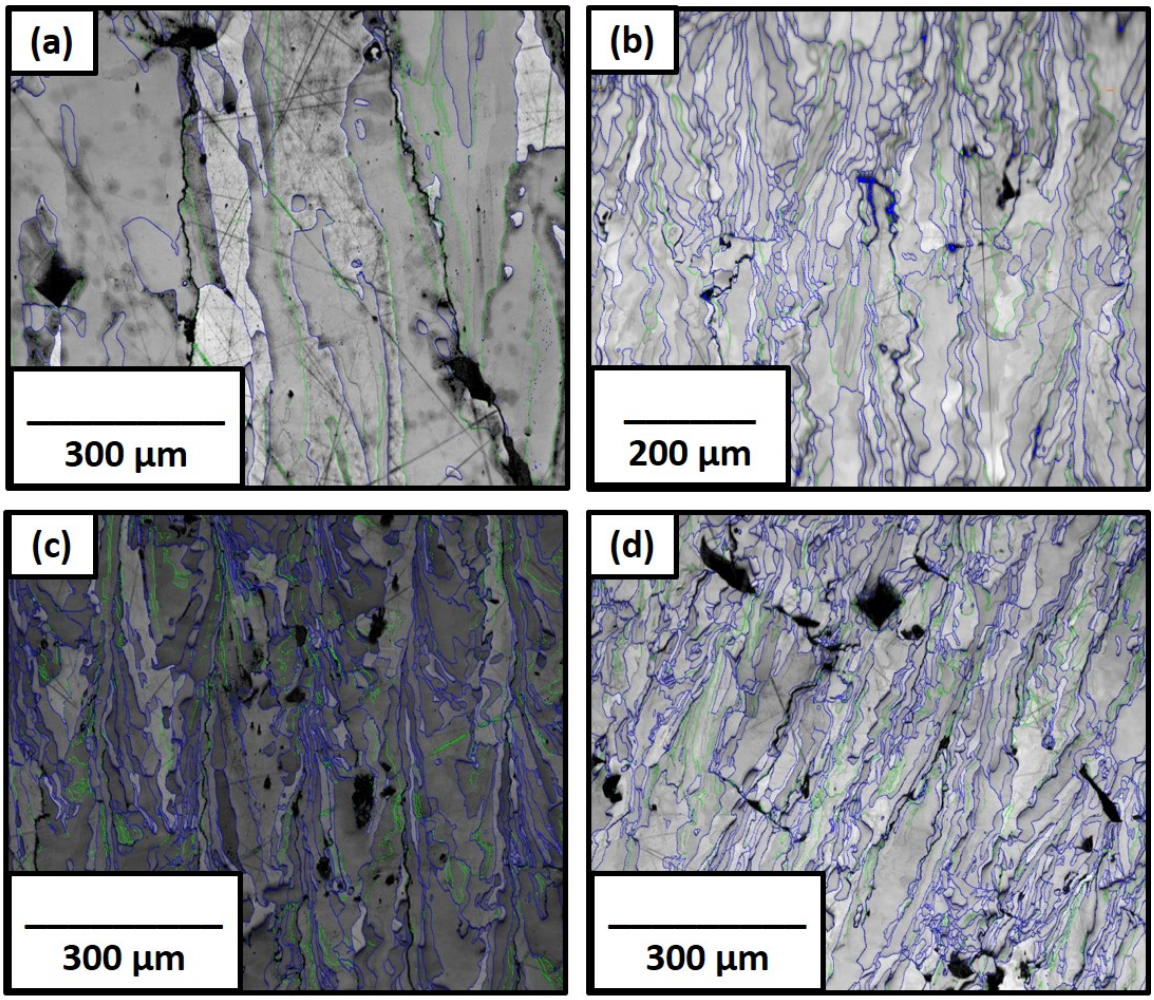

Figure 4.27. Grain boundary analysis maps for the longitudinal direction of the Mo-0.1SiC samples printed at (a) 100, (b) 200, (c) 400, and (d) 800 mm/s respectively.

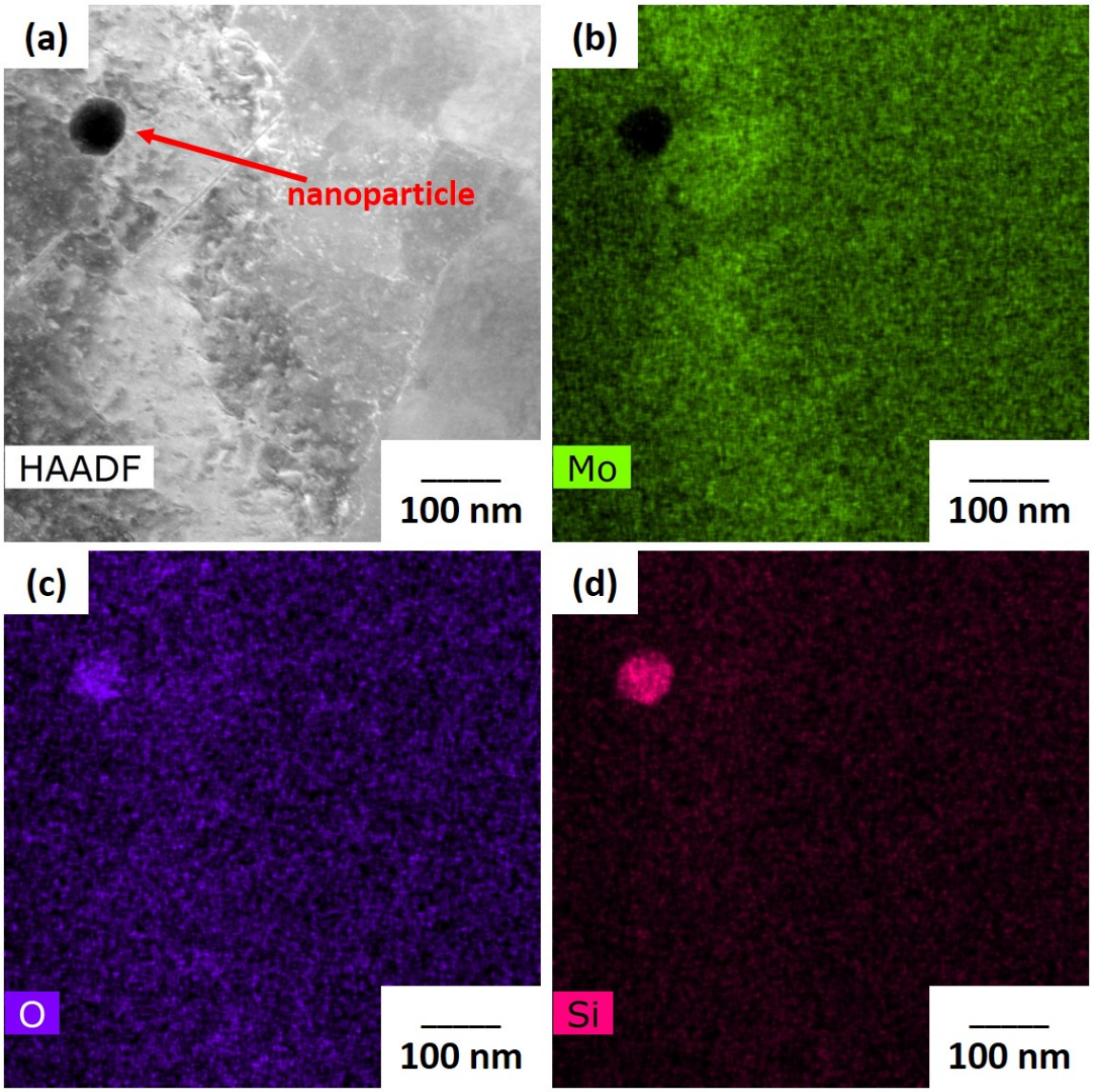

Figure 4.28. EDS analysis of the nanoparticles conducted via TEM. (a) High-annular dark field (HAADF) image. (b) EDS map with molybdenum highlighted. (c) EDS map with oxygen highlighted. (d) EDS map with silicon highlighted.

SEM imaging was conducted to verify the abundance of the nanoparticles. The SEM and point EDS results of the etched surface are shown in Figure 4.29. The point SEM/EDS analysis and TEM/EDS analysis are in agreement that the nanoparticles are primarily silicon and oxygen. Furthermore, the point EDS analysis shows that silicon was not present in the bulk but instead contained only in the nanoparticles

present throughout.

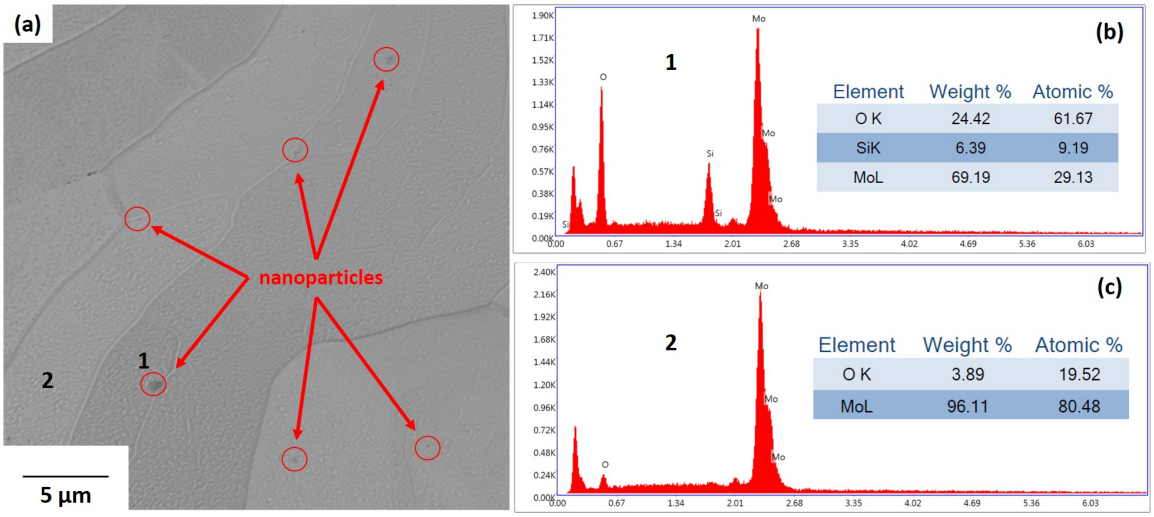

Figure 4.29. Bulk and point EDS analysis of the nanoparticles conducted via SEM. (a) Etched surface showing the presence of nanoparticle inclusions. (b) Nanoparticle EDS analysis result. (c) Bulk material EDS analysis result.

4.2.3 Mechanical Properties

Figure 4.30 shows the flexural strength of the pure molybdenum and Mo-0.1SiC specimens at the four scan speeds. The bars were tested in such a way that placed the load across the build direction so that cracks propagated along the columnar grains.

The strength of LPBF molybdenum was improved through the addition of nano-sized SiC. The flexural strength at a print speed of 400 mm/s was 242.8 ± 23.5 MPa for Mo-0.1SiC and 134.3 ± 12.7 MPa for pure molybdenum representing a roughly 80% increase. The strength varied with scan speed, increasing from 100 to 400 mm/s and decreasing again at 800 mm/s for the Mo-0.1SiC specimens.

Figure 4.31 shows the ductility as percent strain as determined during the flexural strength measurements. The ductility of the Mo-0.1SiC specimens are improved over the pure molybdenum at all scan speeds.

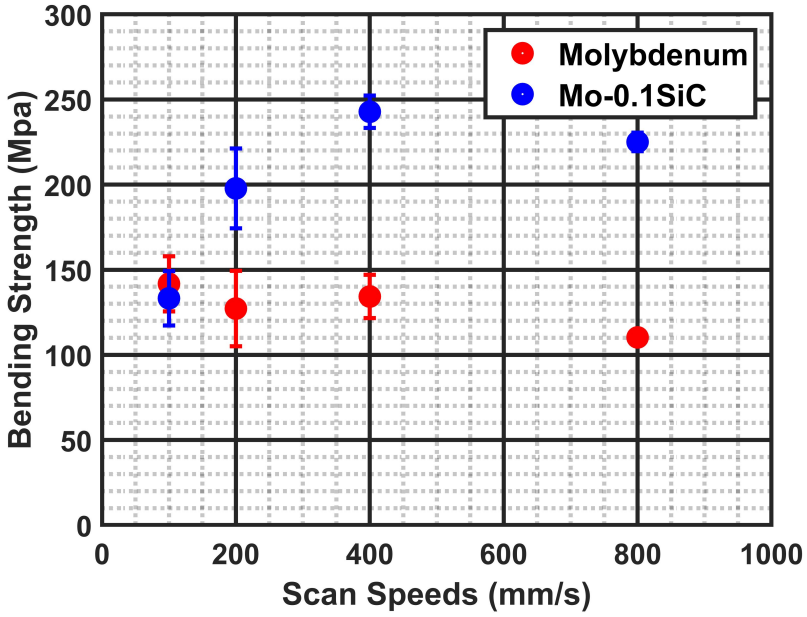

Figure 4.30. Flexural strength of the prepared pure molybdenum and Mo-0.1SiC specimens at the four different scan speeds. The error bars represent the standard deviation of the three measurements taken for each scan speed.

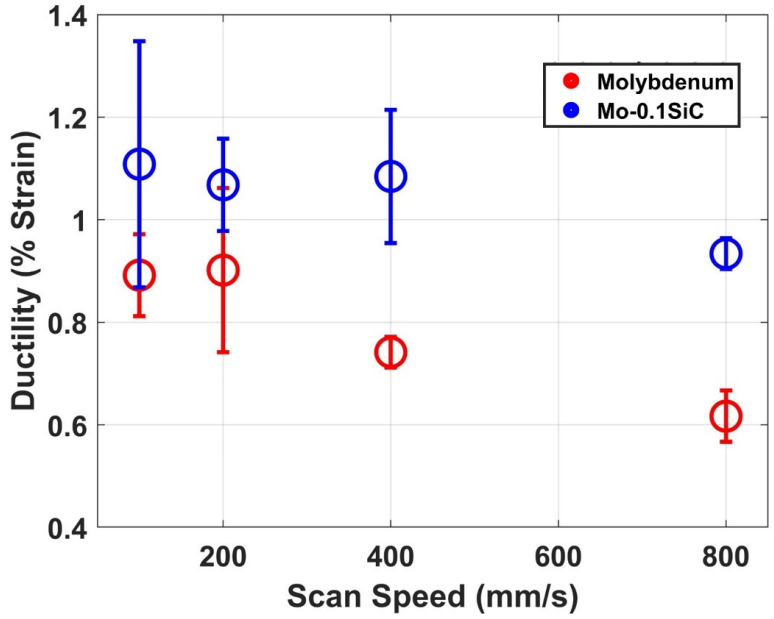

Figure 4.31. Ductility, as % strain, of the prepared pure molybdenum and Mo-0.1SiC specimens at the four different scan speeds. The error bars represent the standard deviation of the three measurements taken for each scan speed.

Figures 4.32 and 4.33 show the fracture surfaces of the pure molybdenum and Mo-0.1SiC specimens. The load applied to the cuboid specimens in the flexural strength measurements resulted in the fracture surfaces showing the grain boundaries of the material. In both cases the fracture surfaces were nearly devoid of transgranular fracture, and instead only show intergranular fracture. The surfaces of the pure molybdenum specimen showed many open volume defects, caused by a lack of fusion, where there was poor consolidation as well as unmelted particles that were not present in the Mo-0.1SiC specimen. Point EDS was performed on the secondary phase present on the surfaces and revealed only molybdenum and oxygen contained in the inclusions.

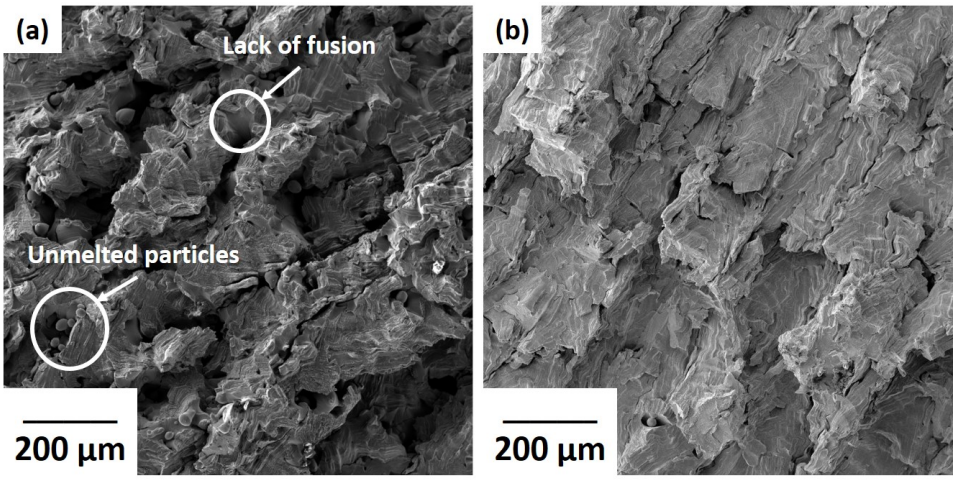

Figure 4.32. SEM images of fracture surfaces for (a) pure molybdenum and (b) Mo-0.1SiC printed at 400 mm/s.

The secondary phase inclusions in Figure 4.33 were present on all the fracture surfaces of pure molybdenum and Mo-0.1SiC alike, indicating that a prevention of oxygen segregation to the grain boundaries was not fully achieved at 0.1 wt% silicon carbide.

The Vickers hardness values for the pure molybdenum and Mo-0.1SiC specimens at all four scan speeds in Figure 4.34. The Mo-0.1SiC specimens had significantly higher hardness than the pure molybdenum specimens at higher scan speeds.

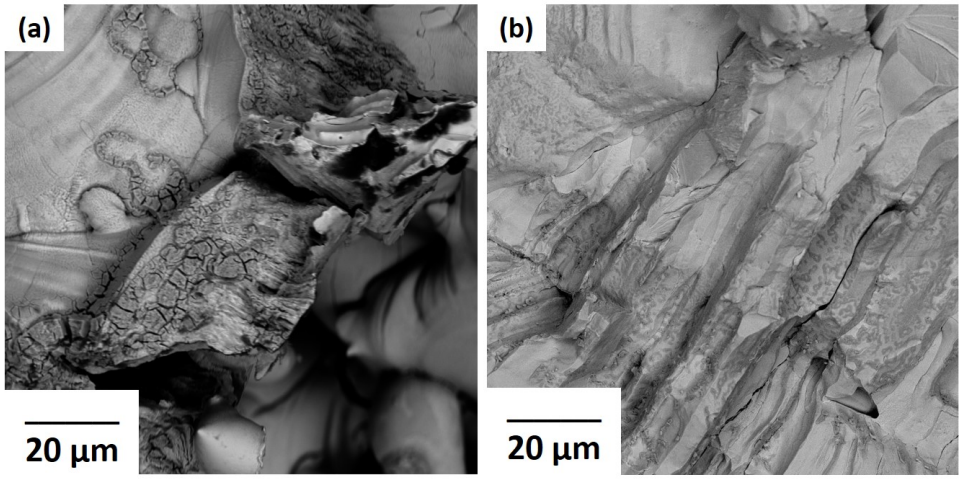

Figure 4.33. Magnified backscattered electron SEM images of fracture surfaces for (a) pure molybdenum and (b) Mo-0.1SiC printed at 200 and 800 mm/s, respectively.

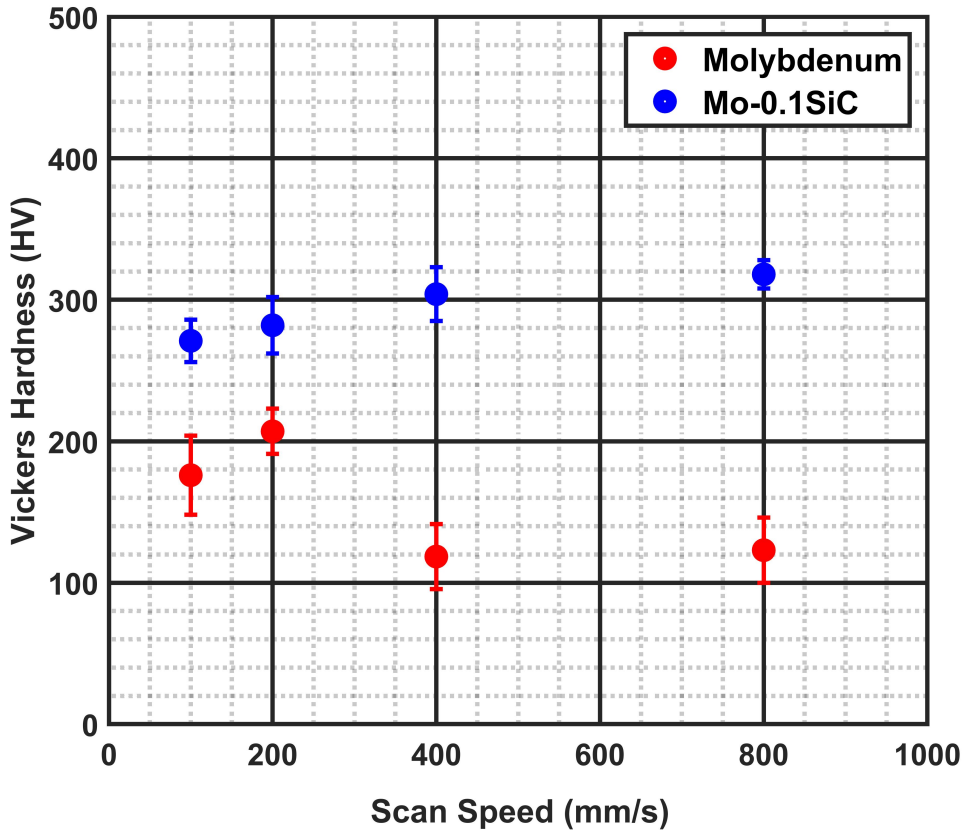

Figure 4.34. Vickers hardness values for pure molybdenum and Mo-0.1SiC at the four different scan speeds. The error bars represent the standard deviation of the forty individual indentations made on each specimen.

4.3 Discussion

When taken together, the experimental data outlined in the Section 4.2 indicate that the addition of nano-sized silicon carbide at 0.1wt% improved the consolidation, mechanical properties, and in-situ oxidation of LPBF molybdenum.

The images of pure molybdenum in Figure 4.8 demonstrate the impact of laser scanning speed on melt pool behavior. At increased scanning speeds the melt-pool temperature is decreased due to decreased energy input [147]. Insufficient energy input at lower VEDs resulted in the balling phenomenon seen in the pure molybdenum samples. Lowering the scanning speed increased energy input and caused improved wetting and spreading of the molybdenum melt pool which suppressed the balling effect. The viscosity of liquid molybdenum decreases as temperature increases, improving the flow of the melt pool, overlapping of weld tracks, and overall consolidation. The addition of nano-sized silicon carbide reduced the balling effect without an increase in energy input indicating better retention of input energy by the Mo-0.1SiC powder compared to the pure molybdenum. The effect of sub-optimal energy input was also observed in the Mo-0.1SiC specimens at higher scan speeds. It is postulated that addition of nano-sized SiC improved the coupling of the laser to the molybdenum powder through the scattering of the incident laser energy. As determined through the K-M analysis, the impact of scattering is about 25% greater in the Mo0.1SiC powder.

Figure 4.7 clearly shows increased reflectance in the Mo-0.1SiC powder, however the increased scattering effect results in increased coupling of the laser and powder system. Additional coupling increases temperature and longevity of the melt pool which improves the rheological properties of the liquid and produces samples with better surface quality and less porosity. Gu et al. [94] showed that the addition of titanium diboride and silicon carbide to copper and AlSi10Mg powders increased the

absorptivity at the 1064 nm wavelength of the laser used in that work which improved melting and consolidation. The melting temperature of copper and AlSi10Mg are significantly lower than that of molybdenum, but the results of the current study show that a dilute addition of nano-sized silicon carbide can have a similar effect on consolidation during LBPF.

The porosity values in Table 4.3 and porosity images in Figure 4.11 also indicate improved melting due to the addition of silicon carbide. It has been shown that variation in porosity is dependent on magnification and at higher porosity levels the variation increases [148]. For this reason, comparison to existing porosity reports can be difficult; however, the porosity values of the pure molybdenum specimens are roughly comparable to the measurements made by Faidel et al. [30] at similar VEDs. There is a significant reduction in porosity in the Mo-0.1SiC specimens. The porosity is lowest in the specimen printed at 400 mm/s and is generally lower at the higher scan speeds. Two mechanisms for pore formation in LPBF metals are evolution of gases from powder feedstock or trapping of build atmosphere gases. The likelihood of these mechanisms occurring increases with increasing VED. High VEDs also result in melt instability due to gas flow resulting in increased porosity. Porosity can be created at low VED due to incomplete melting of the powder [149], which is seen in the Mo-0.1SiC when printed at 800 mm/s. The fracture surface of pure molybdenum shown in Figure 4.32 illustrates the lack-of-fusion defects and bulk porosity resulting from insufficient energy input. Dilip et al. [150] showed an analogous trend to the porosity values of Mo-0.1SiC presented here, in selective laser melted Ti-6Al-4V. An ideal scanning speed that finds a balance between insufficient and excessive energy input is likely around 400 mm/s for the print parameters chosen in this study.

While the evidence points towards increased melt pool temperature with the addition of nano-sized silicon carbide, the scanning speed appeared to have a much larger

impact on the microstructural evolution. The average grain sizes on the top surface of the Mo-0.1SiC specimen printed at 100 mm/s is 47.33 ± 9.47 μm compared to 40.64 ± 7.51 μm for pure molybdenum at the same scanning speed. The average grain size of Mo-0.1SiC at 400 mm/s was much smaller at 25.52 ± 1.09 μm. The reduction in grain sizes due to scanning speed was evident in the longitudinal direction of the Mo-0.1SiC as the average grain sizes for the 100 and 400 mm/s specimens were 211.51 ± 29.13 μm and 58.40 ± 8.16 μm, respectively. The larger grain sizes seen in Mo-0.1SiC at lower scanning speeds are expected due to increased melt-pool temperature and reduced cooling rates allowing more time for grain growth to occur. The thermal behavior of the melt pool likely cannot be inferred from only the VED [151]; however, it is reasoned here, and elsewhere, that the increased effective energy input that is evidenced in the Mo-0.1SiC results in a smaller thermal gradient between the melt pool and the surrounding solid, reducing the cooling rate [152]. Generally the presence of secondary-phase nanoparticles, like those shown in Figure 4.29, act to pin grain boundaries or nucleate new grains to limit grain growth; however, the average grain sizes between molybdenum and Mo-0.1SiC are comparable. It is possible that the increased melt pool temperatures and reduced cooling rates induced an annealing effect that competed with the nanoparticle pinning mechanism to produce the comparable average grain sizes at the 100 mm/s scanning speed.

The presence of oxygen at the grain boundaries of laser printed refractory metals is detrimental to consolidation and mechanical properties. Controlling oxygen is of vital importance to reducing the crack propagation and increasing the mechanical performance of LPBF refractory metals. The addition of silicon carbide provided two mechanisms for limiting the presence of oxygen during printing. The oxidation of silicon carbide can progress by different mechanisms dictated by the presence of oxygen and temperature. Under a non-reactive (or vacuum) environment, like the

nitrogen shield gas used in this analysis, oxidation occurs through the vaporization of silicon into a silicon-rich phase that precipitates carbon. In an oxidizing environment, silicon carbide can undergo passive and active regimes of oxidation. At lower partial pressures of oxygen, silicon is oxidized to gaseous silicon monoxide and more volatile carbon monoxide. Under high partial pressures of oxygen, silicon carbide is oxidized to solid silicon dioxide and gaseous carbon monoxide [153, 154]. It is likely that under the high temperatures, low oxygen, and non-equilibrium conditions of LPBF some combination of mechanisms was taking place. In all three scenarios, free carbon is produced to react with the limited oxygen present in the system, thereby improving oxygen capture. The silicon and oxygen containing nanoparticles indicate that not all of the volatilized silicon escaped from the consolidated material. The formation of nanoparticles instead suggests that the silicon became mobile at the high temperatures and sequestered oxygen. The movement of the laser resulted in rapid cooling of the melt and the silicon oxides became trapped in the bulk of the material, limiting the ability of oxygen to embrittle the grain boundaries. While the formation of secondary phase nanoparticles indicate that oxygen was captured by the silicon, the fracture surfaces, in Figure 4.33, demonstrate that the 0.1 wt% silicon carbide added was insufficient to prevent the formation of detrimental molybdenum oxides.

The flexural strength of Mo-0.1SiC was less than that of pure molybdenum at 100 mm/s, but increased to almost double at 400 mm/s. Interestingly, the grain sizes are most disparate between the pure molybdenum and Mo-0.1SiC specimens at the 100 mm/s scan speed and converge in both the transverse and longitudinal orientations at the 400 and 800 mm/s scan speeds. The grain size is therefore primarily influential between the pure molybdenum and Mo-0.1SiC specimens only at the 100 mm/s where consolidation was best achieved. Dispersion strengthening due to the secondary phase could contribute to the increase in strength in the Mo-0.1SiC specimens, but this

is difficult to confirm to due to the poor consolidation of the pure molybdenum specimens. The Hall-Petch relationship indicates that strength should increase as grain size decreases, and thus, without regard to other factors, an inverse relationship between grain size and strength should exist. As demonstrated in Figure 4.35, this is not exhibited by the pure molybdenum specimens indicating that the disparity in flexural strength between the pure molybdenum and Mo-0.1SiC specimens were, at least in part, due to the lack-of-fusion experienced at the higher scan speeds.

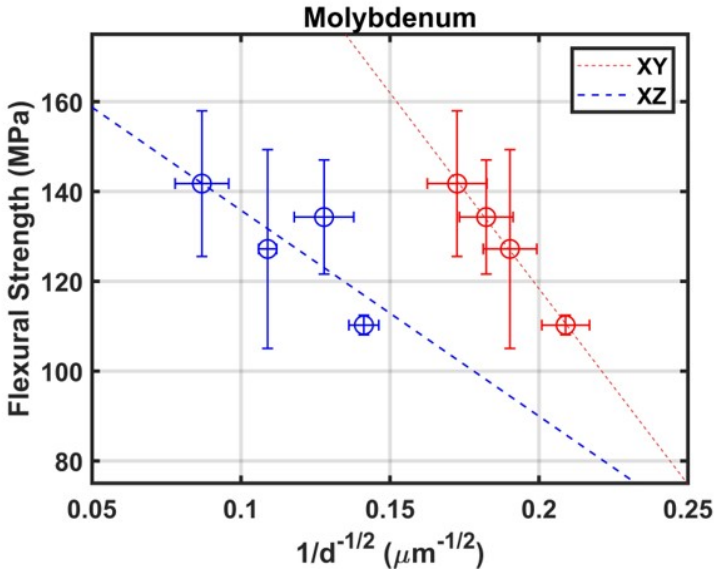

Figure 4.35. Plot of the relationship between the transverse and longitudinal grain size and flexural strength for the pure molybdenum specimens.

As shown in Figure 4.36, the flexural strength of the Mo-0.1SiC specimens is inversely related to the grain size, following the Hall-Petch relationship. At the 800 mm/s scan speed, the strength unexpectedly decreases. The powder system was subjected to insufficient energy input and poor consolidation became the governing factor behind flexural strength. The secondary phase nanoparticles present in the Mo-0.1SiC specimens inherently provide a strengthening effect as pinning locations that impede dislocation motion and raise the activation energy for slip. The analysis of the microstructure provided by the electron microscopy techniques presented in this

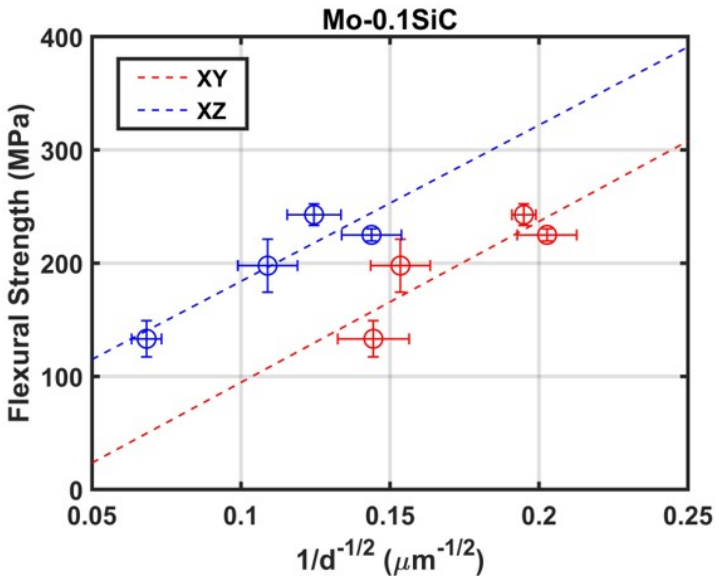

Figure 4.36. Plot of the relationship between the transverse and longitudinal grain size and flexural strength for the Mo-0.1SiC specimens.

chapter do not indicate whether the prevalence of the secondary phase increases with scan speed, so the majority of the strengthening effect is understood to be governed by either the grain size or or overall consolidation of the specimen.

Ductility of the Mo-0.1SiC specimens was improved, specifically at the higher scan speeds, but this is likely due to improved consolidation. All fracture surfaces exhibited purely intergranular fracture.

As expected, the hardness of Mo-0.1SiC was vastly increased over that of pure molybdenum due to the presence of the secondary-phase nanoparticles. The pure molybdenum printed at 200 mm/s had a comparable Vickers hardness of 207 ± 16 HV0.5 as reported elsewhere with LPBF molybdenum at similar energy inputs [32]. The maximum hardness found in the Mo-0.1SiC was 318 ± 10 HV0.5 in the specimen printed at 800 mm/s. Silicon oxide nanoparticles have been shown to increase hardness in other materials and improve wear resistance [155]. The increase in both strength and hardness are due to the nanoparticles blocking dislocation movement and preventing the propagation of cracks. The Hall-Petch relationship predicts an

increase in hardness as grain size decreases. Given that the grain sizes in Mo-0.1SiC decrease with an increase in scan speed, the increase in measured hardness is explained. The absence of a similar trend in the molybdenum hardness was likely due to the extensive porosity.

4.4 Conclusions

The addition of 0.1 wt% silicon carbide improved the consolidation, mechanical properties and in-situ oxidation of molybdenum through LPBF and the subsequent analysis has yielded the following conclusions:

1. The addition of silicon carbide improved melting indicating increased laser energy absorption of the powder system.

2. Chemical analysis shows that in-situ oxidation of molybdenum powder was reduced in the powder system by 60% at the 200 mm/s scan speed by the addition of silicon carbide.

3. Cross-sectional porosity in the Mo-0.1SiC was reduced by as much as 92% at the 400 mm/s scan speed as compared to pure molybdenum.

4. The formation of secondary-phase nanoparticles and oxidation of silicon carbide provided two mechanisms for reducing the effect of oxygen on the consolidated molybdenum material.

5. The flexural strength and hardness of LPBF molybdenum increased by 80% and 60%, respectively, due to the improved consolidation and reduced lack-of-fusion defects. The strengthening mechanism switch to grain boundary strengthening with the addition of silicon carbide.

V. Positron Annihilation Spectroscopy

Positron methods have been successfully used to investigate microstructural behavior during the heat treatments of defected and damaged metals since the method was first proposed in the 1960s [156]; however, there have been very few reports in the literature of studies on metals produced through AM techniques. This chapter addresses the research objectives in Problem Statements 2 and 3. Positron lifetimes and Doppler-broadening spectra were collected for the pure molybdenum and Mo-0.1SiC specimens printed at all four scan speeds: 100, 200, 400, and 800 mm/s. Initial measurements were conducted such that the transverse (print) surfaces of the specimens were exposed to the positrons. Follow-on measurements exposed the longitudinal (build direction) surfaces of only the pure molybdenum specimens to the positrons. The contents of this chapter, in part, have been published as an original research article in the MDPI journal *Materials*, which is an open-access journal with a 2021 Impact Factor of 3.748 per *Journal Citation Reports* by Clarivate [142]. *Materials* covers a broad range of topics across all classes of materials along with characterization techniques. The article was published on February 15, 2023, and has the following DOI:

DOI: 10.3390/ma16041636 [157]

Further data and analyses have been added to the contents presented in the journal article as all of the DBAR data and analysis and the positron lifetime analysis of the longitudinal surface of pure molybdenum was conducted after the article was originally drafted and submitted for publication. The analysis in this chapter directly focuses on the research objectives under Problem Statements 2 and 3 presented in Chapter 1, and indirectly supports Problem Statement 1. The objectives of Problem Statements 2 and 3 were addressed by comparing the positron lifetime spectra to the microstructural and mechanical data discussed in Chapter 4. Grain sizes and

the observed grain boundary misorientation do not correlate with positron lifetimes and associated intensities, indicating the positrons are sampling regions within the grains. PALS results identified the presence of dislocations and microvoids not revealed through electron microscopy techniques and correlated with the findings of SiO_2 nanoparticles in the samples prepared with silicon carbide. This comparison of results indicated the usefulness of positron techniques to characterize nano-structure in AM metals due to the significant increase in atomic-level information.

5.1 Materials and Methods

5.1.1 Specimen Preparation

The pure molybdenum and Mo-0.1SiC specimens used in this study were consolidated in the same manner as those used for initial microstructural characterization as described in Chapter 4. One cylindrical specimen, 15 mm in diameter and 5 mm thick, was produced for each laser scan speed of 100, 200, 400, and 800 mm/s. All cylindrical specimens were printed on copper substrates with a 0.5 mm offset at an initial scan speed of 800 mm/s. This offset was removed when the specimens were separated from the substrate using wire-cut EDM. EDM was also used to section the cylindrical specimens into two pieces to produce two identical cross-sectional surfaces, each with a thickness of roughly 2 mm at each scan speed. The cross-sectional surfaces on these cylindrical specimens were representative of the transverse direction. Cuboidal specimens with dimensions 12 mm x 12 mm x 12 mm were produced for the pure molybdenum at each scan speed and sectioned in half so that the cross-sectional surfaces were representative of the longitudinal, or build, direction. Surfaces of all the samples were ground and polished to 800 grit using silicon carbide grinding paper using an EcoMet 300 grinding and polishing machine (Buehler, Lake Bluff, IL, USA). The transverse specimens, as-built, were 5 mm in height. After sectioning, each piece

was about 2.5 mm thick. Due to the positioning of the positron in the source, they were likely entering the material in the middle of the cylinder at a depth roughly 2.5 mm below the as-built surface. The longitudinal specimens, as-built, were 12 mm in height. These were sectioned along this direction so that the build surface was available for placement against the positron source. The positrons likely entered this material roughly 6 mm below the as-built surface. These depths are sufficient to be considered bulk measurements. The decision to evaluate the longitudinal surface of the pure molybdenum specimens was made well after the original specimens were produced. By this time, additional Mo-0.1SiC powder was unavailable, so study on these specimens was not accomplished.

5.1.2 Positron Annihilation Lifetime Spectroscopy

The digital positron annihilation spectrometer used for the positron lifetime measurements includes six BaF_2 fast scintillation detectors, coupled to fast photomultiplier tubes (Hamamastu R3377, Shizuoka, Japan) whose output was digitized using a 5GSs digitizer (CAEN VX1742, Viagreggio, Italy). Its timing resolution is about 204 ps (FWHM).

The positron source was titanium foil-encapsulated ^{22}Na crystallites (A2305-2, POSN configuration, Eckert and Ziegler) with an activity of 10.1 μCi. The source is constructed so the ^{22}Na is sealed between two titanium foils, 5.1 μm in thickness and supported by two 0.25 mm thick titanium disks. The whole source is 19.1 mm in diameter while the active area has a 9.53 mm diameter.

Positron measurements were conducted by sandwiching the titanium-sealed positron source between two, nominally identical specimens. The source-sample sandwich was held together with tape and suspended between the detectors with aluminum wire. All lifetime spectra of with total counts more than 10^7 were deconvoluted using the

PALSfit3 software package [122] after appropriate background and source contribution corrections as discussed in Section 3.5.

Initial PALS measurements were conducted on the pressed and rolled molybdenum standard whose microstructural is shown in Figure 2.5. Analysis of the lifetime spectrum for the molybdenum standard yielded a single lifetime of 136.6 ± 0.1 ps. The reduced-χ^2 for this fit was 1.034. The expected lifetime of bulk (defect-free) molybdenum is around 120 ps [139, 138], however untreated molybdenum has been shown to have a first component lifetime around 140 ps [141]. This lifetime between 130-140 ps, which is higher than the bulk lifetime, but lower than the monovacancy lifetime has been attributed to annihilations at dislocations and their intersections [140]. Staab et al. [158] showed that Monte Carlo simulations indicate a measurable percentage (1-3%) of annihilations occur at the grain boundaries for materials with grain sizes less than 15 μm. The grain sizes of the molybdenum standard were measured as 4.66 $\pm$0.28μm, but a lifetime around 400 ps that would be associated with grain boundaries [141] was not found during the lifetime spectrum analysis.

5.1.3 Doppler-Broadening of Annihilation Radiation

DBAR measurements were conducted using an ORTEC high-purity germanium detector with a resolution for the energy of the 1333 keV (FWHM) of 2.1 keV, and a DSA 1000 MCA. Data was processed using the Genie 2000 Spectroscopy Software, version 3.1 [159]. The analysis of the data consisted of calculating the S and W parameters. The S parameter is defined as the ratio of the counts in the central area of the annihilation line (510.3 and 511.7 keV) to the total counts in the annihilation region (505 to 517 keV). The W parameter is defined as the ratio of the counts in the wing area of the annihilation line (514 to 516 keV) to the total counts in the annihilation region [114]. The DSA-1000 was configured to produce 8190 channels

which is the maximum number available [160]. Through analysis of the spectra it became clear that sub-channel calibration of the detector was necessary. Each spectra was calibrated using the channel location of the 511 and 1274 peaks. In order to determine the exact location, MATLAB and the associated curve fitting tool were used to fit Gaussian functions to each peak. The centroids were determined and a linear calibration between the 511 and 1274 channels was performed. The channels in the regions containing the 511 and 1274 keV peaks were interpolated so that the original number of channels in the peak was multiplied by 1000. This allowed for sub-channel identification of the centroid and a calibration with more fidelity.

5.2 Results

5.2.1 Doppler-Broadening of Annihilation Radiation

The positron annihilation line energy spectra were collected for the Mo-0.1SiC specimens and the pure molybdenum specimens in the longitudinal and transverse directions. As discussed in Section 3.6, broadening of the annihilation line occurs due to interactions with core electrons. The number of interactions generally increases with atomic number as electrons and electron-shells are added. As mentioned, comparing DBAR results across different published reports is difficult because the absolute momentum broadening spectra are unique to the experimental setup and these particulars differ.

During the course of the year-long measurements, the HPGe detector resolution drifted. This resolution was measured at the 1274 keV peak for all collected spectra. The measured FWHM for all of the collected spectra are shown as a histogram in Figure 5.1. There are significant differences in the detector's resolution over the measurements conducted, however there is not a temporal correlation. The drift is likely due to the radio frequency interference noise associated with the location where

the measurements were conducted.

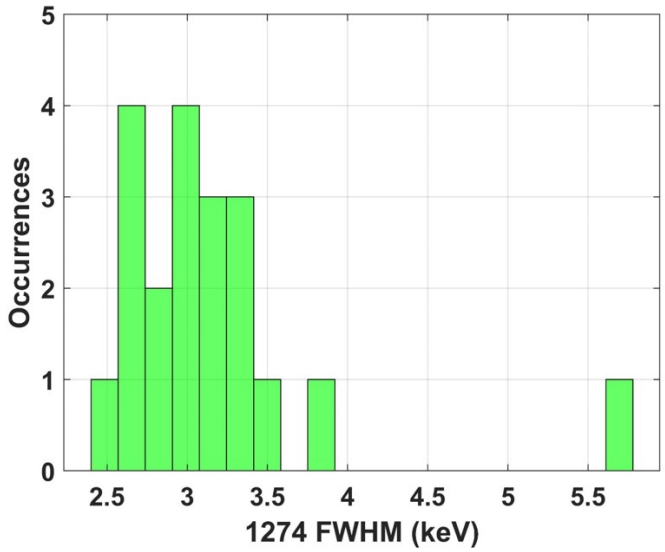

Figure 5.1. Histogram displaying the measured FWHM at the 1274 keV peak for all the spectra collected on the HPGe detector used during this research.

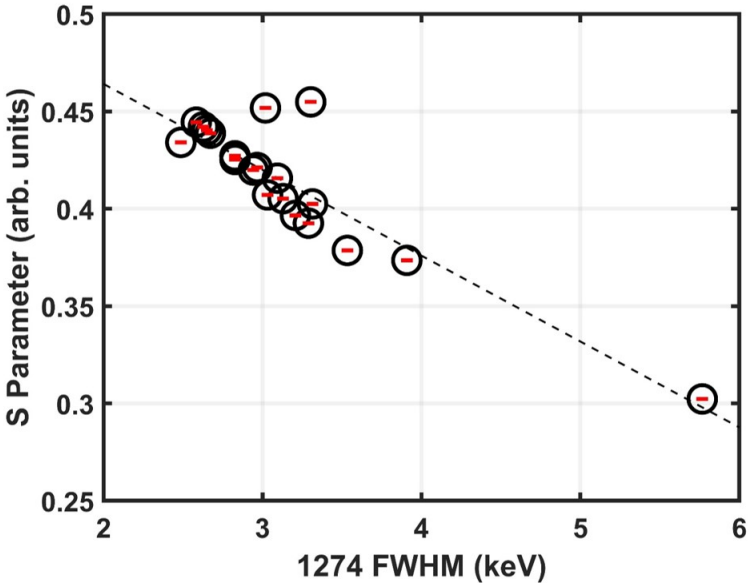

Figure 5.2. Comparison of calculated S parameters and the FWHM of the 1274 peak.

The S parameters determined from all the spectra collected during this research are plotted against the FWHM of the 1274 keV peak in Figure 5.2. The linearity of the S parameters offers the potential for correction, however there is enough variation

to question whether all of the differences are due to the FWHM, or if the specific material under test has any influence. As the only sample that was measured in replicate was the single crystal copper, as described in Chapter 3, it is unclear if different materials will fall along the same line. As such, the current spectra are incomparable due to detector resolution variability.

5.2.2 Positron Annihilation Lifetime Spectroscopy

All positron lifetime measurements collected for the molybdenum and Mo-0.1SiC specimens yielded complex lifetime spectra that required at least two components to provide optimal fits. Initial guesses of lifetime parameters were chosen as 115 ps and 170 ps, representing the characteristic experimental lifetimes of the bulk and defect free regions in molybdenum. The results from the initial deconvolution of the PALS spectra are shown below in Tables 5.1, 5.2, and 5.3. After removal of a constant background and determined source contribution as discussed in Section 3.5.4, the initial analysis employed two unconstrained lifetime fitting parameters.

Table 5.1. Results of deconvolution using two unconstrained lifetime fitting parameters for LPBF molybdenum in the transverse direction with reduced χ^2 values.

Scan Speed (mm/s)	τ_1 (ps)	τ_2 (ps)	I_1 (%)	I_2 (%)	reducedχ^2
100	125.2 ±0.1	751.5 ±32.6	99.66 ±0.02	0.34 ±0.02	1.068
200	128.8 ±0.2	583.6 ±13.8	99.07 ±0.04	0.93 ±0.04	1.083
400	129.7 ±0.2	430.7 ±8.3	98.02 ±0.09	1.97 ±0.09	1.052
800	128.7 ±0.2	462.9 ±11.4	98.69 ±0.07	1.31 ±0.07	1.000

Table 5.2. Results of deconvolution using two unconstrained lifetime fitting parameters for LPBF molybdenum in the longitudinal direction with reduced χ^2 values.

Scan Speed (mm/s)	τ_1 (ps)	τ_2 (ps)	I_1 (%)	I_2 (%)	reduced-χ^2
100	127.7 ±0.1	851.2 ±40.9	99.74 ±0.02	0.26 ±0.02	1.069
200	131.6 ±0.1	863.3 ±14.5	99.22 ±0.02	0.78 ±0.02	1.172
400	130.1 ±0.2	597.3 ±13.5	99.13 ±0.04	0.87 ±0.04	1.108
800	134.1 ±0.2	536.2 ±14.6	99.07 ±0.05	0.93 ±0.05	1.124

Table 5.3. Results of deconvolution using two unconstrained lifetime fitting parameters for LPBF Mo-0.1SiC in the transverse direction with reduced χ^2 values.

Scan Speed (mm/s)	τ_1 (ps)	τ_2 (ps)	I_1 (%)	I_2 (%)	reduced-χ^2
100	135.2 ±0.3	415.0 ±2.7	92.47 ±0.12	7.53 ±0.12	1.114
200	136.8 ±0.3	384.8 ±4.1	94.66 ±0.15	5.34 ±0.15	1.112
400	138.2 ±0.3	368.9 ±5.6	95.87 ±0.17	4.13 ±0.17	1.043
800	141.2 ±0.3	409.3 ±7.3	97.22 ±0.12	2.78 ±0.12	1.069

The lifetime of the second component found in the longitudinal direction is significantly higher than the lifetime of the second component in the transverse direction at comparable scan speeds. As discussed in Section 3.4, positronium can form in regions of open volume or along free surfaces. There was a long lifetime component (745.1 ps) removed due to the source contribution analysis, however this does not fully account for the positron lifetimes found in the LPBF specimens. The copper and molybdenum standards measured do not have open porosity where positronium may be likely to form and therefore this component was not corrected for with in the initial source contribution analysis. Neither the τ_2 lifetimes or intensities correlate with the porosity values in Table 4.3, and it is likely that the second component is a combination of lifetimes that includes positronium and voids. Generally only lifetimes above about 500 ps [107] are considered to be due to the presence of positronium. The transverse molybdenum samples at the 400 and 800 mm/s have a τ_2 component that, while still a combination of lifetimes, is now being dominated by a microstructural feature, such as voids or vacancy clusters, that are a bulk process. The formation and annihilation of positronium is not considered to be a bulk process in this case and will therefore be removed by constraining lifetime parameters during subsequent analyses.

The τ_1 and τ_2 components are reduced in the Mo-0.1SiC specimens compared to the similarly orientated transverse molybdenum specimens. Generally, it appears that the Mo-0.1SiC specimens are more defected as the τ_1 component has an intensity significantly less than that of the τ_1 component in the molybdenum specimens. Additionally I_2, corresponding to the second lifetime component, is more prevalent. All of the Mo-0.1SiC specimens have a τ_2 lifetime that is being dominated by bulk microstructural features. While the open porosity of the Mo-0.1SiC is considerably less than that of the pure molybdenum, the lifetimes and intensities in the Mo-0.1SiC, like those in molybdenum, do not correlate with the values in Table 4.3. Further anal-

ysis using experimentally determined constraints for lifetimes found in molybdenum is warranted to refine the data interpretation.

In a defect-free solid, positron annihilations are characterized by a single lifetime [107]. When trapping sites are available, differences in annihilation rates due to variations in electron density result in a range of lifetimes corresponding specifically to the type of trapping site where they occur [107]. Previous PAS studies of molybdenum have yielded the lifetimes gathered in Table 5.4. Included in this table is the positron lifetime for silicon dioxide (SiO_2) due to the presence of silicon and oxygen containing, secondary-phase nanoparticles in the Mo-0.1SiC specimens.

Table 5.4. Experimentally determined characteristic lifetimes for trapping sites found in molybdenum, with associated references from the literature.

Trapping Site	Positron Lifetime (ps)	Reference
Single Crystal	103	Ziegler and Schaefer [161]
Bulk	115	Hyodo et. al [137]
Dislocations	135	Dryzek and Wróbel [141, 140]
Monovacancy	170	Robles et. al [121]
Divacancy	~ 249	Dryzek and Wróbel, Hautojärvi et. al [140, 162]
SiO_2	~ 261	Kuriplach and Barbiellini [163]
Microvoids	350 - 450	Hautojärvi et. al [162]

The range of lifetimes associated with microvoids is due to the lifetime of positrons in a condensed material correlating with the size of the void in which they annihilate. The larger the void, the longer the associated lifetime [116]. The 350 to 450 ps range corresponds to microvoids that contain 5-15 vacancies [162].

The lifetimes determined in the unconstrained analysis do not necessarily match any of the known lifetimes of positrons found in molybdenum. It is likely that the unconstrained analysis yielded lifetimes that remain convolutions of multiple lifetimes. Attempting an unconstrained analysis with additional lifetime parameters was unsuccessful. Due to this, an iterative approach that involved constraining different combinations of the lifetimes presented in Table 5.4 was adopted. Due to the sus-

pected positronium formation a long lifetime of 1 ns, that might be associated with this occurrence, was constrained. In addition to this, the constrained parameters chosen for the molybdenum specimens were the 115, 135, and 430 ps corresponding to the bulk, dislocation, and microvoid trapping sites, respectively. The τ_1 component in the unconstrained fit for Mo-0.1SiC was around the dislocation lifetime and through the iterative process it was clear that the shorter lifetime found in the molybdenum specimens was not present. With the presence of the silicon-oxide nanoparticles in mind, the constrained parameters for the Mo-0.1SiC specimens were the 135, 261, and 430 ps corresponding to the dislocation, SiO_2, and microvoids, respectively. The intensities corresponding to these constrained lifetime parameters are shown in Tables 5.5, 5.6, and 5.7, with associated reduced-χ^2 values. It should be noted that while the reduced-χ^2 values for certain spectra increased, the constrained fits are statistically consistent with those for the unconstrained fits and are less than 1.2.

Table 5.5. Results of deconvolution using four constrained lifetime fitting parameters (115 ps, 135 ps, 430 ps, and 1ns) for LPBF molybdenum in the transverse direction with reduced-χ^2 values.

Speed (mm/s)	I_1 (%)	$\mathbf{I_2}$ (%)	$\mathbf{I_3}$ (%)	$\mathbf{I_4}$ (%)	**reduced-χ^2**
100	50.51 ±0.76	49.19 ±0.79	0.10 ±0.05	0.20 ±0.01	1.109
200	33.71 ±0.81	65.20 ±0.84	0.88 ±0.05	0.21 ±0.02	1.083
400	26.01 ±0.81	72.15 ±0.84	1.80 ±0.05	0.35 ±0.01	1.057
800	32.58 ±0.80	66.13 ±0.82	1.22 ±0.04	0.70 ±0.01	1.007

Table 5.6. Results of deconvolution using four constrained lifetime fitting parameters (115 ps, 135 ps, 430 ps, and 1 ns) for LPBF molybdenum in the longitudinal direction with reduced-χ^2 values.

Speed (mm/s)	I_1 (%)	$\mathbf{I_2}$ (%)	$\mathbf{I_3}$ (%)	$\mathbf{I_4}$ (%)	**reduced-χ^2**
100	37.94 ±0.77	61.85 ±0.80	0.01 ±0.05	0.20 ±0.01	1.090
200	21.78 ±0.78	77.14 ±0.81	0.56 ±0.05	0.52 ±0.01	1.126
400	27.63 ±0.77	71.31 ±0.81	0.84 ±0.05	0.22 ±0.01	1.069
800	5.75 ±0.84	93.13 ±0.87	0.98 ±0.05	0.14 ±0.01	1.105

Figures 5.3, 5.4 and 5.5 corresponding to the data shown in Tables 5.1, 5.2, and 5.3, respectively, show the intensities of the fixed components. The fourth component

Table 5.7. Results of deconvolution using four constrained lifetime fitting parameters (135 ps, 261 ps, 430 ps, and 1 ns) for LPBF Mo-0.1SiC in the transverse direction with reduced-χ^2 values.

Speed (mm/s)	I_1 (%)	$\mathbf{I}_2$ (%)	$\mathbf{I}_3$ (%)	$\mathbf{I}_4$ (%)	**reduced-χ^2**
100	91.35 ±0.13	2.72 ±0.22	5.76 ±0.12	0.18 ±0.02	1.100
200	92.22 ±0.13	4.99 ±0.21	2.66 ±0.11	0.13 ±0.02	1.086
400	92.45 ±0.12	6.27 ±0.21	1.14 ±0.11	0.14 ±0.02	1.025
800	91.60 ±0.12	8.01 ±0.21	0.14 ±0.11	0.26 ±0.02	1.074

associated with the annihilation of positronium on the surface of the open-volume pores is omitted because it is not considered a bulk effect.

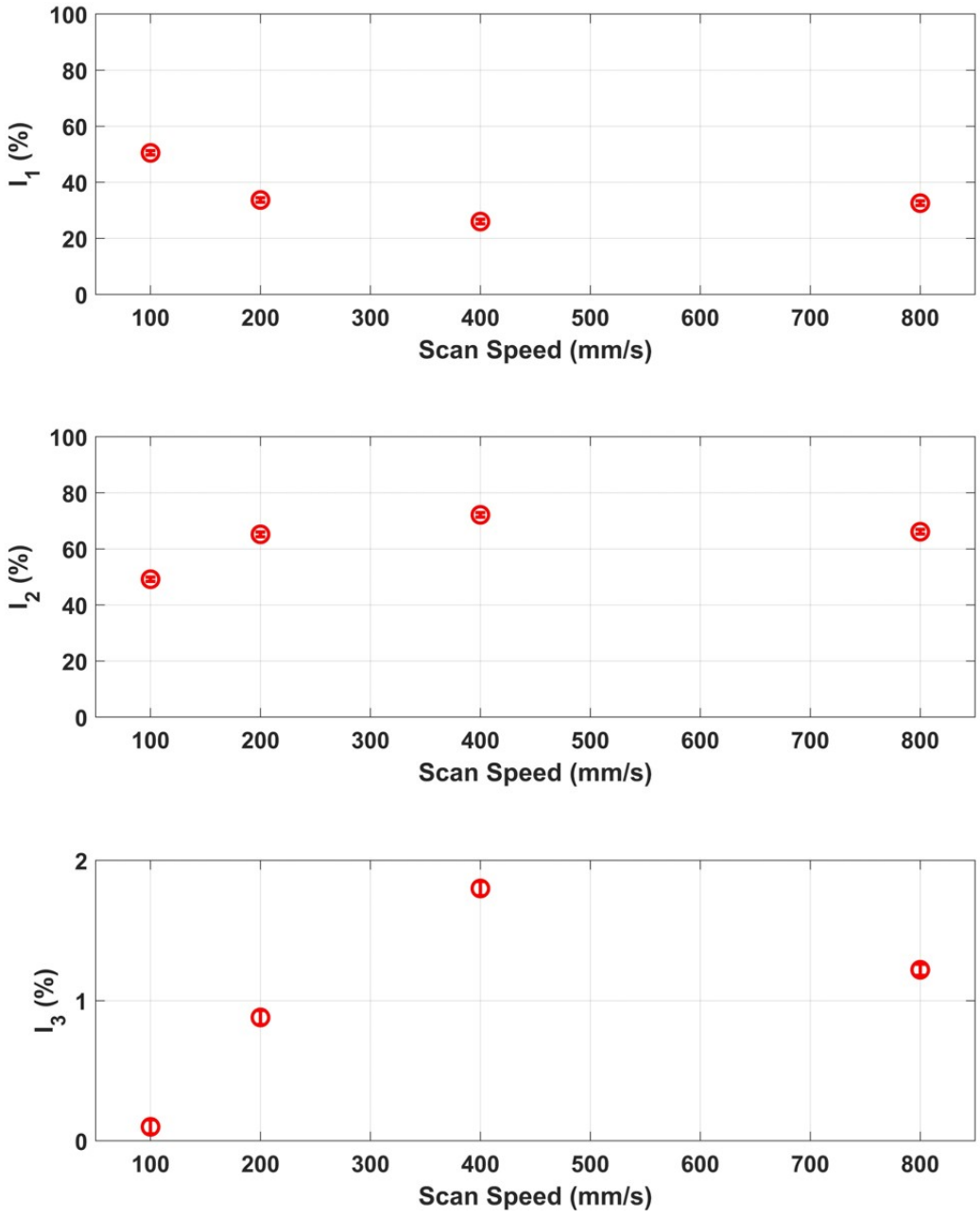

Figure 5.3. Constrained fitting for LPBF molybdenum in the transverse orientation. The I_1, I_2, and I_3 correspond to the three fixed lifetime components: 115, 135, and 430 ps, respectively.

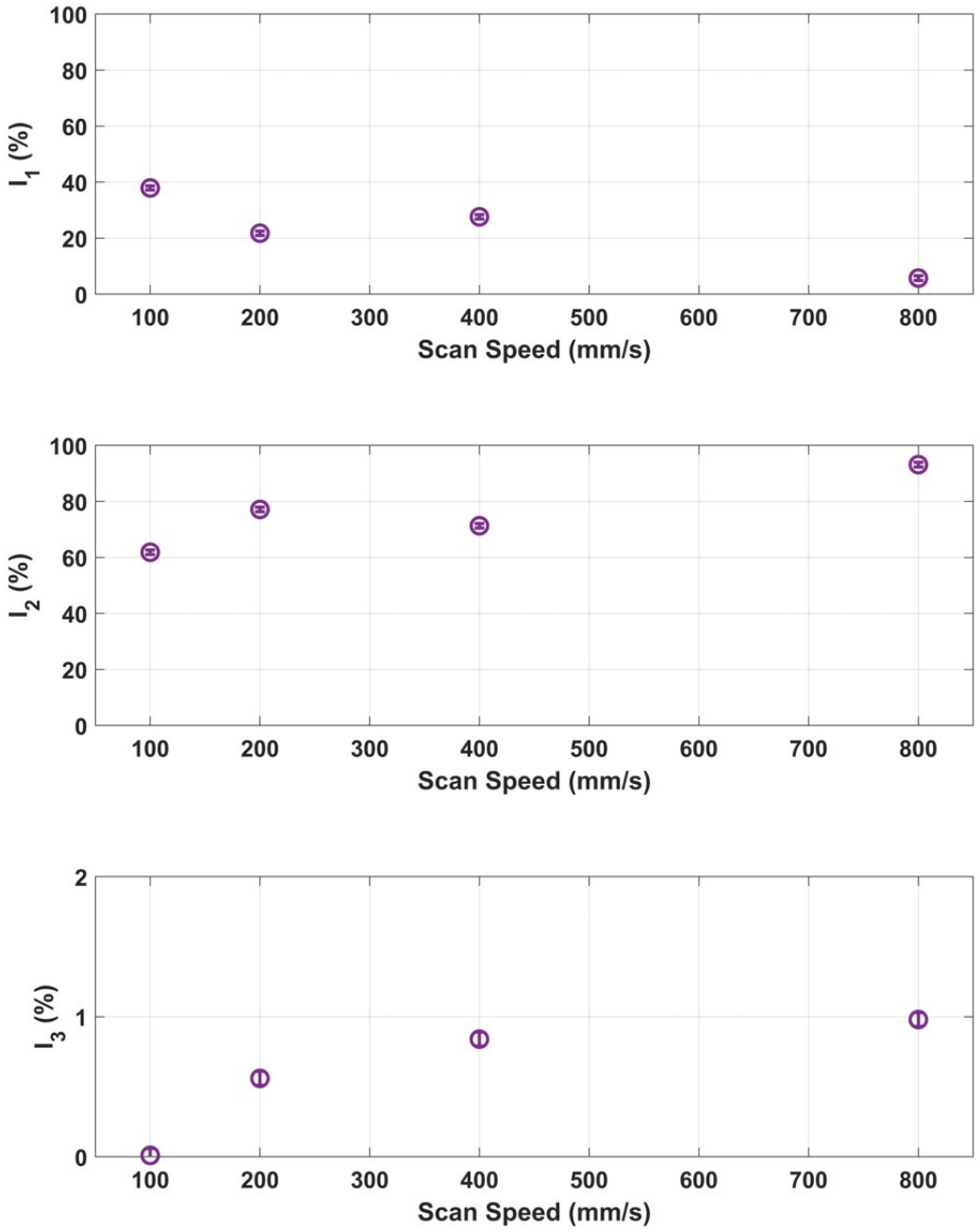

Figure 5.4. Constrained fitting for LPBF molybdenum in the longitudinal orientation. The I_1, I_2, and I_3 correspond to the three fixed lifetime components: 115, 135, and 430 ps, respectively.

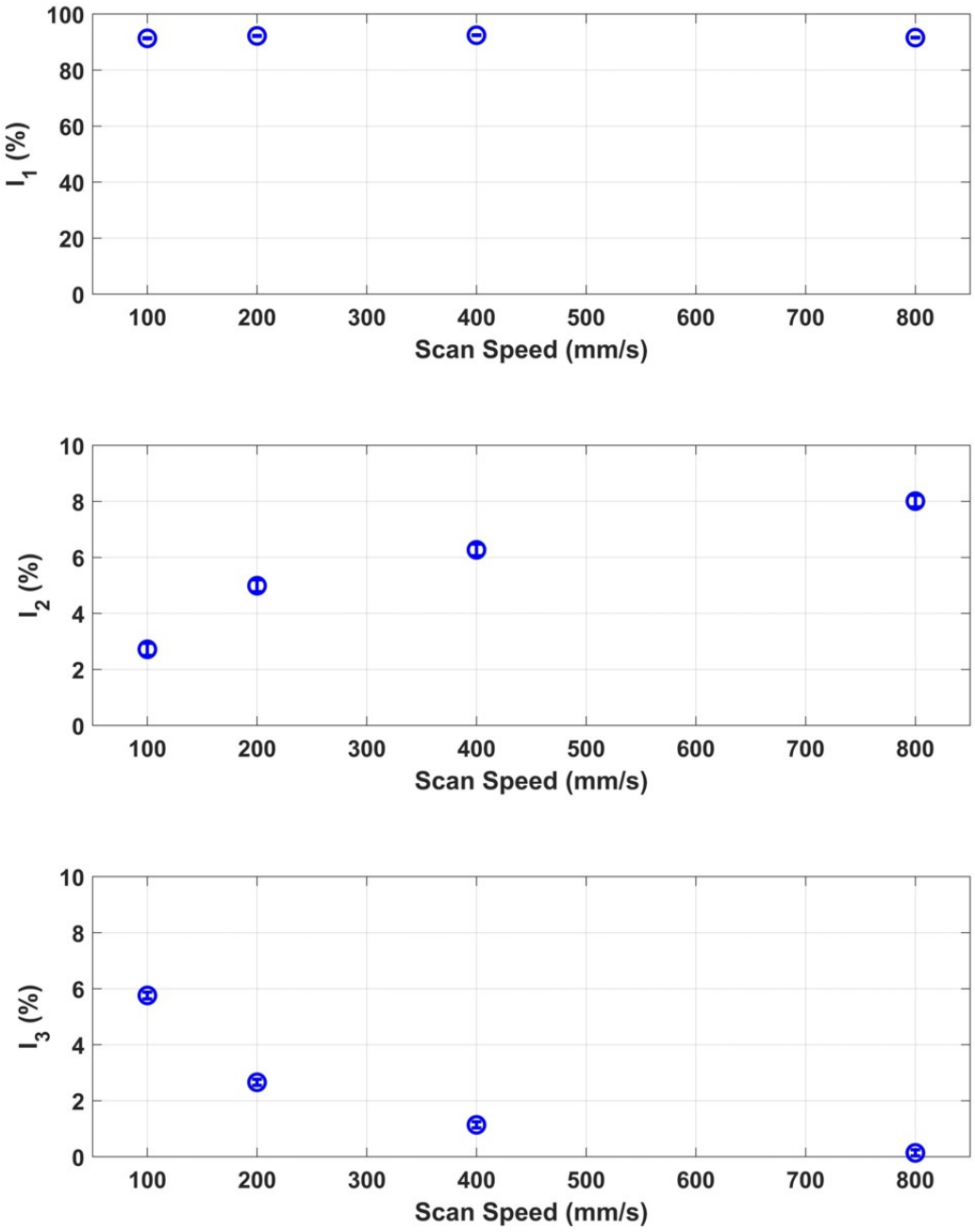

Figure 5.5. Constrained fitting for LPBF Mo-0.1SiC in the transverse orientation. The intensities correspond to the three fixed lifetime components: 135, 261, and 430 ps.

In the pure molybdenum transverse specimens, after the first scan speed at 100 mm/s, the intensity of τ_1, the defect-free component, drops between 15-20%. Correspondingly the intensity of τ_2, which corresponds to jogs or intersections of dislocations increases by the roughly the same amount. The third component, τ_3, intensity only increases to greater than 1.0% for the 400 and 800 mm/s scan speeds. This, along with the unconstrained analysis suggests that microvoids in the pure molybdenum specimens only start to appear at the faster scan speeds.

A similar trend is seen in the longitudinal specimens, however τ_1 is suppressed and τ_2 is enhanced at all scan speeds other than 400 mm/s where the values are consistent. The τ_3 component in the longitudinal specimens increase with scan speed but are not as prevalent as what is seen in the transverse direction. Interestingly, the consistent intensities in both directions at the 400 mm/s scan speed would indicate a similar abundance of defect trapping sites associated with these annihilation rates are being observed, whereas at the other scan speeds this is not the case. As with the transverse specimens, a monotonic trend with scan speed is not observed.

It was clear from the unconstrained analysis that the shorter lifetime exhibited by in the molybdenum specimens wasn't present in the Mo-0.1SiC, and indeed it appears that the 135 ps lifetime is predominant at a stable intensity of about 92% across the four scan speeds. In this fitting procedure τ_2 is 261 ps and represents the presence of SiO_2. The intensity of τ_2 increases by about 6.5% from the print conducted at 100 mm/s to that at 800 mm/s. The microvoid component, τ_3, has an intensity at the 100 mm/s scan speed that is significantly higher than any found in the pure molybdenum specimens. This decreases monotonically with increasing scan speed and is essentially nonexistent in the specimen printed at 800 mm/s.

5.3 Discussion

As previously mentioned, the positron lifetime measurements for the all of the LPBF specimens yielded complex lifetime spectra. The occurrence of multiple lifetime components is a result of numerous trapping processes present in the material. The microstructure of LPBF materials is often complicated by the conditions at which the materials are consolidated. While microscopy techniques like SEM, TEM, EBSD, and EDS, provide very useful information, they are inherently destructive and require preparation that can, in some cases, be quite significant. PAS techniques offer the potential of bulk, defect analysis in a non-destructive manner, but the assignment of lifetimes to specific trapping sites is complicated by influences from both the grain boundaries and defects within the grains due to the finite timing resolution of radiation detection equipment. The goal of this discussion is to examine the possible trapping sites within LPBF molybdenum and Mo-0.1SiC and establish which of these are likely to be contributing to the annihilation characteristics.

5.3.1 Grain Boundaries

Positrons can reach depths of up to 100-150 μm in molybdenum using the ^{22}Na source. Once implanted, thermalization occurs rapidly, within about a few picoseconds [115]. The thermalized positron will then diffuse through the lattice in a random-walk manner. In molybdenum, the diffusion length is less than 100 nm and is dependent on the defect concentration in the lattice, with positrons in more annealed (i.e. less defected) samples having an increased diffusion length [111]. The average grain diameters in Table 4.4 are orders of magnitude larger than the positron diffusion length. The probability of annihilation at a specific trapping site is proportional to the probability of diffusing to that trapping site and due to grain size and diffusion length difference, which is at least three orders of magnitude larger, this probability

is very small [164]. The lifetime of positrons would be expected to be in the 350-450 ps range associated with microvoids. The average grain diameter for the traditionally manufactured molybdenum was much smaller than for the LPBF specimens, however there was no indication of a longer lifetime component that could be associated with grain boundaries as only a single lifetime component of 136.9 ps was identified. McKee et al. [165] note that grain diameters on the order of 1 μm would be required to have consequential contributions the positron annihilation characteristics. As the grain diameters of the LPBF specimens are much larger than this, it is unlikely that the grain boundaries are influencing the positron lifetime spectra in a meaningful way which indicates the trapping sites are located within the grains themselves.

5.3.2 Defect-Free Bulk Material

In well-annealed materials, the most common channel for positron annihilation is the bulk region where the crystal lattice exhibits no defects. This lifetime is generally very low for all metals and, as mentioned previously in Table 5.4, is 115 ps in molybdenum. The two-component unconstrained analysis indicated that this lifetime was present in the pure molybdenum but not the Mo-0.1SiC specimens. Figure 5.3 shows that the 115 ps component decreases from ∼51% at the 100 mm/s to ∼27% at 400 mm/s before increasing back to ∼33% at 800 mm/s. The laser scanning speed influences the solidification rates of the melt-pool. At lower scan speeds the cooling rate that the melt-pool experiences is slower which provides more time and energy for recovery and recrystallization to occur within the grains. It is expected that the defect-free lifetime would be more intense in the specimens at lower scan speeds. Interestingly; however, the GOS graphs imply that the recrystallized fraction is the highest at the 800 mm/s scan speed. It is postulated that due to the high scan rate, much of the original grains from the powder feedstock are still present and retain

their original structure and stress state due to never fully melting.

5.3.3 Dislocations

Dislocations are linear defects in crystalline materials that influence many macroscopic properties. They can be created by the external loading or unloading as well as the agglomeration of self-interstitial atoms [166]. The lifetime associated with dislocations (∼135-140 ps) was noted in all the samples measured to include the molybdenum standard. It is very likely that LPBF and the rolling or extrusion process resulted in the formation of dislocations so there is confidence that these are acting as the trapping sites associated with this lifetime. Positron studies of deformed molybdenum have shown decreased dislocation density at 500°C after one hour of annealing [140]. The molybdenum standard would have been subjected to temperatures higher than this during the manufacturing process. It is possible that the mechanical processes used to prepare a section of the molybdenum bar for positron analysis resulted in an increase in dislocation density. The positron spectra for each set of LPBF specimens indicate the presence of dislocations. The intensity of the 135 ps lifetime component increases by ∼20% across the 100, 200, and 400 mm/s scan speeds. At the 100 mm/s scan speed the defect-free component is more prevalent, but the dislocation component is more prevalent at faster speeds. This is likely caused by the rapid solidification of the melt-pool. The intensity falls at the 800 mm/s due to, again, incomplete melting of the powder particles. Unlike the pure molybdenum samples, the dislocation lifetime component is the predominant component in the Mo-0.1SiC specimens at a consistent intensity of ∼92% for all four scan speeds. Dislocations form around nanoparticles in a metal matrix, and these dislocations can become intersected and tangled [167]. Additionally, the presence of both carbon and oxygen has been shown to pin dislocation motion in molybdenum reducing the annihilation

rate of defects [168]. The large intensity associated with the the dislocation lifetime is due to the presence of silicon and oxygen containing nanoparticles distributed within the molybdenum grains. The increased presence of dislocations in the Mo-0.1SiC helps to explain the differences in flexural strength between the Mo-0.1SiC and pure molybdenum specimens. Increased dislocation density creates stress within the crystal lattice which impedes dislocation motion, in a process known as strain hardening. The EBSD analysis does not provide evidence of this vast disparity in dislocation behavior as the influence of the nanoparticles in the grains is not captured. The differences between the pure molybdenum and Mo-0.1SiC GOS graphs are due to the improved energy coupling of the powder system which resulted in higher melt-pool temperatures, improved melting, and increased recrystallization [143].

5.3.4 Secondary Phases

Two types of secondary phase nanoparticles were found in the LPBF specimens. Evidence of molybdenum oxides was revealed through SEM on the fracture surfaces of both the pure molybdenum and Mo-0.1SiC specimens while silicon oxide containing nanoparticles were found well distributed throughout the grains of the Mo-0.1SiC specimens by TEM. The solubility of oxygen in molybdenum is quite low and the segregation of the oxides formed during printing occurs at the grain boundaries [169]. The influence of the grain boundaries is expected to be minimal, thus the presence of a lifetime corresponding to annihilations in molybdenum oxides is unlikely to be found with any significant intensity. Chemical composition analysis showed that the oxygen content was significantly higher in the pure molybdenum specimens than in the Mo-0.1SiC and that the amount of oxygen increased monotonically with scan speed [143]. It was clear that the increased melt-pool temperature at lower scan speeds drove the reduction in oxygen; however, it was noted that the silicon sequestered an amount

of oxygen into nanoparticles. As positrons diffuse through the crystal lattice, they are repelled by the surrounding atoms so any regions of decreased atomic density or increased electronic density are attractive trapping sites. Therefore, it is likely that positrons will diffuse to, and annihilate in, the silicon oxide nanoparticles. The lifetime for α-quartz, estimated to be around 261 ps, was fixed in the Mo-0.1SiC positron spectra and, as Figure 5.5 shows, the intensity increases monotonically with scan speed similarly to the increase shown for the oxygen content. This provides evidence that some of the additional oxygen that was found in the Mo-0.1SiC at the higher scan speeds was captured by the silicon and sequestered. It is well known that nanoparticles can pin grain boundaries in materials thus increasing strength and hardness. The increasing intensity of the 261 ps lifetime can be correlated to the hardness measurements conducted on these specimens as both indicate an increasing abundance of secondary-phase nanoparticles. The increased abundance at 800 mm/s confirms that the flexural strength of the Mo-0.1SiC was primarily influenced by lack-of-fusion as the grain size and presence of a secondary-phase would lead to an expected increase in strength, where instead a decrease was observed. This information was not readily determined through the use of SEM and TEM, further highlighting the role that bulk measurement tools like PAS techniques can fill for AM materials.

5.3.5 Voids

The lifetime for nano-voids was fixed at 430 ps for both sets of LPBF specimens as they were expected to be present at HAGBs. As mentioned previously, HAGBs become more prevalent as grain sizes decrease. This trend was observed in the Mo-0.1SiC specimens (Table 4.7), but the intensity of the 430 ps component (Figure 5.5) decreased. This indicates that the 430 ps lifetime component corresponds to voids not present at HAGBs, but more likely within the grains themselves. The

intensity of this component in the Mo-0.1SiC specimens is inversely related to the component associated with SiO_2. As the energy deposited into the powder system increases, so too does powder vaporization. Vaporization of the metal powder can lead to melt-pool instability, key-hole pores, porosity, and lack-of-fusion defects [170]. Molybdenum has a tendency to oxidize under LPBF conditions, first to MoO_2 and then further to MoO_3. MoO_3 exhibits extensive volatility and vaporizes readily at the high temperatures see during LPBF [171]. At higher scan speeds, the overall energy supplied to the powder system is lower resulting in less vaporization and more oxygen present in the consolidated component. While the 430 ps component corresponds to voids that are 5-15 vacancies in size which is much smaller than the standard size of key-hole pores, which are generally on the order of dozens of microns [172], it is likely that these voids present in the grains are due to the evaporation of trapped gases but are not big enough to be considered key-hole pores. An intensity of the void component decreases because less evaporation can occur at the higher scan speeds.

5.3.6 Effect of Orientation

A comparison of the pure molybdenum transverse and longitudinal specimens unconstrained lifetime analysis in Tables 5.1 and 5.2 show minor differences compared to those between the pure molybdenum and Mo-0.1SiC specimens. In general, the τ_2 component decreases in lifetime and increases in intensity with increasing scan speed for both orientations. This is consistent with a growing dislocation density due to increased cooling rates. Similar to the unconstrained analysis for the Mo-0.1SiC specimens, it is likely the two lifetime parameters contain information that is a convolution of multiple trapping locations. The constrained analysis ensures that the characteristic lifetime parameters are associated with similar trapping sites in the longitudinal and transverse directions. There was clear evidence in the constrained

analysis of the defect-free region; however at reduced intensities for the 100, 200, and 800 mm/s scan speeds. The intensities of the defect-free and dislocation lifetimes are essentially the same at the 400 mm/s scan speed. This is indicative of dislocations spatially oriented in the crystal structure in such a way as to trap more positrons in the longitudinal orientation. The difference in the intensity associated with micro-voids is not as readily apparent in the constrained analysis, but coupled with the τ_2 in the unconstrained analysis, it is likely that the positrons implanting on the longitudinal surfaces are not being trapped in micro-voids at an appreciable rate compared to the transverse specimens printed at the 400 and 800 mm/s scan speeds. The difference in rate is indicative of micro-voids that are not spherical, as the presentation of the void surface in the longitudinal orientation is less than that in the transverse, and thus, less positrons are trapped.

5.4 Conclusion

The comparison of results of the EBSD OIM analyses and the PALS measurements has yielded the following conclusions:

1. Grain boundary evolution during the LPBF process was observable through IPF plots and KAM maps; however their influence on the positron annihilation characteristics was insignificant.

2. The ability of the collected single-detector DBAR data to distinguish microstructural differences proved inconclusive due to significant detector resolution drift over the course of the measurements.

3. The pure molybdenum specimens exhibit a positron lifetime corresponding to a defect-free region in the lattice whereas the Mo-0.1SiC do not.

4. PALS measurements highlight the presence of silicon oxide nanoparticles and

the greatly increased dislocation density in the Mo-0.1SiC, a microstructural feature that was not readily observable from the EBSD analysis.

5. PALS provides evidence that the quantity of silicon oxide nanoparticles in the consolidated material increases at higher laser scan speeds.

6. Microvoids are present in the Mo-0.1SiC specimens as a result of metal vaporization, however the subsurface, bulk nature of these pores do not easily allow for non-destructive analysis through traditional electron microscopy techniques.

The investigation of pure molybdenum and Mo-0.1SiC specimens by PALS measurements have proven the usefulness of PALS to the study of AM materials by elucidating nanoparticle and atomic level defects. Evidence is shown for microstructural features that are not fully observed by traditional SEM and TEM analysis.

VI. Conclusions

The goals of the research presented in this dissertation were to improve the density and crack resistance of LPBF molybdenum through the addition of silicon carbide nanoparticles and show that the variations in microstructural environments found in LPBF molybdenum could be observed through PAS. These objectives were successfully reached through the microstructural characterization, mechanical testing, and PAS studies performed in support of this dissertation. The sections of this chapter highlight the research conclusions that support the Problem Statements and Hypotheses presented in Chapter 1. This chapter concludes with the recommendation of future work to be done in the future regarding study of additively manufactured metals through positron annihilation spectroscopy.

6.1 Microstructural and Mechanical Summary and Contributions

The traditional microstructural analysis and mechanical testing presented in Chapter 4 addressed the research objectives in **Problem Statement 1**. **Problem Statement 1** identified the main culprit of molybdenum's poor LPBF performance as oxygen segregation to the grain boundaries and their subsequent embrittlement. Four hypotheses were proposed under **Problem Statement 1**. **Hypothesis 1.A** proposed that the addition of silicon carbide would reduce the segregation of oxygen impurities during consolidation and increase grain boundary strength and cohesion. **Hypothesis 1.B** proposed that the increased grain boundary strength would reduce cracking, porosity, and improve mechanical properties. **Hypothesis 1.C** proposed that the addition of nanoparticles to molybdenum powder would increase the ability of the powder bed to absorb the energy from the laser and improve melting. **Hypothesis 1.D** proposed that the additions of carbides to AM molybdenum would behave simi-

larly to those in AM tungsten and create secondary phase silicon-oxygen nanoparticles that sequester oxygen from the grain boundaries. The objectives of **Problem Statement 1** were achieved by consolidating pure molybdenum and molybdenum with a dilute, 0.1wt%, addition of silicon carbide nanoparticles at four different scan speeds of 100, 200, 400, and 800 mm/s. Powders were characterized through electron microscopy, inert gas fusion and laser reflectance techniques. The consolidated samples were subjected to inert gas fusion, electron backscatter diffraction (EBSD), optically determined porosity, energy dispersive x-ray spectroscopy (EDS), three-point bending strength and Vickers hardness measurements. The addition of 0.1 wt% silicon carbide was successful in reducing the concentration of oxygen present in the consolidation samples verifying **Hypothesis 1.A**. The pure molybdenum samples prepared showed up to 60% oxygen by way of comparison. The extensive microstructural characterization performed in support of **Hypothesis 1.A** enabled the analysis of the PAS studies in Chapter 5. The cross-sectional porosity in the Mo-0.1SiC was reduced by as much as 92% compared to pure molybdenum and the flexural strength and hardness were improved by 80% and 60%, respectively, verifying **Hypothesis 1.B**. The improvement in consolidation resulted in the differences between the pure molybdenum and Mo-0.1SiC specimens, but only flexural strength in the Mo-0.1SiC specimens was governed, in part, by grain boundary strengthening. The reduction in porosity in the Mo-0.1SiC confirmed the improved melting and the reflectance measurements of the pure molybdenum and Mo-0.1SiC powders confirmed that this was likely due to increased scattering and subsequent absorption of the incident laser verifying **Hypothesis 1.C**. Transmission electron microscopy (TEM) and its associated EDS measurements confirmed the presence of secondary-phase, silicon-oxygen nanoparticles. Scanning electron microscopy (SEM) imaging indicated that the secondary-phase was well distributed throughout the bulk of the consolidated samples. Along with the over

reduction of carbon and oxygen in the Mo-0.1SiC samples after consolidation, these findings belied two mechanisms of oxygen reduction and verified **Hypothesis 1.D**.

The contributions from the research in support of **Problem Statement 1** are as follows:

1. Identified silicon carbide nanoparticles as an option for improving the melting and consolidation of LPBF molybdenum.

2. Published the first characterization of LPBF molybdenum with the addition of silicon carbide [143].

3. Showed that the in-situ oxidation of molybdenum powder was reduced in the powder system by as much as 60% [143].

4. Demonstrated the reduction in cross-sectional porosity of up to 92% due to the addition of silicon carbide [143].

5. Documented the presence of silicon-oxygen containing nanoparticles, indicating a similar secondary-phase formation process to tungsten [143].

6. Compared hardness and flexural strength properties between LPBF molybdenum and LPBF Mo-0.1SiC demonstrating improvement at all scan speeds with the addition of the silicon carbide nanoparticles to the powder system [143].

6.2 PAS Summary and Contributions

The PAS studies presented in Chapter 5 addressed the research objectives in **Problem Statements 2 and 3**. **Problem Statement 2** recognized the ability of atomic-scale defects in the microstructure of LPBF molybdenum to influence the macroscopic properties like hardness and strength, and additionally, the inability

of traditional characterization techniques to easily identify these defects in a non-destructive manner. **Problem Statement 3** highlighted the orientational differences in LPBF microstructures due to the formation of columnar grains in LPBF metals. Positron lifetime measurements were presented in Chapter 5 and when compared to the EBSD measurements presented in Chapter 4 indicated the influence of grain boundaries on the positron behavior to LPBF molybdenum and Mo-0.1SiC was insignificant. This negatively impacts the verification of **Hypothesis 3** as the lifetimes appeared to be indifferent to the large columnar grains found in the build direction. At the nanostructural scale; however, orientation differences were observed in the annihilation rates in dislocations and micro-voids. The pure molybdenum specimens exhibited a positron lifetime corresponding to a defect-free region in the lattice whereas the Mo-0.1SiC did not. Additionally, micro-voids were identified by positron lifetimes in the LPBF specimens. A lack of evidence of these microstructural differences in the myriad of destructive testing conducted on these specimens verified **Hypothesis 2**. The presence of secondary-phase nanoparticles in the Mo-0.1SiC specimens was highlighted by the positron lifetimes, further supporting **Hypothesis 1.D**.

The contributions from the research in support of **Problem Statements 2 and 3** are as follows:

1. First PAS study of LPBF molybdenum and Mo-0.1SiC.
2. Demonstrated that the positron measurements performed were indifferent to the grain sizes and anisotropic orientation differences in the consolidated specimens tested.
3. Differentiated between defect-free regions found in the pure molybdenum specimens and the defected microstructure found in Mo-0.1SiC due to the presence of the secondary phase nanoparticles.

4. Identified lifetimes characteristic of the presence of silicon-oxygen containing nanoparticles in the Mo-0.1SiC specimens.

6.3 Recommendations

The addition of nanoparticle silicon carbide to the pure molybdenum powder system improves the consolidation through LPBF; however, continued study of the effects of silicon carbide on the LPBF of pure molybdenum is warranted. Future studies should include variation of both silicon carbide particle size and concentration. Single weld tracks produced through the LPBF printer need to be studied to more clearly understand the influence of silicon carbide on the melt-pool size and shape. Furthermore, reflectance measurements on the different powder systems will provide insight on the laser-powder interactions. Due to time constraints, the sample size for this research was necessarily limited to four scan speeds. To inform the trends found in the four scan speed data points, characterization of the 300, 500, 600, and 700 mm/s scan speeds should occur. Printing parameters other than scan speed, such as laser power, hatch spacing, and layer thickness have all been proven to effect the consolidation of LPBF molybdenum in various ways [98]. While exhaustively addressing the entire build parameter design space would be nearly impossible, a controlled study of the influence of powder layer depth and hatch spacing on the positron annihilation lifetimes would provide a clearer picture of the differences observed during this work.

The oxidation of refractory metals and alloys remains a problem that must be solved. Ab initio simulation methods have effectively shown the stability of certain oxides present within a refractory metal system [173]. Studying the Mo-0.1SiC system along with other concentrations of silicon carbide would identify the thermodynamically favorable formation of silicon, carbon, and molybdenum oxides and assess the potential for silicon carbide additions to aid in the oxidation resistance of the consol-

idated component.

PALS measurements were able to distinguish between the Mo-0.1SiC and pure molybdenum specimens at a nano-scale resolution; however the PALS array is limited to only one experimental run a week due to low throughput and the size of the data files generated for each run. The PALS Array was built as a digital test bed and not a production system. A tuned, high-throughput analog system would be sufficient for subsequent measurements. Using such a system would allow for many more samples to be run in a short amount of time and would inform the suspected trends derived from the four data points used in this dissertation.

The Doppler-broadening measurements proved inconclusive due to detector resolution drift. While unconfirmed, it is possible that this drift was due to changing environmental or electronic conditions over the extended period needed for measurements due to the PALS Array. It is also possible that the variation is due to material specific attenuation or the varying thickness of the samples. Potential exists that there could be a quantifiable linear relationship between the detector resolution and the lineshape parameters that are characteristic of the broadening of the 511 keV photopeak. DBAR measurements on multiple different samples in replicate are required to confirm this assessment. This does not absolve the high energy background issues inherent to single detector DBAR experiments though. There are a few methods available to examine the differences in high energy annihilations, to include the use of a two detector-coincident technique, extensive post-processing, mathematical treatment of the data to numerically reduce background or the use of ^{68}Ge source [130]. These methods would be appropriate for high momenta examination, but only after the systematic variation is addressed and resolved.

Bibliography

1. K. Deprez, R. Van Holen, K. Van Audenhaege, and S. Vandenberghe, "Additive manufacturing of high density tungsten collimators," *Journal of Nuclear Medicine*, vol. 53, no. supplement 1, pp. 2394–2394, 2012. [Online]. Available: https://jnm.snmjournals.org/content/53/supplement_1/2394

2. C. Yin, D. Terentyev, T. Zhang, S. Nogami, S. Antusch, C.-C. Chang, R. H. Petrov, and T. Pardoen, "Ductile to brittle transition temperature of advanced tungsten alloys for nuclear fusion applications deduced by miniaturized three-point bending tests," *International Journal of Refractory Metals and Hard Materials*, vol. 95, p. 105464, 2021. [Online]. Available: https://www.sciencedirect.com/science/article/pii/S0263436820303401

3. A. Talignani, R. Seede, A. Whitt, S. Zheng, J. Ye, I. Karaman, M. M. Kirka, Y. Katoh, and Y. M. Wang, "A review on additive manufacturing of refractory tungsten and tungsten alloys," *Additive Manufacturing*, vol. 58, p. 103009, 2022. [Online]. Available: https://www.sciencedirect.com/science/article/pii/S221486042200402X

4. C. C. Eckley, R. A. Kemnitz, C. P. Fassio, C. R. Hartsfield, and T. A. Leonhardt, "Selective laser melting of tungsten-rhenium alloys," *JOM*, vol. 73, pp. 3439–3450, 2021.

5. D. J. Newell, R. P. O'Hara, G. R. Cobb, A. N. Palazotto, M. M. Kirka, L. W. Burggraf, and J. A. Hess, "Mitigation of scan strategy effects and material anisotropy through supersolvus annealing in LPBF IN718," *Materials Science and Engineering: A*, vol. 764, p. 138230, 2019. [Online]. Available: https://www.sciencedirect.com/science/article/pii/S0921509319310160

6. I. Gibson, D. Rosen, and B. Stucker, "Additive manufacturing technologies: 3D printing," *Rapid Prototyping and Direct Digital Manufacturing*, 2014.

7. P. Charalampous, I. Kostavelis, and D. Tzovaras, "Non-destructive quality control methods in additive manufacturing: a survey," *Rapid Prototyping Journal*, vol. 26, no. 4, pp. 777–790, 2020.

8. P. Liacouras and N. Wake, "Chapter 5 - 3D Printing Principles and Technologies," pp. 61–73, 2022. [Online]. Available: https://www.sciencedirect.com/science/article/pii/B9780323775731000166

9. S. Pfeiffer, K. Florio, D. Puccio, M. Grasso, B. M. Colosimo, C. G. Aneziris, K. Wegener, and T. Graule, "Direct laser additive manufacturing of high performance oxide ceramics: A state-of-the-art review," *Journal of the European Ceramic Society*, 2021. [Online]. Available: https://www.sciencedirect.com/science/article/pii/S0955221921003617

10. N. Sohrabi, J. Jhabvala, G. Kurtuldu, R. Frison, A. Parrilli, M. Stoica, A. Neels, J. F. Löffler, and R. E. Logé, "Additive manufacturing of a precious bulk metallic glass," *Applied Materials Today*, vol. 24, p. 101080, 2021. [Online]. Available: https://www.sciencedirect.com/science/article/pii/S2352940721001451

11. N. Singh, A. Rana, and G. K. Badhotiya, "Manufacturing processes for the development of engineered wood – a mini-review," *Materials Today: Proceedings*, 2021. [Online]. Available: https://www.sciencedirect.com/science/article/pii/S2214785321017594

12. M. K. Islam, P. J. Hazell, J. P. Escobedo, and H. Wang, "Biomimetic armour design strategies for additive manufacturing: A review," *Materials Design*,

vol. 205, p. 109730, 2021. [Online]. Available: https://www.sciencedirect.com/science/article/pii/S0264127521002823

13. R. L. Bradford, L. Cao, D. Klosterman, F. Herman, L. Forman, and C. Browning, "A metal-metal powder formulation approach for laser additive manufacturing of difficult-to-print high-strength aluminum alloys," *Materials Letters*, p. 130113, 2021. [Online]. Available: https://www.sciencedirect.com/science/article/pii/S0167577X21008107

14. M. T. Hasib, H. E. Ostergaard, Q. Liu, X. Li, and J. J. Kruzic, "Tensile and fatigue crack growth behavior of commercially pure titanium produced by laser powder bed fusion additive manufacturing," *Additive Manufacturing*, p. 102027, 2021. [Online]. Available: https://www.sciencedirect.com/science/article/pii/S2214860421001925

15. R. K. Upadhyay and A. Kumar, "Scratch and wear resistance of additive manufactured 316L stainless steel sample fabricated by laser powder bed fusion technique," *Wear*, vol. 458-459, p. 203437, 2020. [Online]. Available: https://www.sciencedirect.com/science/article/pii/S0043164820308966

16. M. Guo, D. Gu, L. Xi, H. Zhang, J. Zhang, J. Yang, and R. Wang, "Selective laser melting additive manufacturing of pure tungsten: Role of volumetric energy density on densification, microstructure and mechanical properties," *International Journal of Refractory Metals and Hard Materials*, vol. 84, p. 105025, 2019. [Online]. Available: https://www.sciencedirect.com/science/article/pii/S0263436819302094

17. C. Sungail and A. Abid, "Spherical tantalum feed powder for metal additive manufacturing," *Metal Powder Report*, vol. 73, no. 6, pp. 316–318,

2018. [Online]. Available: https://www.sciencedirect.com/science/article/pii/S0026065718301309

18. M. A. Melia, S. R. Whetten, R. Puckett, M. Jones, M. J. Heiden, N. Argibay, and A. B. Kustas, "High-throughput additive manufacturing and characterization of refractory high entropy alloys," *Applied Materials Today*, vol. 19, p. 100560, 2020. [Online]. Available: https://www.sciencedirect.com/science/article/pii/S235294072030007X

19. T. Andrews, R. Rapp, E. Elwakil, E. Dietz, and S. Baroudi, "Sourcing materials for additive manufacturing," *The Military Engineer*, vol. 112, no. 729, pp. 59–60, 2020.

20. M. Oyesola, K. Mpofu, and N. Mathe, "A techno-economic analytical approach of laser-based additive manufacturing processes for aerospace application," *Procedia Manufacturing*, vol. 35, pp. 155–163, 2019, the 2nd International Conference on Sustainable Materials Processing and Manufacturing, SMPM 2019, 8-10 March 2019, Sun City, South Africa. [Online]. Available: https://www.sciencedirect.com/science/article/pii/S2351978919306535

21. S. Talib, S. Gupta, V. Chaudhary, P. Gupta, and M. A. Wahid, "Additive manufacturing: Materials, techniques and biomedical applications," *Materials Today: Proceedings*, 2021. [Online]. Available: https://www.sciencedirect.com/science/article/pii/S2214785321033587

22. S. Ferrari, M. Loveridge, S. D. Beattie, M. Jahn, R. J. Dashwood, and R. Bhagat, "Latest advances in the manufacturing of 3D rechargeable lithium microbatteries," *Journal of Power Sources*, vol. 286, pp. 25–46, 2015. [Online]. Available: https://www.sciencedirect.com/science/article/pii/S0378775315005571

23. M. H. Mosallanejad, B. Niroumand, A. Aversa, and A. Saboori, "In-situ alloying in laser-based additive manufacturing processes: A critical review," *Journal of Alloys and Compounds*, vol. 872, p. 159567, 2021. [Online]. Available: https://www.sciencedirect.com/science/article/pii/S0925838821009762

24. S. Sanchez, P. Smith, Z. Xu, G. Gaspard, C. J. Hyde, W. W. Wits, I. A. Ashcroft, H. Chen, and A. T. Clare, "Powder bed fusion of nickel-based superalloys: A review," *International Journal of Machine Tools and Manufacture*, vol. 165, p. 103729, 2021. [Online]. Available: https://www.sciencedirect.com/science/article/pii/S0890695521000390

25. L. L. Snead, D. T. Hoelzer, M. Rieth, and A. A. Nemith, "Chapter 13 - Refractory Alloys: Vanadium, Niobium, Molybdenum, Tungsten," in *Structural Alloys for Nuclear Energy Applications*, G. R. Odette and S. J. Zinkle, Eds. Boston: Elsevier, 2019, pp. 585–640. [Online]. Available: https://www.sciencedirect.com/science/article/pii/B9780123970466000137

26. F. Hinrichs, A. Kauffmann, D. Schliephake, S. Seils, S. Obert, K. Ratschbacher, M. Allen, A. Pundt, and M. Heilmaier, "Flexible powder production for additive manufacturing of refractory metal-based alloys," *Metals*, vol. 11, no. 11, 2021. [Online]. Available: https://www.mdpi.com/2075-4701/11/11/1723

27. D. S. Thomas and S. W. Gilbert, "Cost and cost effectiveness of additive manufacturing," *NIST Special Publication 1176*, vol. 255, no. 9, p. 1800051, 2014. [Online]. Available: https://onlinelibrary.wiley.com/doi/abs/10.1002/pssb.201800051

28. Wildebeest, "London metal exchange begins trading cobalt and molybdenum," 2010. [Online]. Available: https://seekingalpha.com/article/189819-london-metal-exchange-begins-trading-cobalt-and-molybdenum

29. J. Braun, L. Kaserer, J. Stajkovic, K.-H. Leitz, B. Tabernig, P. Singer, P. Leibenguth, C. Gspan, H. Kestler, and G. Leichtfried, "Molybdenum and tungsten manufactured by selective laser melting: Analysis of defect structure and solidification mechanisms," *International Journal of Refractory Metals and Hard Materials*, vol. 84, p. 104999, 2019. [Online]. Available: https://www.sciencedirect.com/science/article/pii/S0263436819302288

30. D. Faidel, D. Jonas, G. Natour, and W. Behr, "Investigation of the selective laser melting process with molybdenum powder," *Additive Manufacturing*, vol. 8, pp. 88–94, 2015. [Online]. Available: https://www.sciencedirect.com/science/article/pii/S2214860415000457

31. D. Wang, C. Yu, J. Ma, W. Liu, and Z. Shen, "Densification and crack suppression in selective laser melting of pure molybdenum," *Materials Design*, vol. 129, pp. 44–52, 2017. [Online]. Available: https://www.sciencedirect.com/science/article/pii/S0264127517304513

32. L. Kaserer, J. Braun, J. Stajkovic, K.-H. Leitz, B. Tabernig, P. Singer, I. Letofsky-Papst, H. Kestler, and G. Leichtfried, "Fully dense and crack free molybdenum manufactured by selective laser melting through alloying with carbon," *International Journal of Refractory Metals and Hard Materials*, vol. 84, p. 105000, 2019. [Online]. Available: https://www.sciencedirect.com/science/article/pii/S026343681930229X

33. J. Braun, L. Kaserer, I. Letofsky-Papst, K.-H. Leitz, H. Kestler, and G. Leichtfried, "On the role of carbon in molybdenum manufactured by laser powder bed fusion," *International Journal of Refractory Metals and Hard Materials*, vol. 92, p. 105283, 2020. [Online]. Available: https://www.sciencedirect.com/science/article/pii/S0263436820301591

34. J. Braun, L. Kaserer, J. Stajkovic, H. Kestler, and G. Leichtfried, "Grain refinement mechanisms of alloying molybdenum with carbon manufactured by laser powder bed fusion," *Materials Design*, vol. 215, p. 110507, 2022. [Online]. Available: https://www.sciencedirect.com/science/article/pii/S0264127522001289

35. N. Li, S. Huang, G. Zhang, R. Qin, W. Liu, H. Xiong, G. Shi, and J. Blackburn, "Progress in additive manufacturing on new materials: A review," *Journal of Materials Science Technology*, vol. 35, no. 2, pp. 242–269, 2019, recent Advances in Additive Manufacturing of Metals and Alloys. [Online]. Available: https://www.sciencedirect.com/science/article/pii/S1005030218301786

36. S. Chen, W.-B. Li, X. ming Wang, and W. jin Yao, "Explosion/impact response of pure molybdenum at ultra-high strain rate and large strains," *International Journal of Refractory Metals and Hard Materials*, vol. 104, p. 105801, 2022. [Online]. Available: https://www.sciencedirect.com/science/article/pii/S0263436822000257

37. J. Slotwinski, E. Garboczi, P. Stutzman, C. Ferraris, S. Watson, and M. Peltz, "Characterization of metal powders used for additive manufacturing," *Journal of Research of the National Institute of Standards and Technology*, vol. 119, pp. 460–493, 2014.

38. S. Berumen, F. Bechmann, S. Lindner, J.-P. Kruth, and T. Craeghs, "Quality control of laser- and powder bed-based additive manufacturing (AM) technologies," *Physics Procedia*, vol. 5, pp. 617–622, 2010, Laser Assisted Net Shape Engineering 6, Proceedings of the LANE 2010, Part 2. [Online]. Available: https://www.sciencedirect.com/science/article/pii/S1875389210005158

39. F. Xu, N. Madhaven, V. Dhokia, A. McAndrew, P. Colegrove, and S. Williams, "Multi-sensor system for wire-fed additive manufacture of titanium alloys," *26th International conference on Flexible Automation and Intelligent Manufacturing*, 2016.

40. H. Rieder, M. Spies, J. Bamberg, and B. Henkel, "On- and offline ultrasonic characterization of components built by slm additive manufacturing," *Proceedings of the AIP Conference*, p. 130002, 2016.

41. R. J. Smith, M. Hirsch, R. Patel, W. Li, A. T. Clare, and S. D. Sharples, "Spatially resolved acoustic spectroscopy for selective laser melting," *Journal of Materials Processing Technology*, vol. 236, pp. 93–102, 2016. [Online]. Available: https://www.sciencedirect.com/science/article/pii/S0924013616301352

42. I. Yadroitsev, P. Krakhmalev, and I. Yadroitsava, "Selective laser melting of Ti6Al4V alloy for biomedical applications: Temperature monitoring and microstructural evolution," *Journal of Alloys and Compounds*, vol. 583, pp. 404–409, 2014. [Online]. Available: https://www.sciencedirect.com/science/article/pii/S0925838813020689

43. A. Dunbar, A. Nassar, E. Reutzel, and J. Blecher, "A real-time communication architecture for metal powder bed fusion additive manufacting," *Solid Freeform Fabrication 2016, Proceedings of the 27th Annual International Solid Freeform Fabrication Symposium.*

44. G. Mohr, S. J. Altenburg, A. Ulbricht, P. Heinrich, D. Baum, C. Maierhofer, and K. Hilgenberg, "In-situ defect detection in laser powder bed fusion by using thermography and optical tomography—comparison to computed tomography," *Metals*, vol. 10, no. 1, 2020. [Online]. Available: https://www.mdpi.com/2075-4701/10/1/103

45. A. du Plessis, I. Yadroitsev, I. Yadroitsava, and S. G. Le Roux, "X-ray microcomputed tomography in additive manufacturing: A review of the current technology and applications," *3D Printing and Additive Manufacturing*, vol. 5, no. 3, pp. 227–247, 2018. [Online]. Available: https://doi.org/10.1089/3dp.2018.0060

46. A. du Plessis, I. Yadroitsava, and I. Yadroitsev, "Effects of defects on mechanical properties in metal additive manufacturing: A review focusing on x-ray tomography insights," *Materials Design*, vol. 187, p. 108385, 2020. [Online]. Available: https://www.sciencedirect.com/science/article/pii/S0264127519308238

47. R. J. Williams, A. Piglione, T. Rønneberg, C. Jones, M.-S. Pham, C. M. Davies, and P. A. Hooper, "In situ thermography for laser powder bed fusion: Effects of layer temperature on porosity, microstructure and mechanical properties," *Additive Manufacturing*, vol. 30, p. 100880, 2019. [Online]. Available: https://www.sciencedirect.com/science/article/pii/S2214860419303410

48. V. Mahato, M. A. Obeidi, D. Brabazon, and P. Cunningham, "An evaluation of classification methods for 3D printing time-series data," *CoRR*, vol. abs/2010.00903, 2020. [Online]. Available: https://arxiv.org/abs/2010.00903

49. R. McCann, M. A. Obeidi, C. Hughes, Éanna McCarthy, D. S. Egan, R. K. Vijayaraghavan, A. M. Joshi, V. Acinas Garzon, D. P. Dowling, P. J. McNally, and D. Brabazon, "In-situ sensing, process monitoring and machine control in laser powder bed fusion: A review," *Additive Manufacturing*, vol. 45, p. 102058, 2021. [Online]. Available: https://www.sciencedirect.com/science/article/pii/S2214860421002232

50. K. Babinsky, S. Primig, W. Knabl, A. Lorich, R. Stickler, and H. Clemens, "Fracture behavior and delamination toughening of molybdenum in charpy impact tests," *JOM*, vol. 68, no. 11, pp. 2854–2863, Nov 2016. [Online]. Available: https://doi.org/10.1007/s11837-016-2075-y

51. A. Wronski, A. Chilton, and E. Capron, "The ductile-brittle transition in polycrystalline molybdenum," *Acta Metallurgica*, vol. 17, no. 6, pp. 751–755, 1969. [Online]. Available: https://www.sciencedirect.com/science/article/pii/0001616069900819

52. A. Iveković, N. Omidvari, B. Vrancken, K. Lietaert, L. Thijs, K. Vanmeensel, J. Vleugels, and J.-P. Kruth, "Selective laser melting of tungsten and tungsten alloys," *International Journal of Refractory Metals and Hard Materials*, vol. 72, pp. 27–32, 2018. [Online]. Available: https://www.sciencedirect.com/science/article/pii/S0263436817307618

53. American Society for Testing and Materials, *ASTM E1019-18: Standard Testing Methods for Determination of Carbon, Sulfur, Nitrogen, and Oxygen in Steel, Iron, Nickel, and Cobalt Alloys by Various Combustion and Inert Gas Fusion Techniques*. West Conshohocken, PA, USA, 2018.

54. American Society Testing and Materials, *ASTM E903-20: Standard Test Method for Solar Absorptance, Reflectance, and Transmittance of Materials Using Integrating Spheres*. West Conshohocken, PA, USA, 2020.

55. B. Song, S. Wen, C. Yan, Q. Wei, and Y. Shi, "Chapter 6 - Materials Characterization," pp. 231–247, 2021. [Online]. Available: https://www.sciencedirect.com/science/article/pii/B9780081030059000067

56. International Organization for Standardization, *ISO 14577-1: Metallic materials - Instrumented indentation test for hardness and materials parameters - Part 1: Test Method*. Vernier, Geneva, Switzerland, 2015.

57. S. Lyon, "3.17 - Corrosion of Molybdenum and its Alloys," in *Shreir's Corrosion*, B. Cottis, M. Graham, R. Lindsay, S. Lyon, T. Richardson, D. Scantlebury, and H. Stott, Eds. Oxford: Elsevier, 2010, pp. 2157–2167. [Online]. Available: https://www.sciencedirect.com/science/article/pii/B9780444527875001062

58. J. A. Moriarty, "Ultrahigh-pressure structural phase transitions in Cr, Mo, and W," *Phys. Rev. B*, vol. 45, pp. 2004–2014, Feb 1992. [Online]. Available: https://link.aps.org/doi/10.1103/PhysRevB.45.2004

59. A. McMahan, "Pressure-induced changes in the electronic structure of solids," *Physica B+C*, vol. 139-140, pp. 31–41, 1986. [Online]. Available: https://www.sciencedirect.com/science/article/pii/037843638690519X

60. J. C. Jamieson, "Crystal structures of titanium, zirconium, and hafnium at high pressures," *Science*, vol. 140, no. 3562, pp. 72–73, 1963. [Online]. Available: https://www.science.org/doi/abs/10.1126/science.140.3562.72

61. T. D. Dolezal and A. J. Samin, "Adsorption of oxygen to high entropy alloy surfaces for up to 2 ml coverage using density functional theory and monte carlo calculations," *Langmuir*, vol. 38, no. 10, pp. 3158–3169, Mar 2022. [Online]. Available: https://doi.org/10.1021/acs.langmuir.1c03191

62. S. Ogata, J. Li, and S. Yip, "Twinning pathway in bcc molybdenum," *Europhysics Letters*, vol. 68, no. 3, p. 405, Oct 2004. [Online]. Available: https://dx.doi.org/10.1209/epl/i2004-10201-y

63. J. Christian and S. Mahajan, "Deformation twinning," *Progress in Materials Science*, vol. 39, no. 1, pp. 1–157, 1995. [Online]. Available: https://www.sciencedirect.com/science/article/pii/0079642594000077

64. D. Killeffer, *Molybdenum Compounds: Their Chemistry and Technology*. Interscience Publishers, 1952, ch. Oxides of Molybdenum.

65. E. A. Gulbransen, K. F. Andrew, and F. A. Brassart, "Oxidation of molybdenum 550° to 1700°C," *Journal of The Electrochemical Society*, vol. 110, no. 9, p. 952, sep 1963. [Online]. Available: https://dx.doi.org/10.1149/1.2425918

66. H. M. Spencer and J. L. Justice, "The reaction of carbon monoxide on molybdenum oxides," *Journal of the American Chemical Society*, vol. 56, no. 11, pp. 2301–2306, 1934. [Online]. Available: https://doi.org/10.1021/ja01326a025

67. S. Chaudhury, S. Mukerjee, V. Vaidya, and V. Venugopal, "Kinetics and mechanism of carbothermic reduction of MoO_3 to Mo_2C," *Journal of Alloys and Compounds*, vol. 261, no. 1, pp. 105–113, 1997. [Online]. Available: https://www.sciencedirect.com/science/article/pii/S0925838897002120

68. R. A. Kemnitz, C. C. Eckley, B. M. Sexton, and A. R. LeSieur, "Strengthening of additively manufactured tungsten by use of hydrogen in argon shielding gas," *International Journal of Refractory Metals and Hard Materials*, vol. 110, p. 105970, 2023. [Online]. Available: https://www.sciencedirect.com/science/article/pii/S0263436822001949

69. A. Abel, Y. Wessarges, S. Julmi, C. Hoff, J. Hermsdorf, C. Klose, H. J. Maier, S. Kaierle, and L. Overmeyer, "Laser powder bed fusion of WE43 in hydrogen-argon-gas atmosphere," *Procedia CIRP*, vol. 94, pp. 21–24, 2020, 11th

CIRP Conference on Photonic Technologies [LANE 2020]. [Online]. Available: https://www.sciencedirect.com/science/article/pii/S2212827120311902

70. D. Lide, *CRC Handbook of Chemistry and Physics*. CRC Press, 2000, pp. 10–176.

71. L. Backman, J. Gild, J. Luo, and E. J. Opila, "Part I: Theoretical predictions of preferential oxidation in refractory high entropy materials," *Acta Materialia*, vol. 197, pp. 20–27, 2020. [Online]. Available: https://www.sciencedirect.com/science/article/pii/S1359645420305012

72. C. Wang, Q. Li, Z. Guo, X. Li, X. Ding, X. Li, Z. Li, and B. Li, "Study on the pre-oxidation and resulting oxidation mechanism and kinetics of Mo-9Si-8B alloy," *Materials*, vol. 14, no. 18, 2021. [Online]. Available: https://www.mdpi.com/1996-1944/14/18/5309

73. L. Brewer and R. H. Lamoreaux, "The mo-o system (molybdenum-oxygen)," *Bulletin of Alloy Phase Diagrams*, vol. 1, no. 2, pp. 85–89, Sep 1980. [Online]. Available: https://doi.org/10.1007/BF02881199

74. W. Callister Jr. and D. Rethwisch, *Materials Science and Engineering, An Introduction*, 8th ed. John Wiley and Sons, Inc., 2009.

75. H. W. Hugosson, O. Eriksson, L. Nordström, U. Jansson, L. Fast, A. Delin, J. M. Wills, and B. Johansson, "Theory of phase stabilities and bonding mechanisms in stoichiometric and substoichiometric molybdenum carbide," *Journal of Applied Physics*, vol. 86, no. 7, pp. 3758–3767, 1999. [Online]. Available: https://doi.org/10.1063/1.371284

76. H. Okamoto, "Mo-Si (molybdenum-silicon)," *Journal of Phase Equilibria and Diffusion*, vol. 32, no. 2, pp. 176–176, Apr 2011. [Online]. Available: https://doi.org/10.1007/s11669-010-9843-0

77. O. Lenchuk, J. Rohrer, and K. Albe, "Solubility of zirconium and silicon in molybdenum studied by first-principles calculations," *Scripta Materialia*, vol. 97, pp. 1–4, 2015. [Online]. Available: https://www.sciencedirect.com/science/article/pii/S1359646214004060

78. G. jun Zhang, G. Liu, Y. jun Sun, F. Jiang, L. Wang, R. Wang, and J. Sun, "Microstructure and strengthening mechanisms of molybdenum alloy wires doped with lanthanum oxide particles," *International Journal of Refractory Metals and Hard Materials*, vol. 27, no. 1, pp. 173–176, 2009. [Online]. Available: https://www.sciencedirect.com/science/article/pii/S0263436808000723

79. T. Mrotzek, A. Hoffmann, and U. Martin, "Hardening mechanisms and recrystallization behaviour of several molybdenum alloys," *International Journal of Refractory Metals and Hard Materials*, vol. 24, no. 4, pp. 298–305, 2006, selected presentations from the 16th International Plansee Seminar 2005. [Online]. Available: https://www.sciencedirect.com/science/article/pii/S0263436805001472

80. O. D. Neikov, S. S. Naboychenko, I. B. Murashova, and N. A. Yefimov, "Chapter 23 - Production of Refractory Metal Powders," in *Handbook of Non-Ferrous Metal Powders (Second Edition)*, second edition ed., O. D. Neikov, S. S. Naboychenko, and N. A. Yefimov, Eds. Oxford: Elsevier, 2019, pp. 685–755. [Online]. Available: https://www.sciencedirect.com/science/article/pii/B9780081005439000233

81. T. Fujii, R. Watanabe, Y. Hiraoka, and M. Okada, "Effects of rolling procedures on the development of annealing textures in molybdenum sheets," *Journal of the Less Common Metals*, vol. 97, pp. 163–171, 1984. [Online]. Available: https://www.sciencedirect.com/science/article/pii/0022508884900201

82. American Society for Testing and Materials. West Conshohocken, PA, USA, 2018.

83. J. Manriquez-Frayre and D. Bourell, "Selective laser sintering of binary metallic powder," *Solid Freeform Fabrication Symposium*, pp. 99–106, 1990.

84. acrfullGE Additive, "Concept Laser MLab, MLab R, MLab 200R," ge.com/additive.

85. R. K. Enneti, R. Morgan, and S. V. Atre, "Effect of process parameters on the selective laser melting (SLM) of tungsten," *International Journal of Refractory Metals and Hard Materials*, vol. 71, pp. 315–319, 2018. [Online]. Available: https://www.sciencedirect.com/science/article/pii/S0263436817307370

86. N. K. Tolochko, Y. V. Khlopkov, S. E. Mozzharov, M. B. Ignatiev, T. Laoui, and V. I. Titov, "Absorptance of powder materials suitable for laser sintering," *Rapid Prototyping Journal*, vol. 6, no. 3, pp. 155–160, 2000, copyright - Copyright MCB UP Limited (MCB) 2000. [Online]. Available: https://afit.idm.oclc.org/login?url=https://www.proquest.com/scholarly-journals/absorptance-powder-materials-suitable-laser/docview/214036978/se-2?accountid=26185

87. A. Gusarov and J.-P. Kruth, "Modelling of radiation transfer in metallic powders at laser treatment," *International Journal of Heat and Mass Transfer*, vol. 48, pp. 3423–3434, 07 2005.

88. C. D. Boley, S. A. Khairallah, and A. M. Rubenchik, "Calculation of laser absorption by metal powders in additive manufacturing," *Appl. Opt.*, vol. 54, no. 9, pp. 2477–2482, Mar 2015. [Online]. Available: https://opg.optica.org/ao/abstract.cfm?URI=ao-54-9-2477

89. J. Torrent and V. Barrón, *Diffuse Reflectance Spectroscopy.* John Wiley Sons, Ltd, 2008, ch. 13, pp. 367–385. [Online]. Available: https://acsess.onlinelibrary.wiley.com/doi/abs/10.2136/sssabookser5.5.c13

90. S. D. Jadhav, P. P. Dhekne, E. Brodu, B. V. Hooreweder, S. Dadbakhsh, J. P. Kruth, J. van Humbeeck, and K. Vanmeensel, "Laser powder bed fusion additive manufacturing of highly conductive parts made of optically absorptive carburized CuCr1 powder," *Materials & Design*, vol. 198, p. 109369, 2021.

91. S. D. Jadhav, D. xiao Fu, M. Deprez, K. Ramharter, D. Willems, B. V. Hooreweder, and K. Vanmeensel, "Highly conductive and strong $CuSn_{0.3}$ alloy processed via laser powder bed fusion starting from a tin-coated copper powder," *Additive manufacturing*, vol. 36, p. 101607, 2020.

92. O. Tertuliano, P. DePond, D. Doan, M. Matthews, W. Gu, W. Cai, and A. Lew, "Nanoparticle-enhanced absorptivity of copper during laser powder bed fusion," *Additive Manufacturing*, vol. 51, p. 102562, 12 2021.

93. O. Pannitz, F. Großwendt, A. Lüddecke, A. Kwade, A. Röttger, and J. T. Sehrt, "Improved process efficiency in laser-based powder bed fusion of nanoparticle coated maraging tool steel powder," *Materials*, vol. 14, no. 13, 2021. [Online]. Available: https://www.mdpi.com/1996-1944/14/13/3465

94. D. Gu, Y. Yang, L. Xi, J. Yang, and M. Xia, "Laser absorption behavior of randomly packed powder-bed during selective laser melting

of SiC and TiB_2 reinforced Al matrix composites," *Optics Laser Technology*, vol. 119, p. 105600, 2019. [Online]. Available: https://www.sciencedirect.com/science/article/pii/S0030399219302658

95. K.-H. Leitz, P. Singer, A. Plankensteiner, B. Tabernig, H. Kestler, and L. S. Sigl, "Thermo-fluid dynamical simulation of layer build-up by selective laser melting of molybdenum and steel," *BHM Berg- und Hüttenmännische Monatshefte*, vol. 162, no. 5, pp. 172–178, May 2017. [Online]. Available: https://doi.org/10.1007/s00501-017-0588-5

96. K.-H. Leitz, C. Grohs, P. Singer, B. Tabernig, A. Plankensteiner, H. Kestler, and L. Sigl, "Fundamental analysis of the influence of powder characteristics in selective laser melting of molybdenum based on a multi-physical simulation model," *International Journal of Refractory Metals and Hard Materials*, vol. 72, pp. 1–8, 2018. [Online]. Available: https://www.sciencedirect.com/science/article/pii/S026343681730776X

97. P. Bajaj, J. Wright, I. Todd, and E. A. Jägle, "Predictive process parameter selection for selective laser melting manufacturing: Applications to high thermal conductivity alloys," *Additive Manufacturing*, vol. 27, pp. 246–258, 2019. [Online]. Available: https://www.sciencedirect.com/science/article/pii/S2214860418307358

98. M. Higashi and T. Ozaki, "Selective laser melting of pure molybdenum: Evolution of defect and crystallographic texture with process parameters," *Materials Design*, vol. 191, p. 108588, 2020. [Online]. Available: https://www.sciencedirect.com/science/article/pii/S0264127520301222

99. F. Oehlerking, M. T. Stawovy, S. Ohm, and A. Imandoust, "Microstructural characterization and mechanical properties of additively manufactured

molybdenum and molybdenum alloys," *International Journal of Refractory Metals and Hard Materials*, vol. 109, p. 105971, 2022. [Online]. Available: https://www.sciencedirect.com/science/article/pii/S0263436822001950

100. P. Rebesan, M. Ballan, M. Bonesso, A. Campagnolo, S. Corradetti, R. Dima, C. Gennari, G. Longo, S. Mancin, M. Manzolaro, G. Meneghetti, A. Pepato, E. Visconti, and M. Vedani, "Pure molybdenum manufactured by laser powder bed fusion: Thermal and mechanical characterization at room and high temperature," *Additive Manufacturing*, vol. 47, p. 102277, 2021. [Online]. Available: https://www.sciencedirect.com/science/article/pii/S2214860421004371

101. S. Guo, W. Zhou, Z. Zhou, and N. Nomura, "Laser additive manufacturing of pure molybdenum using freeze-dry pulsated orifice ejection method-produced powders," *Journal of Materials Research and Technology*, vol. 16, pp. 1508–1516, 2022. [Online]. Available: https://www.sciencedirect.com/science/article/pii/S2238785421015271

102. P. M. Dirac and R. H. Fowler, "The quantum theory of the electron," *Proceedings of the Royal Society of London. Series A, Containing Papers of a Mathematical and Physical Character*, vol. 117, no. 778, pp. 610–624, 1928. [Online]. Available: https://royalsocietypublishing.org/doi/abs/10.1098/rspa.1928.0023

103. P. Dirac and R. Fowler, "The quantum theory of the electron: Part II," *Proceedings of the Royal Society of London. Series A, Containing Papers of a Mathematical and Physical Character*, vol. 118, no. 779, pp. 351–361, 1928. [Online]. Available: https://royalsocietypublishing.org/doi/abs/10.1098/rspa.1928.0056

104. H. Weyl, *The Theory of Groups and Quantum Mechanics*, ser. Dover Books on Mathematics. Dover Publications, 1950. [Online]. Available: https://books.google.com/books?id=jQbEcDDqGb8C

105. C. D. Anderson, "The positive electron," *Phys. Rev.*, vol. 43, pp. 491–494, Mar 1933. [Online]. Available: https://link.aps.org/doi/10.1103/PhysRev.43.491

106. A. Franklin and R. Laymon, *The Discovery of the Positron*. Cham: Springer International Publishing, 2021, pp. 31–57. [Online]. Available: https://doi.org/10.1007/978-3-030-62565-8_3

107. D. J. Keeble, U. Brossmann, W. Puff, and R. Würschum, *Positron Annihilation Studies of Materials*. American Cancer Society, 2012, pp. 1–28. [Online]. Available: https://onlinelibrary.wiley.com/doi/abs/10.1002/0471266965.com110.pub2

108. W. Brandt and R. Paulin, "Positron implantation profile effects in solids," *Phys. Rev. B*, vol. 15, no. 25, pp. 2511 – 2518.

109. M. Mourino, H.-P. Löbl, and R. Paulin, "Profiles and absorption coefficients of positrons implanted in solids from radioactive sources," *Physics Letters A*, vol. 71, pp. 106–108, 1979.

110. J. Dryzek and D. Singleton, "Implantation profile and linear absorption coefficients for positrons injected in solids from radioactive sources ^{22}Na and ^{68}Ge/^{68}Ga," *Nuclear Instruments & Methods in Physics Research Section B-beam Interactions With Materials and Atoms*, vol. 252, pp. 197–204, 2006.

111. T. Suzuki, "Measurement of positron diffusion constants in tungsten and molybdenum by the observation of positronium negative ions," in *Journal of Physics Conference Series*, 2016.

112. J. Dryzek, "Remarks on a source contribution in positron lifetime measurements," *Nuclear Instruments and Methods in Physics Research Section B: Beam Interactions with Materials and Atoms*, vol. 521, pp. 1–6, 2022. [Online]. Available: https://www.sciencedirect.com/science/article/pii/S0168583X22000994

113. A. Ore and J. L. Powell, "Three-photon annihilation of an electron-positron pair," *Phys. Rev.*, vol. 75, pp. 1696–1699, Jun 1949. [Online]. Available: https://link.aps.org/doi/10.1103/PhysRev.75.1696

114. F. Selim, "Positron annihilation spectroscopy of defects in nuclear and irradiated materials- a review," *Materials Characterization*, vol. 174, p. 110952, 2021. [Online]. Available: https://www.sciencedirect.com/science/article/pii/S1044580321000826

115. M. J. Puska and R. M. Nieminen, "Theory of positrons in solids and on solid surfaces," *Reviews of Modern Physics; (United States)*. [Online]. Available: https://www.osti.gov/biblio/7071978

116. K. Wada and T. Hyodo, "A simple shape-free model for pore-size estimation with positron annihilation lifetime spectroscopy," *Journal of Physics: Conference Series*, vol. 443, p. 012003, jun 2013. [Online]. Available: https://doi.org/10.1088/1742-6596/443/1/012003

117. K. Wada, F. Saito, N. Shinohara, and T. Hyodo, "Pick-off quenching probability of ortho-positronium per collision with atoms and molecules," *The European Physical Journal D*, vol. 66, no. 4, p. 108, Apr 2012. [Online]. Available: https://doi.org/10.1140/epjd/e2012-20668-5

118. G. F. Knoll, *Radiation Detection and Measurement*. John Wiley and Sons Inc, New York, 2000.

119. J. Gearhart, J. R. Machacek, and L. W. Burggraf, "A three-dimensional array for positron spectroscopy," *To be published*.

120. H. Saito and T. Hyodo, "Direct measurement of the parapositronium lifetime in α-SiO_2," *Phys. Rev. Lett.*, vol. 90, p. 193401, May 2003. [Online]. Available: https://link.aps.org/doi/10.1103/PhysRevLett.90.193401

121. J. M. C. Robles, E. Ogando, and F. Plazaola, "Positron lifetime calculation for the elements of the periodic table," *Journal of Physics: Condensed Matter*, vol. 19, no. 17, p. 176222, apr 2007. [Online]. Available: https://doi.org/10.1088/0953-8984/19/17/176222

122. P. Kirkegaard, J. Olsen, and M. Eldrup, *PALSfit3: A software package for analysing positron lifetime spectra*. Technical University of Denmark, 2017.

123. C. Williams and S. Johnson, "AFIT/ENP and AFRL/RWME Technical Memorandum 09-01: Palsfit (version 1.40) program executive procedure," 2009.

124. K. Siemek, P. Horodek, V. Skuratov, J. Waliszewski, and A. Sohatsky, "Positron annihilation studies of irradiation induced defects in nanostructured titanium," *Vacuum*, vol. 190, p. 110282, 2021. [Online]. Available: https://www.sciencedirect.com/science/article/pii/S0042207X21002360

125. S. C. Mcguire and D. J. Keeble, "Positron lifetimes of polycrystalline metals : A positron source correction study," *Journal of Applied Physics*, vol. 100, p. 103504, 2006.

126. M. Bertolaccini and L. Zappa, "Source-supporting foil effect on the shape of positron time annihilation spectra," *Il Nuovo Cimento B (1965-*

1970), vol. 52, no. 2, pp. 487–494, Dec 1967. [Online]. Available: https://doi.org/10.1007/BF02711092

127. K. Płotkowski, T. J. Panek, and J. Kansy, "Positron implantation profile in kapton," *Il Nuovo Cimento D*, vol. 10, no. 8, pp. 933–940, Aug 1988. [Online]. Available: https://doi.org/10.1007/BF02450195

128. A. Saoucha, "Positron transmission into Kapton: The effective mass absorption coefficient of relevance to positron lifetime experiments," *Journal of Applied Physics*, vol. 85, no. 3, pp. 1802–1810, 1999. [Online]. Available: https://doi.org/10.1063/1.369327

129. T. Staab, B. Somieski, and R. Krause-Rehberg, "The data treatment influence on the spectra decomposition in positron lifetime spectroscopy part 2: The effect of source corrections," *Nuclear Instruments and Methods in Physics Research Section A: Accelerators, Spectrometers, Detectors and Associated Equipment*, vol. 381, no. 1, pp. 141–151, 1996. [Online]. Available: https://www.sciencedirect.com/science/article/pii/0168900296005852

130. M. Haaks, Staab, "Analyzing the high-momentum part of positron annihilation doppler spectra with a single germanium detector," *Nuclear Instruments and Methods in Physical Research A*, vol. 569.

131. O. Mogensen, K. Petersen, R. M. J. Cotterill, and B. Hudson, "Effect of voids on angular correlation of positron annihilation photons in molybdenum," *Nature*, vol. 239, no. 5367, pp. 98–99, Sep 1972. [Online]. Available: https://doi.org/10.1038/239098a0

132. R. M. J. Cotterill, I. K. Mackenzie, L. Smedskjær, G. Trumpy, and J. H. O. L. Träff, "Correlation of void size and positron annihilation characteristics

in neutron-irradiated molybdenum," *Nature*, vol. 239, no. 5367, pp. 99–101, Sep 1972. [Online]. Available: https://doi.org/10.1038/239099a0

133. L. Cheng and P. Sen, "Correlation between swelling and annihilation lineshape parameter in neutron-irradiated molybdenum," *Physics Letters*, vol. 53A, no. 5, pp. 417–418, 1975.

134. L. Cheng, P. Sen, I. MacKenzie, and H. Kissinger, "Positron lifetime study of molybdenum neutron-irradiated at various temperatures," *Solid State Communications*, vol. 20, no. 10, pp. 953–955, 1976. [Online]. Available: https://www.sciencedirect.com/science/article/pii/0038109876904816

135. R. Grynszpan, K. Lynn, C. Snead, A. Goland, and F. Wiffen, "Positron-annihilation investigation of high-temperature neutron-irradiated molybdenum," *Physics Letters A*, vol. 62, no. 6, pp. 459–462, 1977. [Online]. Available: https://www.sciencedirect.com/science/article/pii/0375960177906958

136. K. Petersen, B. Nielsen, and J. H. Evans, "A positron annihilation study of plastically deformed molybdenum," *The Philosophical Magazine: A Journal of Theoretical Experimental and Applied Physics*, vol. 34, no. 5, pp. 685–692, 1976. [Online]. Available: https://doi.org/10.1080/14786437608222042

137. T. Hyodo, B. T. A. McKee, and A. T. Stewart, "Vacancy clusters in neutron irradiated molybdenum," *Radiation Effects*, vol. 68, no. 3, pp. 77–81, 1982. [Online]. Available: https://doi.org/10.1080/01422448208226912

138. B. Pagh, H. E. Hansen, B. Nielsen, G. Trumpy, and K. Petersen, "Temperature dependence of positron annihilation parameters in neutron irradiated molybdenum," *Applied Physics A*, vol. 33, no. 4, pp. 255–263, Apr 1984. [Online]. Available: https://doi.org/10.1007/BF00614668

139. Zhu Zhiyong, Chen Keqin, Chen Jiachao, Xu Ronghui, and Wang Zhiguang, "Positron lifetime study of proton-irradiated molybdenum," *Nuclear Instruments and Methods in Physics Research Section B: Beam Interactions with Materials and Atoms*, vol. 61, no. 1, pp. 72–76, 1991. [Online]. Available: https://www.sciencedirect.com/science/article/pii/0168583X9195563S

140. J. Dryzek and M. Wróbel, "Recovery and recrystallization in molybdenum studied by positron annihilation and x-ray methods," *International Journal of Refractory Metals and Hard Materials*, vol. 97, p. 105514, 2021. [Online]. Available: https://www.sciencedirect.com/science/article/pii/S0263436821000469

141. J. Dryzek and M. Wrobel, "Detection of dynamical recrystallization in a tribolayer of pure molybdenum using positron annihilation and ebsd techniques," *Wear*, vol. 466-467, p. 203524, 2021. [Online]. Available: https://www.sciencedirect.com/science/article/pii/S0043164820309832

142. Clarivate Analytics, "Clarivate Analytics," Technical Report, 2021, Journal Citation Reports.

143. N. E. Ellsworth, R. A. Kemnitz, C. C. Eckley, B. M. Sexton, C. T. Bowers, J. R. Machacek, and L. W. Burggraf, "Influence of nano-sized SiC on the laser powder bed fusion of molybdenum," *Crystals*, vol. 12, no. 9, 2022. [Online]. Available: https://www.mdpi.com/2073-4352/12/9/1276

144. American Society for Testing and Materials, *ASTM E29: Standard Practice for Using Significant Digits in Test Data to Determine Conformance with Specifications*. West Conshohocken, PA, USA, 1967.

145. A. Sidambe, Y. Tian, P. Prangnell, and P. Fox, "Selective laser melting of high-performance pure tungsten: parameter design, densification

behavior and mechanical properties," *Science and Technology of Advanced Materials*, vol. 19(1), pp. 370–380, 2018. [Online]. Available: https://www.sciencedirect.com/science/article/pii/S0263436818303858

146. A. Sidambe, Y. Tian, P.B. Prangnell, and P. Fox, "Effect of processing parameters on the densification, microstructure and crystallographic texture during the laser powder bed fusion of pure tungsten," *International Journal of Refractory Metals and Hard Materials*, vol. 78, pp. 254–263, 2019. [Online]. Available: https://www.sciencedirect.com/science/article/pii/S0263436818303858

147. M. J. Ansari, D.-S. Nguyen, and H. S. Park, "Investigation of SLM process in terms of temperature distribution and melting pool size: Modeling and experimental approaches," *Materials*, vol. 12, no. 8, 2019. [Online]. Available: https://www.mdpi.com/1996-1944/12/8/1272

148. A. Spierings, M. Schneider, and R. Eggenberger, "Comparison of density measurement techniques for additive manufactured metallic parts," *Rapid Prototyping Journal*, vol. 17, pp. 380–386, 08 2011.

149. M. Guo, D. Gu, L. Xi, H. Zhang, J. Zhang, J. Yang, and R. Wang, "Selective laser melting additive manufacturing of pure tungsten: Role of volumetric energy density on densification, microstructure and mechanical properties," *International Journal of Refractory Metals and Hard Materials*, vol. 84, p. 105025, 2019. [Online]. Available: https://www.sciencedirect.com/science/article/pii/S0263436819302094

150. J. Dilip, S. Zhang, C. Teng, K. Zeng, C. Robinson, D. Pal, and B. Stucker, "Influence of processing parameters on the evolution of melt pool, porosity, and

microstructures in Ti-6Al-4V alloy parts fabricated by selective laser melting," *Progress in Additive Manufacturing*, vol. 2, 09 2017.

151. S. Pauly, P. Wang, U. Kühn, and K. Kosiba, "Experimental determination of cooling rates in selectively laser-melted eutectic Al-33Cu," *Additive Manufacturing*, vol. 22, 05 2018.

152. D. Dai, D. Gu, R. Poprawe, and M. Xia, "Influence of additive multilayer feature on thermodynamics, stress and microstructure development during laser 3D printing of aluminum-based material," *Science Bulletin*, vol. 62, no. 11, pp. 779–787, 2017. [Online]. Available: https://www.sciencedirect.com/science/article/pii/S2095927317302475

153. N. Biscay, L. Henry, T. Adschiri, M. Yoshimura, and C. Aymonier, "Behavior of silicon carbide materials under dry to hydrothermal conditions," *Nanomaterials (Basel, Switzerland)*, vol. 11, no. 5, p. 1351, May 2021. [Online]. Available: https://europepmc.org/articles/PMC8161094

154. C. Chatillon and F. Teyssandier, "Thermodynamic assessment of the different steps observed during SiC oxidation," *Journal of the European Ceramic Society*, vol. 42, no. 4, pp. 1175–1196, 2022. [Online]. Available: https://www.sciencedirect.com/science/article/pii/S0955221921008931

155. M. Islam, M. R. Azhar, N. Fredj, T. Burleigh, O. Oloyede, A. Almajid, and S. Shah, "Influence of SiO_2 nanoparticles on hardness and corrosion resistance of electroless Ni–P coatings," *Surface and Coatings Technology*, vol. 261, 12 2014.

156. I. K. MacKenzie, T. L. Khoo, A. B. McDonald, and B. T. McKee, "Temperature Dependence of Positron Mean Lives in Metals," , vol. 19, no. 17, pp. 946–948, Oct. 1967.

157. N. E. Ellsworth, J. R. Machacek, R. A. Kemnitz, C. C. Eckley, B. M. Sexton, J. A. Gearhart, and L. W. Burggraf, "Laser powder bed fusion of molybdenum and Mo-0.1SiC studied by positron annihilation lifetime spectroscopy and electron backscatter diffraction methods," *Materials*, vol. 16, no. 4, 2023. [Online]. Available: https://www.mdpi.com/1996-1944/16/4/1636

158. T. E. M. Staab, R. Krause-Rehberg, B. Vetter, B. Kieback, G. Lange, and P. Klimanek, "The influence of microstructure on the sintering process in crystalline metal powders investigated by positron lifetime spectroscopy: II. tungsten powders with different powder-particle sizes," *Journal of Physics: Condensed Matter*, vol. 11, no. 7, pp. 1787–1806, jan 1999. [Online]. Available: https://doi.org/10.1088/0953-8984/11/7/010

159. *Genie 2000 Spectroscopy Software Operations*, Canberra Industries, Inc., 2006, 387.

160. *DSA-1000 Hardware Manual*, Canberra Industries, Inc., 2005, 109.

161. R. Ziegler and H. E. Schaefer, "Vacancy formation in molybdenum and tungsten investigated by positron lifetime measurements," in *Vacancies and Interstitials in Metals and Alloys*, ser. Materials Science Forum, vol. 15. Trans Tech Publications Ltd, 1 1987, pp. 145–148.

162. P. Hautojärvi, J. Heiniö, M. Manninen, and R. Nieminen, "The effect of microvoid size on positron annihilation characteristics and residual resistivity in metals," *The Philosophical Magazine: A Journal of Theoretical Experimental*

and Applied Physics, vol. 35, no. 4, pp. 973–981, 1977. [Online]. Available: https://doi.org/10.1080/14786437708232638

163. J. Kuriplach and B. Barbiellini, "Improved generalized gradient approximation for positron states in solids," *Phys. Rev. B*, vol. 89, p. 155111, Apr 2014. [Online]. Available: https://link.aps.org/doi/10.1103/PhysRevB.89.155111

164. M. Bernardin, A. Gallone, A. Dupasquier, and P. Pizzi, "Positron annihilation study of ageing and creep on inconel x750," *Physica Status Solidi A, Applied Research*, vol. 56, no. 1, pp. 277–284, 1979.

165. B. T. A. McKee, G. J. C. Carpenter, J. F. Watters, , and R. J. Schultz, "Positron diffusion in metals and trapping at grain boundaries," *Philosophical Magazine A*, vol. 41, no. 1, pp. 65–80, 1980. [Online]. Available: https://doi.org/10.1080/01418618008241831

166. K. Arakawa, K. Ono, M. Isshiki, K. Mimura, M. Uchikoshi, and H. Mori, "Observation of the one-dimensional diffusion of nanometer-sized dislocation loops," *Science*, vol. 318, no. 5852, pp. 956–959, 2007. [Online]. Available: https://www.science.org/doi/abs/10.1126/science.1145386

167. C. Zhang, Z. Li, Y. Ye, Y. Yuan, D. Fang, H. Wu, and W. Li, "Interaction of nanoparticles and dislocations with $Mg_{17}Al_{12}$ precipitates in n-SiC_p/AZ_{91}D magnesium matrix nanocomposites," *Journal of Alloys and Compounds*, vol. 815, p. 152416, 2020. [Online]. Available: https://www.sciencedirect.com/science/article/pii/S092583881933662X

168. Z.-Q. Wang, Y.-H. Li, G.-H. Lu, and H.-B. Zhou, "Influence of carbon and oxygen on the core structure and peierls stress of screw dislocation

in molybdenum," *Metals*, vol. 12, no. 3, 2022. [Online]. Available: https://www.mdpi.com/2075-4701/12/3/507

169. M. A. Abbas, Y. Anru, and Z. Y. Wang, "Comparative study of additively manufactured samples of tungsten with molybdenum and their applications," *IOP Conference Series: Earth and Environmental Science*, vol. 968, no. 1, p. 012008, jan 2022. [Online]. Available: https://dx.doi.org/10.1088/1755-1315/968/1/012008

170. J. Liu and P. Wen, "Metal vaporization and its influence during laser powder bed fusion process," *Materials Design*, vol. 215, p. 110505, 2022. [Online]. Available: https://www.sciencedirect.com/science/article/pii/S0264127522001265

171. M. Simnad and A. Spilners, "Kinetics and mechanism of the oxidation of molybdenum," *JOM*, vol. 7, no. 9, pp. 1011–1016, Sep 1955. [Online]. Available: https://doi.org/10.1007/BF03377603

172. S. Shrestha, T. Starr, and K. Chou, "A Study of Keyhole Porosity in Selective Laser Melting: Single-Track Scanning With Micro-CT Analysis," *Journal of Manufacturing Science and Engineering*, vol. 141, no. 7, 05 2019, 071004. [Online]. Available: https://doi.org/10.1115/1.4043622

173. A. J. Samin, "Oxidation thermodynamics of Nb-Ti alloys studied via first-principles calculations," *Journal of Alloys and Compounds*, vol. 879, p. 160455, 2021. [Online]. Available: https://www.sciencedirect.com/science/article/pii/S0925838821018648

REPORT DOCUMENTATION PAGE

Form Approved
OMB No. 0704–0188

1. REPORT DATE *(DD–MM–YYYY)*	2. REPORT TYPE	3. DATES COVERED *(From — To)*
23-03-2023	Doctoral Dissertation	Sep 2019 – Mar 2023

4. TITLE AND SUBTITLE

Influence of dilute silicon carbide nanoparticle additions to the microstructure and mechanical properties of laser powder bed fusion molybdenum.

5a. CONTRACT NUMBER

5b. GRANT NUMBER

5c. PROGRAM ELEMENT NUMBER

6. AUTHOR(S)

Ellsworth, Nathan, E., Major, USAF

5d. PROJECT NUMBER

5e. TASK NUMBER

5f. WORK UNIT NUMBER

7. PERFORMING ORGANIZATION NAME(S) AND ADDRESS(ES)

Air Force Institute of Technology
Graduate School of Engineering and Management (AFIT/EN)
2950 Hobson Way
WPAFB OH 45433-7765

8. PERFORMING ORGANIZATION REPORT NUMBER

AFIT-ENP-DS-23-M-084

9. SPONSORING / MONITORING AGENCY NAME(S) AND ADDRESS(ES)

Air Force Research Laboratory
Materials and Manufacturing Directorate (AFRL/RX)
Wright-Patterson Air Force Base, OH 45433-7750
Air Force Material Command
United States Air Force

10. SPONSOR/MONITOR'S ACRONYM(S)

AFRL/RX

11. SPONSOR/MONITOR'S REPORT NUMBER(S)

12. DISTRIBUTION / AVAILABILITY STATEMENT

DISTRIBUTION STATEMENT A:
APPROVED FOR PUBLIC RELEASE; DISTRIBUTION UNLIMITED.

13. SUPPLEMENTARY NOTES

This material is declared work of the U.S. Government and is not subject to copyright protection in the United States.

14. ABSTRACT

Consolidation of pure molybdenum through laser powder bed fusion and other additive manufacturing techniques is complicated by a high melting temperature, thermal conductivity, and ductile-to-brittle transition temperatures. Nano-sized silicon carbide particles (0.1 wt%) were homogeneously mixed with molybdenum powder and the printing characteristics, chemical composition, microstructure, and mechanical properties were compared to pure molybdenum for scan speeds of 100, 200, 400, and 800 mm/s. The addition of silicon carbide improved the consolidation and mechanical properties and the oxygen content was reduced. Two mechanisms of oxygen reduction were identified as responsible for the improvements: oxidation of free carbon and the creation of secondary-phase nanoparticles. Positron annihilation lifetime spectroscopy (PALS) and Doppler-broadening of annihilation radiation were used to monitor the microstructural evolution and compared with electron back scatter diffraction analysis. The grain size and misorientation results do not correlate with positron lifetimes indicating the positrons sample sub-grain regions. PALS identified the presence of dislocations and micro-voids not revealed through electron microscopy techniques and correlated with the findings of secondary-phase nanoparticles in the Mo-0.1SiC specimens. This dissertation produced the first proof-of-concept for the possibility of in-situ positron-based, defect monitoring and diagnostic tool.

15. SUBJECT TERMS

additive manufacturing, molybdenum, silicon carbide, nanoparticles, positron annihilation spectroscopy

16. SECURITY CLASSIFICATION OF:			17. LIMITATION OF ABSTRACT	18. NUMBER OF PAGES	19a. NAME OF RESPONSIBLE PERSON
a. REPORT	b. ABSTRACT	c. THIS PAGE			Dr Larry W. Burggraf, AFIT/ENP
U	U	U	U	205	19b. TELEPHONE NUMBER *(include area code)* (937) 255-3636 x4507 larry.burggraf@afit.edu